

Strength and fracture characterization of welded wood joints - Effects of moisture and mixed mode loadings

THÈSE N° 6289 (2014)

PRÉSENTÉE LE 26 SEPTEMBRE 2014

À LA FACULTÉ DES SCIENCES ET TECHNIQUES DE L'INGÉNIEUR
LABORATOIRE DE MÉCANIQUE APPLIQUÉE ET D'ANALYSE DE FIABILITÉ
PROGRAMME DOCTORAL EN SCIENCE ET GÉNIE DES MATÉRIAUX

ÉCOLE POLYTECHNIQUE FÉDÉRALE DE LAUSANNE

POUR L'OBTENTION DU GRADE DE DOCTEUR ÈS SCIENCES

PAR

Martin RHÊME

acceptée sur proposition du jury:

Prof. H. Hofmann, président du jury
Prof. I. Botsis, directeur de thèse
Prof. J. Carmeliet, rapporteur
Dr Y. Leterrier, rapporteur
Prof. S. Morel, rapporteur



ÉCOLE POLYTECHNIQUE
FÉDÉRALE DE LAUSANNE

Suisse
2014

Il n'y a pas de réussite facile
ni d'échecs définitifs.
— Marcel Proust

Acknowledgments

I would like to thank first Prof. John Botsis who accepted me as an external student and gave me access to all what his laboratory could offer in terms of manpower and equipment. Beyond the geographical distance, he kept a close eye on my work and made me benefit from valuable knowledge. Many thanks as well to Joël Cugnoni who always has an answer, whatever the problem. I am still impressed by his scientific and human skills and will always remember his constant cheerfulness, whether during working meetings or around a cup of coffee. My thanks go also to Parviz Navi who shared with me his long experience in the wood field, always with patience and kindness. I particularly enjoyed his positive and encouraging comments about my work.

At this point I would like to thank the members of the jury who have accepted to read and evaluate my work. Their comments enabled improving this final version of my report. I also acknowledge the financial support of the Swiss National Science Foundation.

Many thanks to all the people that I met at the LMAF and at the BUAS for creating a motivating and comfortable working environment. I think in particular about Marco Lai and Piccinini in Lausanne, Christelle, Maria-Inès and Marion in Bienne and would like to thank them for their help and moral support. Thank you as well to the other PhD students of the Sinergia project, Benjamin, Saeed and Maria-Inès for sharing ideas about this tricky topic that is the welding of wood.

Thank you to all my friends, athletes or mountaineer, and to my family. It brings huge relief to know that there are people out there, ready and available for distracting and entertaining meals, beers or sporting activities.

Very special thanks go to my parents, Cathy and Dominique who have been present from the beginning, even when it was not that easy to send me to school on Monday mornings. They are at the roots of the self-confidence, calmness and perseverance that where so much helpful during this work.

And finally, many thanks to Micheline who became my wife during this adventure and also found time to grow our son Gaëtan. I couldn't have spent that much energy working, without her unconditional support and love. She has been a source of happiness and motivation all along these years.

Lausanne, 10th of July 2014

M. R.

Abstract

Wood is a naturally growing material that has been used since the beginning of man's history for various modes of shelter or tool construction. It has proven to be very convenient to machine and to form, however the applications for a single wood piece are limited by the shape and the girth of the tree from where the piece is derived.

Assembling wood pieces together enables working around this issue while efficiently enabling to reduce the effects of the anisotropy and heterogeneity of the material. In addition to the various mechanical assembling techniques, joining with adhesives is broadly used for the production of the engineered wood products in the form of panels or beams for example. However, the use of synthetic adhesives based on oil has a negative influence on the environmental impact of the wood products. That is why more and more bio-based adhesives are under development.

Another solution is to avoid the use of adhesives, which is possible by employing friction welding. This bonding technique is already widely used for metallic and polymeric materials and has been under investigation for the past 15 years in the wood field. The friction between two wood pieces rapidly increases the temperature and softens wood components that are subsequently able to flow at the interface. The joint is solidified during a holding step and is composed of wood fibres entangled in a lignin based matrix material. The advantage of the method is that no material other than wood is needed for the bonding, which yields to a much easier end of life management of the product. From an economical point of view, it is interesting to note that the welding technology does not need drying or curing, both of which being time and space consuming phases of the bond production.

Past research has brought out interesting mechanical properties as well as some issues that currently prevent at the moment the use of the welding of wood for everyday life applications. The joint's mechanical properties seem to strongly depend on the welding process parameters and show a very high scatter that prevent performing accurate predictions regarding the joint failure. Furthermore, poor water resistance has been reported and frequently delamination of the welded piece is observed when immersed in water. Quantitative information about the joint properties under the influence of the moisture content (MC) is still lacking and, at the moment, no numerical model efficiently predicts delamination of welded joints.

In this work, the fracture characteristics of the welded joint are investigated. The goal is to understand and characterize the fracture behavior of the welded joint in a range of moisture content below the fibre saturation point (FSP). The experimental work should help to build a finite element model capable of modeling the fracture behavior of the welded part throughout

its service life.

To this aim, the first part of the thesis is dedicated to the determination of the wood and welded joint properties that are directly related to the MC. Besides the usual equilibrium MC (EMC) and hygro-expansion coefficients of the wood, moisture transport in the welded piece is also studied. A numerical inverse method is used to determine the moisture coefficient of diffusion of the joint. The results show a similar tendency to that of standard adhesives, i.e. the welded joint acts as a barrier against moisture transport.

Afterwards, the pure modes I and II crack propagation are investigated as a function of the MC of the welded piece. Elongated beam specimens with standardized tests (double cantilever beam and end notched flexure) yield to a stable crack propagation and enable measuring the critical energy release rate (ERR). Above a MC of about 16 % the ERR strongly decreases for both modes of fracture. A layer of cohesive elements, of which their parameters are determined in the experimental work, is used in a finite element (FE) model and leads to a satisfactory prediction of the crack propagation in the joint.

During service life, joined pieces are frequently loaded in mixed mode conditions. The influence of the out of plane loading angle on the fracture behavior is investigated with uncracked and pre-cracked specimens. With the help of an Arcan device, the effect of the orientation of the fibres on the strength properties of the joint and its mixed mode behavior can be investigated. It appears that the wood pieces' fibres orientation has no strong influence on the mechanical properties. A mixed mode fracture criterion is expressed by a power law and shows that the introduction of mode mixity decreases the total critical ERR.

A FE model is built with the criterion mentioned above to describe the behavior of a welded beam engraved with a notch in which crack propagation occurs in mixed mode. The numerical results exhibit an earlier onset of propagation than the experiments. The reason is to be sought in the time dependent energy dissipation phenomena that occurs in the wood during the experiment, which are not captured by the linear elastic wood model. Yet, the use of a standardized testing method (mixed mode bending) enabled validating the previous results and the fact that the cohesive elements were suitable to model crack propagation in welded wood joints.

Keywords: Beech, Cohesive elements, Energy release rate, Fracture mechanics, Friction welding, Moisture content, VCCT

Résumé

Le bois est un matériau naturel et répandu dans le monde entier qui a été utilisé dès le début de l'Histoire de l'Homme pour la construction d'abris et d'outils divers. Très pratique à usiner et à former, les applications pour une pièce de bois uniques sont limitées par la forme et la taille relativement petite de l'arbre duquel cette pièce provient.

Assembler des pièces de bois permet de contourner ce problème tout en réduisant les effets de l'anisotropie et de l'hétérogénéité du matériau. Outre les moyens d'assemblage mécanique, les adhésifs sont largement utilisés pour la fabrication de produits en bois reconstitués sous forme de panneaux ou de poutres. Mais l'utilisation d'adhésifs synthétiques à base de pétrole influence négativement l'impact sur l'environnement des produits à base de bois. C'est pourquoi de plus en plus d'adhésifs bio sourcés sont en cours de développement.

Une autre approche est d'éviter l'utilisation d'adhésifs, ce qui est possible par soudage par friction. Cette technique d'assemblage déjà largement utilisée dans des matériaux métalliques et polymères a été étudiée durant ces 15 dernières années pour le domaine du bois. Le frottement entre deux pièces de bois fait augmenter rapidement la température et ramollit les composés du bois qui sont par la suite en mesure de s'écouler à l'interface. Le joint est solidifié au cours d'une étape de maintien et est composé de fibres de bois enchevêtrées dans une matrice à base de lignine. L'avantage du procédé est qu'aucun autre matériau que le bois n'est nécessaire pour le collage, ce qui mène à une gestion beaucoup plus facile de la fin de vie du produit. D'un point de vue économique, il est intéressant de noter que la technologie de soudage n'a pas besoin de séchage ou de durcissement qui sont des étapes du procédé habituel de collage gourmandes en temps et en espace de stockage.

Des recherches antérieures ont mis en évidence des propriétés mécaniques intéressantes, mais aussi certains problèmes qui empêchent à l'heure actuelle l'utilisation de la soudure du bois pour des applications de la vie de tous les jours. Les propriétés mécaniques du joint semblent être fortement dépendant des paramètres du procédé de soudage et montrent une très haute dispersion, ce qui empêche de faire des prédictions exactes concernant la ruine du joint. En outre, une faible résistance à l'eau a été rapportée et, souvent, une rapide delamination de la pièce soudée est observée lorsqu'elle est immergée dans l'eau. Des informations quantitatives sur les propriétés du joint en fonction du taux d'humidité font encore défaut pour le moment, et aucun modèle numérique ne permet de prédire la delamination du joint soudé.

Dans ce travail, les caractéristiques de rupture du joint soudé sont étudiées. L'objectif est de comprendre et de caractériser le comportement à la rupture du joint soudé dans une gamme d'humidité en dessous du point de saturation des fibres. Le travail expérimental doit permettre

de construire un modèle à éléments finis capable de modéliser le comportement à la rupture de pièces soudées en service.

A cet effet, une première partie de la thèse est consacrée à la détermination des propriétés qui sont directement liées au taux d'humidité du bois et du joint. Outre les taux d'humidité d'équilibre et les coefficients de dilatation hygrique du bois, le transport de l'humidité dans la pièce soudée est étudié. Une méthode numérique d'identification inverse est utilisée pour déterminer le coefficient de diffusion de l'humidité du joint. Les résultats montrent une tendance similaire à celle des adhésifs classiques, c'est à dire que le joint soudé agit comme une barrière contre le transport d'humidité .

Par la suite, les modes purs I et II de propagation des fissures sont étudiées en fonction du taux d'humidité de la pièce soudée. Des échantillons de forme allongée avec des tests standardisés (double cantilever beam et end notched flexure) donne une propagation de fissure stable et permettent de mesurer le taux de restitution de l'énergie élastique. Au dessus d'un taux d'humidité d'environ 18 %, le taux de restitution d'énergie diminue fortement et ce pour les deux modes de rupture. Une couche d'éléments cohésifs avec les paramètres déterminés par le travail expérimental est utilisée dans un modèle FE et mène à une prédiction satisfaisante de la propagation de fissures dans le joint.

Pendant la durée de vie, les assemblages sont souvent chargés en mode mixte. L'influence de l'angle de chargement hors du plan sur le comportement à la rupture est étudiée avec des échantillons non fissurés et pré- fissurés. Avec l'aide d'un dispositif Arcan, l'effet de l'orientation des fibres sur les propriétés de résistance du joint et son comportement de rupture en mode mixte peuvent être étudiés. Il semble que l'orientation des fibres des pièces de bois n'a pas de forte influence sur les propriétés mécaniques. Un critère de rupture en mode mixte est exprimé par une loi de puissance et montre que l'introduction d'une mixité de mode diminue le taux critique de restitution de l'énergie totale.

Un modèle FE est construit avec le critère mentionné ci-dessus pour décrire le comportement d'une poutre soudée avec une encoche dans laquelle se produit une propagation de fissures en mode mixte. Les résultats numériques montrent une initiation de propagation se produisant avant celle des expériences. La raison est à chercher dans les phénomènes de dissipation d'énergie dépendant du temps et survenant dans le bois lors de l'expérience, et qui ne sont pas capturés par le modèle élastique linéaire du bois. Cependant, l'utilisation d'une méthode d'essai normalisée (mixed mode bending) a permis de valider les résultats précédents et le fait que les éléments cohésifs sont adaptés pour modéliser la propagation de fissures dans les joints soudés de bois.

Keywords : Elements cohesifs, Hêtre (*fagus sylvatica*), Mécanique de la rupture, Soudage par friction, Taux de restitution de l'énergie élastique, Taux d'humidité, VCCT

Contents

Acknowledgments	v
Abstract (English/Français)	vii
Table of Content	xi
List of Figures	xv
List of Tables	xxi
List of Symbols and Abbreviations	xxiii
1 Introduction	1
1.1 Context and motivations	1
1.2 Objectives and organization of the work	2
2 State of the Art	7
2.1 Wood behavior	7
2.1.1 Hierarchical structure of wood	7
2.1.2 Moisture related behavior	9
2.1.3 Mechanical behavior	11
2.2 Fracture mechanics	13
2.2.1 Basics of linear elastic fracture mechanics	13
2.2.2 Mode I fracture in the wood field	16
2.2.3 Mode II fracture in the wood field	17
2.2.4 Mixed mode I/II fracture in the wood field	17
2.3 Friction welding of wood	18
2.3.1 Welding technology	18
2.3.2 Microstructure of the welded joint	18
2.3.3 Mechanical properties of the welded joint	19
2.3.4 Numerical modeling of the welded joint	20
2.4 Summary	20
	xi

3	Materials and methods	23
3.1	Wood preparation and friction welding process	23
3.2	Moisture related properties	24
3.2.1	Equilibrium state	24
3.2.2	Moisture transport	25
3.3	Mode I testing	26
3.3.1	Specimen preparation	26
3.3.2	DCB test	27
3.4	Mode II testing	28
3.4.1	Specimen Preparation	28
3.4.2	4-ENF test	28
3.5	Maximal strength testing	29
3.5.1	Tensile specimen	29
3.5.2	Tensile test	30
3.5.3	Torsion specimen	30
3.5.4	Torsion test	30
3.6	Arcan test	31
3.6.1	Specimen preparation	31
3.6.2	Experimental methods	34
3.7	Mixed mode crack propagation	34
3.7.1	Specimen preparation	34
3.7.2	Experimental methods	35
3.8	Fracture of joint modeling	36
3.8.1	Cohesive elements models	37
3.8.2	VCCT	39
3.9	Summary	40
4	Moisture related properties	41
4.1	Equilibrium state	41
4.2	Moisture transport	43
4.3	Summary	48
5	Mode I crack propagation	49
5.1	Experimental tests	49
5.1.1	DCB test and energy release rate	49
5.1.2	tensile test and maximal strength	54
5.2	Finite elements modeling	56
5.3	Summary	57
6	Mode II crack propagation	59
6.1	Experimental tests	59
6.1.1	4-ENF test and energy release rate	59
6.1.2	Torsion test and maximal strength	62

6.2	Finite elements modeling	63
6.3	Summary	65
7	Crack initiation and mode mixity	67
7.1	Strength analysis	67
7.1.1	Specimen design	67
7.1.2	Maximal Strength	70
7.2	Critical energy release rate	72
7.3	Summary	79
8	Mixed mode crack propagation	81
8.1	SENB specimen	81
8.2	4-SENB test	82
8.3	MMB test	86
8.4	Finite elements modeling	87
8.5	Summary	91
9	Conclusions and future work	93
9.1	Conclusion	93
9.1.1	Effect of moisture	93
9.1.2	Mixed mode fracture and mechanical behavior modeling	94
9.2	Future work	95
9.2.1	Micro mechanics	95
9.2.2	Modeling of crack propagation with MC variation	96
9.2.3	Structure assessment	96
	Bibliography	99
	Curriculum Vitae	111

List of Figures

1.1	Processes and interactions coming into play for the modeling of a welded piece in real conditions.	3
1.2	Contribution and detailed working plan of the thesis.	4
2.1	Structure and micro-structure of wood at various scale levels [1].	8
2.2	Illustration of the local orientation system with the associated section of the wood [2]	8
2.3	Illustration of the three basic modes of crack loading.	15
2.4	Illustration of the different friction welding technologies.	18
2.5	(a) SEM picture of joining material composed of wood fibers embedded in a molten lignin matrix [3]. (b) Confocal microscopy of a welded joint with densified zones on both sides of the joint [4]	19
3.1	(a) Photograph and (b) syochematic representation of the welding machine (www.bransoneurope.eu).	24
3.2	(a) Sketch of the 3-layer welded piece. (b) Picture of sample ready to be sealed and stored in new climatic conditions (85% RH). (c) Sketch of the cuts after the diffusion test.	26
3.3	Sketch of the DCB specimen.	26
3.4	Experimental configuration of the DCB test	27
3.5	Sketch of the geometry of the ENF specimen and the test configuration.	28
3.6	(a) Metallic wedge glued on the specimen's lower beam and (b) detail of the lower support with a machined notch in the roller. (c) General view of the configuration of the 4-ENF setup for mode II testing.	29
3.7	(a) Schematic representation of the tensile specimen. (b) Photograph of the tensile test setup.	30
3.8	(a) Schematic representation of the torsion specimen. (b) Photograph of the torsion test setup	31
3.9	Schematic representation of the preparation process and testing of the Arcan specimens. See text for details.	32
3.10	Sketch of the Arcan specimens with the dimensions for the strength tests in tension (a), shear (b) and mixed loading (c). (d) represents the specimen for fracture testing.	33

List of Figures

3.11	Examples of specimens for the Arcan test in (a) tension, (b) shear and (c) mixed loading	33
3.12	Photograph of the Arcan setup mounted for (a) tensile testing, (b) shear testing and (c) mixed mode testing at an angle of 45°.	34
3.13	(a) Specimen after welding and cutting of the notch in the thin layer (5mm). (b) Sketch of the specimen and the testing situation. (c) Photograph of the setup for 4-SENB	36
3.14	Sketch (a) and photograph (b) of the MMB setup	36
3.15	Schematic representation of the cohesive law in normal and shear mode as well as in mixed mode.	38
3.16	VCCT for ERR calculation on a 2D model.	39
4.1	left: Evolution of the dimensions with changing MC. right: Corresponding hygro-expansion coefficients in the range of MC from 0 % to the FSP.	42
4.2	Sorption isotherm for beech wood. In black are the curves calculated based on data by Vorreiter [5]. The red curve is the adsorption calculated with experimental values. The parameters of relation 2.2 are expressed in table 4.2.	43
4.3	Experimental MCs measured as a function of the position in the specimen and the diffusion time.	44
4.4	Comparison of the experimental values with numerical results. In this case, the same diffusion coefficient for wood and for the joint is used.	45
4.5	Flowchart of the identification process.	46
4.6	Moisture content profile within the pieces. The curves are the result of the identification of the coefficient of the joint and the dots are the experimental data. In (a) the coefficient of diffusion of the joint is identified while the other parameters are left constant. In (b) the diffusion coefficient of wood and film coefficient are identified with a constant coefficient of the joint.	46
4.7	Evolution of the moisture diffusion coefficients with the MC below FSP.	47
5.1	Comparison of typical load-displacement experimental curves (straight lines) with results obtained by FEM (dashed line). The relative error, represented by the gray area, is calculated according to the standard deviation of the experimental data (see text for details).	50
5.2	At the top is a schematic representation of the crack path on a moist specimen (22% MC) after separation of the joint. The pulled out fibers are the brown lines coming out of the joining material in black. The photograph at the bottom is a magnification showing the detail. The SEM picture shows the transition of the crack path that crosses the joint material from one interface to the other.	51
5.3	Optical light microscopy photograph of the fracture planes for all four different MCs. The fracture surface exhibits islands and valleys formed by the welded material. The opposite surface has the negative print of these features. At this scale, only the moist specimens exhibit a fleecy surface. This is due to long fibers coming out of the joining material.	52

5.4	Evolution of the critical energy release rate (G_{Ic}) and the maximal tensile strength of the welded joint in terms of the corresponding MC.	53
5.5	Representative stress-strain curves obtained during the tensile test at different MCs.	54
5.6	(a) Location of the lines along which the displacements are measured to compute the strain. Straight lines serve as an optical extensometer for the wood part, dotted lines for the joint and dashed lines are the strain over the total width of the picture. (b) Strain-stress curves corresponding to the different extensometer presented in (a).	55
5.7	Close images of the fractured joint (black part in the middle) after failure of the tensile specimen. Fibres entanglement between the two broken parts differentiate the dry (left) and moist (right) specimens.	56
5.8	Schematic of the DCB FE model (see text for detail).	56
6.1	Examples of load displacement curves obtained with the 4-ENF test at various MCs	60
6.2	(a) Photograph at the beginning of the test (top) and after 25 mm of crack propagation (bottom). The distance between each vertical line is 1 mm. (b) Sketch of the lateral surface of the ENF specimen after separation, which is based on optical microscopy observations. The dark parts represent the joining material and the wood beam appears striped. Fibers are indicated by the thin lines. . . .	61
6.3	Evolution of the critical energy release rate (G_{IIc}) and the maximal shear strength of the welded joint as a function of the MC of each group of specimens.	62
6.4	(a) Torque related to the angle of rotation during the torsion test. One representative curve for each MC is presented. (b) Torsion specimens after fracture. Three types of fracture occurred. (1) Fully in the welded joint, (2) partially in the joint and mainly in wood, and (3) partially in wood and mainly in the joint. . .	63
6.5	Schematic of the FE model (see text for detail)	63
6.6	Effect of friction on the load-displacement response according to the FE modeling. Friction between the support and the specimen has much more influence than friction between the beams of the specimen. “Beam Friction” indicates the friction between the two wood beams. “Support Friction” refers to friction between the supports and the specimen. In both cases, the coefficient of friction is assumed to be $\mu = 0.4$	65
7.1	(a) View of the Arcan setup and specimen as modeled in Abaqus. (b) Organization of the cylindrical coordinate systems around the part. In this case, the R, T and Z axes represent respectively the radial, tangential and longitudinal directions. . .	68
7.2	(a) Distribution of tensile stress along the interface during tensile test. (b) Distribution of shear stress during shear test. Both graphics show the influence of cut grooves on the sides of the specimens.	69

List of Figures

7.3	(a) Example of specimen that encountered a combined failure in the wood and in the joint. (b) t-r shear stresses distribution in the wood. (c) Tensile stresses in the tangential direction in the wood. The high stress regions are indicated with black arrows.	69
7.4	Effect of the groove's angle on the (a) tensile and (b) shear stress distributions with a mixed loading.	70
7.5	Maximal tensile (a), mixed (b) and shear (c) strength measured with the Arcan test.	71
7.6	(a) Effect of the element's height on the values of G along the crack front. The element length is constant and equal to 2.5 mm. (b) Effect of the element's length along the interface on the values of SERR along the crack front. The height of the elements is constant and equal to 2.5 mm.	73
7.7	Examples of ERR profile along the crack front for each loading angles tested in the experimental part. The loads used in the model are the average of the experimental maximal loads of each group.	74
7.8	Evolution of the mixed mode ratio with the loading angle for both types of specimen orientation.	75
7.9	Flowchart presenting the process to determine the critical ERR by combining an experimental and numerical approach.	75
7.10	ERR values determined with combined Arcan experiment and VCCT, (a) for the 0-0 specimens and (b) for the 0-90. The empty symbols are the individual ERR value for each specimen. The filled symbols show the average value of each group of specimen tested with the same loading angle.	76
7.11	Side view of the (a) 0-0 and (b) 0-90 specimens taken with confocal autofluorescence microscopy and optical photography (box). The wood fibers are either blue or yellowish and the joining material is the brown part in the center of the images.	77
7.12	Fracture envelop for 0-0 welding orientation compared with the results of ENF, MMB and DCB test.	78
7.13	Comparison of tensile and shear stresses experienced by the bonded region of the joint for the strength (uncracked) and fracture (pre-cracked) specimens. . .	79
8.1	(a) FEM showing the values of G_T on the joined surfaces. Here the half specimen with a crack of 5 mm. (b) Evolution of G_T and the mixed mode ratio with increasing crack length.	82
8.2	Load displacement data of the 4-SENB test for (a) 0-90 and (b) 0-0 specimens. .	83
8.3	Experimental load and displacement data during loading and unloading cycles of (a) 4-SENB (0-90 specimen) and (b) MMB.	83
8.4	Measured dissipated energy (U^{dis}) for each cycle as a function of the observed crack length (top) and ratio of the energy dissipated to the cracked surface per cycle for the 4-SENB (squares) and MMB (triangles) experiments.	85

8.5	(a) Load-displacement data during cyclic loading with a holding step of 1 hour at constant displacement. (b) Evolution of the load during the holding step at 0.5 mm of displacement.	86
8.6	(a) Load and displacement data of the MMB test for 5 different specimens and the FE model curve. Experimental data are in black and FE results in red. (b) Corresponding curves of the evolution of G_T with the crack length.	86
8.7	Sketch of the 4-SENB propagation model	87
8.8	(a) Numerical load and displacement curve (plain) compared with the associated crack length (dashed). (b) Similar to (a) but for one of the experimental test. . .	88
8.9	Numerical load and displacement curves (red) compared with the experimental results.	90
8.10	Presentation of the FE model for MMB test with a magnification of the crack tip region.	91
9.1	Side view of a welded joint taken with autofluorescence confocal microscopy. .	95
9.2	(a) Schematic representation of the position of the gratings on the DCB specimen. (b) Comparison of the experimental (blue) and numerical (purple) values of strain as function of time for three of the ten gratings. The associated observed crack tip position is indicated with the dashed line.	97

List of Tables

2.1	Identified diffusion coefficient for beech.	11
2.2	Elastic constants given in the literature for beech and as comparison with a softwood type (spruce)	12
3.1	Welding process parameters for specimens production	24
3.2	Salts used to set the RH in climatic boxes	25
4.1	Moisture dependent properties of the wood.	41
4.2	Parameters of the sorption isotherm curve.	42
4.3	Identified diffusion parameters (see equation 2.6)	48
5.1	Roughness and fractal data of the fractured surface.	53
5.2	Experimental data of the tensile and DCB test.	57
6.1	Experimental results of the torsion and 4-ENF test	64
7.1	Maximal strength value determined with the Arcan test.	72
7.2	Parameters of the mixed mode power expression (equation 7.1)	76
8.1	Data of the cyclic 4-SENB test.	84
8.2	Data of the cyclic MMB test.	84

List of Symbols and Abbreviations

α	Coefficient of hygro-expansion tensor
δ	Displacement
$\dot{\epsilon}$	Deformation rate tensor
ϵ	Deformation
γ	Surface energy
μ	Friction coefficient
ν	Poisson's ratio
ρ	Density
σ	Stress
τ_{max}	Maximal shear strength
C	Compliance matrix
a	Crack length
a_0	Initial crack length
b	Specimen width
C	Compliance
c	Water concentration
c_p	Specific heat
D	Mass diffusion coefficient
D_0	Diffusion coefficient at 0% of moisture content
E_K	Stiffness of cohesive element
E_l	Longitudinal Young's modulus

List of Symbols and Abbreviations

E_r	Radial Young's modulus
E_t	Tangential Young's modulus
G_{Ic}	Mode I critical strain energy release rate
G_{IIc}	Mode II critical strain energy release rate
G_{IIIc}	Mode III critical strain energy release rate
G_{III}	Mode III strain energy release rate
G_{II}	Mode II strain energy release rate
G_I	Mode I strain energy release rate
G_{rl}	Radial-longitudinal shear modulus
G_{tl}	Tangential-longitudinal shear modulus
G_{tr}	Tangential-radial shear modulus
G_T	Total energy release rate
J	Flow
k	Thermal diffusion coefficient
K_i	Mode i stress intensity factor
l	Longitudinal direction
P	Load
r	Radial direction
t	Tangential direction
t_n	Nominal stress in the direction normal to the interface
t_s	Nominal stress in the first shear direction
t_t	Nominal stress in the second shear direction
u	Moisture content
3-ENF	Three points bending test with an end notched flexure specimen
3-SENB	Three points bending test with a single edge notched beam specimen
4-ENF	Four points bending test with an end notched flexure specimen
4-SENB	Four points bending test with a single edge notched beam specimen

CT	Computed tomography
CTS	Compact tension shear
DCB	Double cantilever beam
EMC	Equilibrium moisture content
ENF	End notched flexure
ERR	Energy release rate
FBG	Fiber Bragg Grating
FE	Finite elements
FEM	Finite elements method
FPZ	Fracture process zone
FSP	Fibre saturation point
LEFM	Linear elastic fracture mechanics
MC	Moisture content
MMB	Mixed mode bending
MPC	Multi-point constraint
RH	Relative humidity
SEM	Scanning electron microscopy
SENB	Single edge notched beam
SERR	Strain energy release rate
SIF	Stress intensity factor
SLB	Single leg bending
VCCT	Virtual crack closure technique

1 Introduction

1.1 Context and motivations

Due to its widespread availability and ease of machining, wood has been used from the beginning of mankind to produce tools and shelters. Even nowadays, its low ecological impact and high specific mechanical properties make it an interesting alternative to polymeric or metallic materials. Consequently, it is abundantly used for interior furniture, buildings skins and structural applications.

On account of the limited size and the heterogeneous nature of trees, the correct assembly of wood is an important issue in wood science. Joining techniques in the field of engineered wood products are used to either increase the size and tailor the shape of the pieces (e.g. glulam and cross-laminated timber) or to increase dimensional stability and isotropy (e.g. plywood and cross-laminated panel). For the pre-mentioned wood-based products, gluing is often the chosen assembling technique among the other available mechanical means in the wood field. However, adhesives need to be carefully applied and cured, which is time and space demanding. Furthermore, they are often by-products of the oil industry and have a negative impact on the end of life of the wood-based products.

Friction welding of wood is a joining technique in development and has the advantage of being a fast process that does not require the utilization of additional material (mechanical fastener or synthetic adhesives). The joint is generated at the interface by the mixture of molten wood components and wood fibers during the thermo-mechanical effects produced by the friction and solidified in a holding step. Welding wood provides an interesting alternative to gluing, because the elimination of the adhesive can reduce costs and environmental effects generated by the whole life cycle of the product.

In order to be used in practical applications and compete with standard adhesives, the bonding created by welding must offer enough strength and reliability. Indeed, the hygroscopic interaction of the wood with its environment leads to serious issues that can result in material failure. For example, the process of wood drying is known to be problematic with regards

to wood cracking and is intensively studied. A great deal of research in this field has been aimed at modeling the correct behavior of wood in changing climatic conditions and the early macroscopic approach [6, 7, 8], which has already shown good results, tends to be enhanced by a multi-scale approach [9].

Research conducted in the field of welding of wood the last 15 years has highlighted similar moisture related problems that prevent its use in products manufacturing. Indeed, the already low mechanical strength of the joint seems to be further reduced by contact with moisture or water. Studies have reported spontaneous delamination or a strong decrease of shear strength of welded pieces immersed in water [10, 11, 12], but besides this, quantitative studies of the effect of moisture on the mechanical properties, and more precisely the fracture characteristics of the welded joint, are lacking. Furthermore, the heterogeneous microstructure of the joint leads to a high scatter of the mechanical strength, making accurate failure prediction difficult. It is therefore of practical interest to have a model available to predict delamination of welded pieces for design purposes. However, at the moment no complete characterization of the fracture behavior of the welded joint has been performed.

1.2 Objectives and organization of the work

The goal of this work is to study and characterize the strength and the fracture properties of welded wood joints. To achieve this, the welded joint is investigated with a focus on the fracture mechanics, typically applied to resolve delamination problem, i.e. when a crack propagates between two layers of materials. The studies presented in this work aim at understanding the effects of moisture and mixed mode loadings of welded pieces with experimental procedures and numerical analyses. The following objectives are defined:

- Characterize the strength and fracture properties of a welded wood joint.
- Determine the cohesive parameters of the joint.
- Build a numerical model of the bond delamination.

This work should contribute towards increasing the knowledge of the fracture behavior of welded joints at various moisture content (MC). The experimental result will serve to define parameters of numerical models to predict the behavior of welded joints subjected to external loads and climatic variation and also provide a tool to facilitate the appropriate design of a welded assembly. To reach the objectives of this work, the following activities are proposed:

- Preparation of the specimens by linear friction welding of beech wood and appropriate subsequent machining.
- Characterization of the properties of the wood used and the diffusion properties of the welded joint.

- Testing of specimens at various EMC with standardized fracture tests in pure mode I and II.
- Testing of specimens at various angles of loading in order to determine the mixed mode behavior of welded joints at a given MC.
- Construction of numerical models to support and/or describe the experimental tests with a greater focus on cohesive laws in pure and mixed mode fracture.
- Validation of the numerical models by comparison with experimental data.

Figure 1.1 schematically summarizes the information needed to model welded pieces in service conditions (for simplification, only an isothermal situation is presented here). Obviously, all the materials and interactions present need to be characterized. The mechanical and hygro behavior of wood is already well documented in the literature and models exist. Sometimes, only the properties specific to the wood species in question are lacking. In regard to the welded joint, however, not much work was done to quantify the effect of moisture on the mechanical properties. The present study focuses on the determination and characterization of the joint fracture properties, as detailed in figure 1.2.

Chapter 2 provides an overview of the state of the art of the different fields addressed in this work. The structure and the properties of wood are briefly introduced. The basic concepts to understand fracture mechanics are reviewed, followed by more specific focus on the fracture of wood. Finally a review of past research in the field of the welding of wood is given. In **Chapter 3** the experimental and numerical methods that are used throughout this work are introduced.

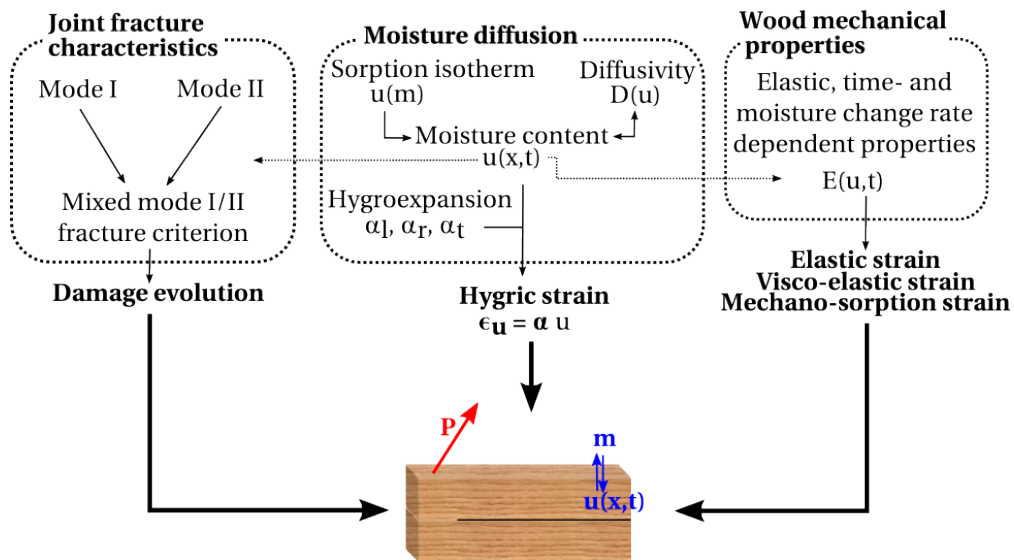


Figure 1.1: Processes and interactions coming into play for the modeling of a welded piece in real conditions.

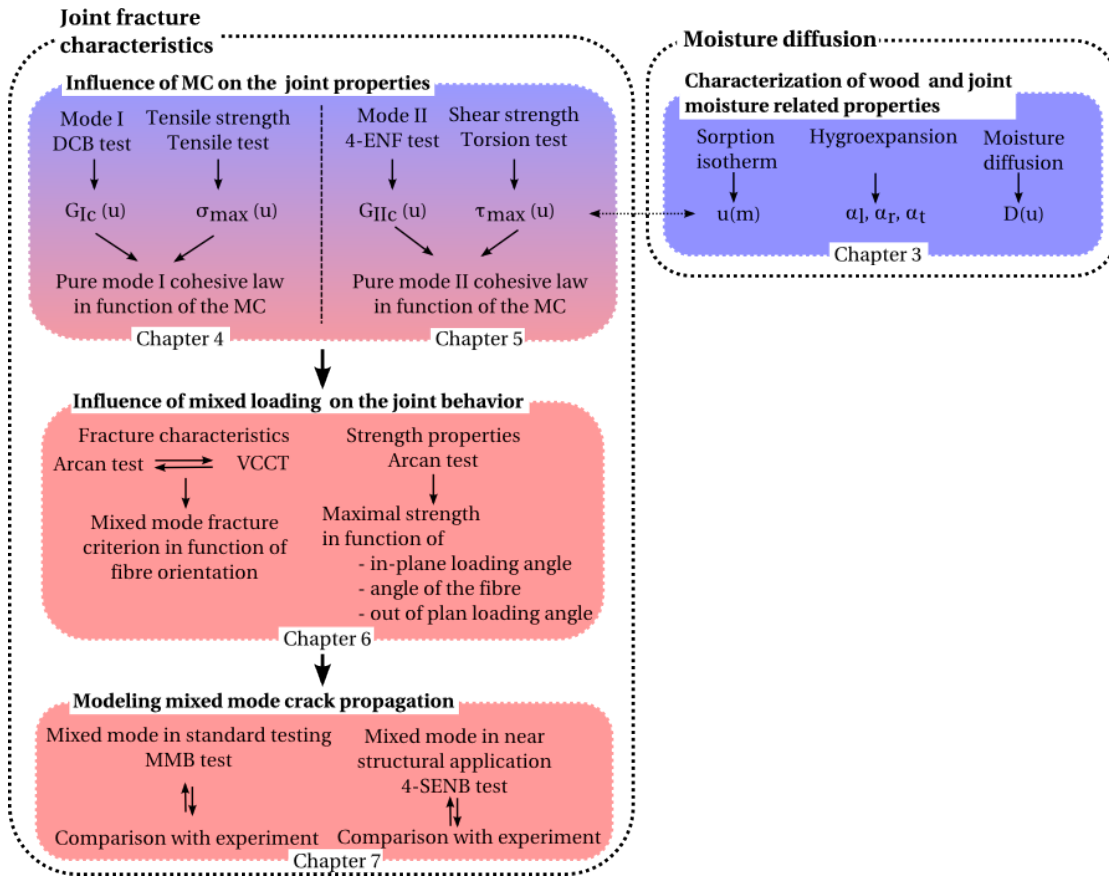


Figure 1.2: Contribution and detailed working plan of the thesis.

The welding process is presented and a detailed description of the specimens' preparation and the course of the tests is given. The numerical methods to model crack propagation are also presented. **Chapter 4** presents a characterization of the water related physical and mechanical properties. Hygro-expansion and sorption isotherms of the wood are experimentally measured and moisture diffusion coefficients are determined by inverse methods based on FE modeling. In **Chapter 5**, the effects of various MC on the mode I strain energy release rate (ERR) are characterized. For this purpose, double cantilever beam (DCB) specimens are acclimatized in various climatic conditions and subsequently tested at a controlled displacement rate. The same levels of MC are used for the determination of the maximal tensile strength of the joining material and the experimental results are used to establish cohesive parameters to model crack propagation. The same topic is addressed for mode II in **Chapter 6**, where the effects of MC are determined using the same procedure as previously described, but with end notched flexure (ENF) specimens tested in 4-point bending. Torsion tests are carried out to determine the maximal shear strength and again, cohesive parameters are successfully implemented in a numerical model. Since in real conditions mixed mode loadings are likely to occur, mixed mode fracture is investigated in **Chapter 7**. In a first step, Arcan testing using

uncracked specimens enables studying the effect of the fibers orientation of the wood parts on the strength properties. Afterwards, a combined experimental and numerical work with pre-cracked specimens enables determining mixed mode fracture criteria of the welded joint. More particularly, the experimental load at failure is used in a numerical model and the ERR in the different modes are computed with a virtual crack closure technique (VCCT). In **Chapter 8**, the fracture criteria determined in chapter 7 are used to predict the mechanical behavior of a welded beam containing a notch and loaded with external loads. A single edge notched beam (SENB) specimen is loaded in bending and mixed mode propagation occurs in the joint. Mixed mode bending (MMB) tests are also performed as a standardized method for mixed mode fracture to be compared with the bending test of the SENB specimen. Finally, a summary of the thesis is given in **Chapter 9**. The concluding remarks are followed by suggestions for future works in this field.

2 State of the Art

This chapter briefly overviews past research carried out in the fields addressed in this work. A general introduction to wood properties are presented. Then, the concepts of fracture mechanics are introduced and the last part presents the state of the research in the field of wood fracture. Mode I, II and mixed mode I/II testing methods are presented and some results are commented on. Finally, the welding of wood technology and its structure and properties are presented.

2.1 Wood behavior

2.1.1 Hierarchical structure of wood

Wood is an organic material composed of natural fibers embedded in a matrix of lignin that give it a cellular and porous structure dictated by the need of the living tree for nutriment transport and structural support. Tree growth occurs in a radial manner at the interface between the wood and the bark and can be simplified as the superposition of yearly slightly conical layers of new cells. Depending on the observation scale, the structure of wood is different, but at a macro scale one can consider that the wood is a homogeneous cylindrical orthotropic material (see figure 2.1) and therefore the rules of continuum mechanics apply.

The directions of orthotropy correspond to the three local directions of the wood. The longitudinal (l) direction is collinear to the pith of the tree, the radial direction (r) goes along the radius of the year rings and the tangential direction (t) is tangential to the year rings. The local coordinate system of the wood is illustrated in figure 2.2.

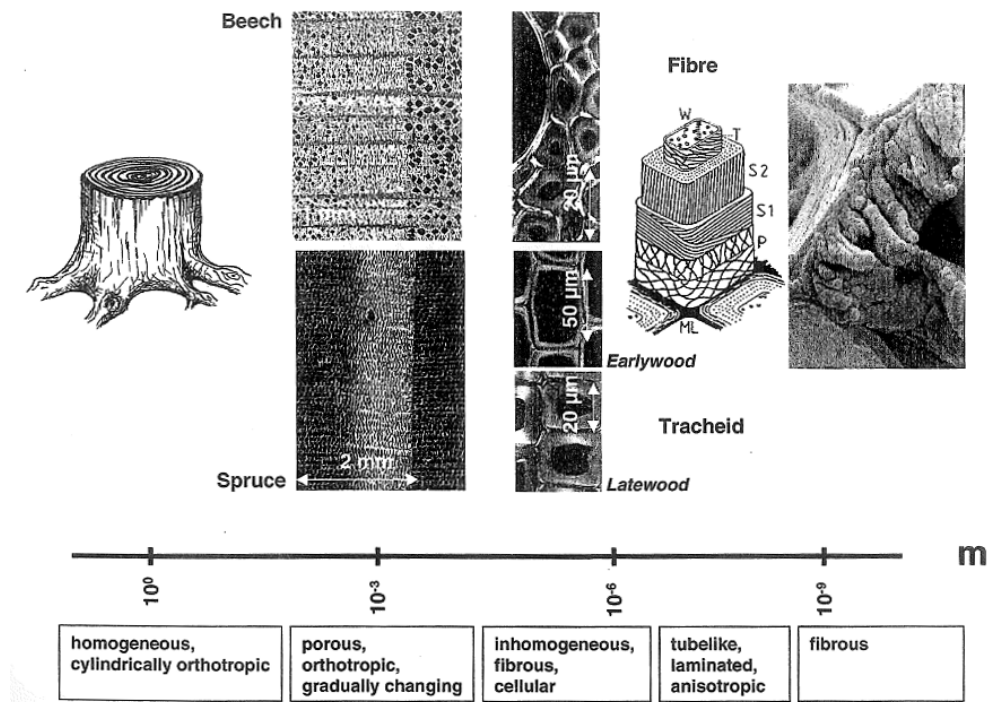


Figure 2.1: Structure and micro-structure of wood at various scale levels [1].

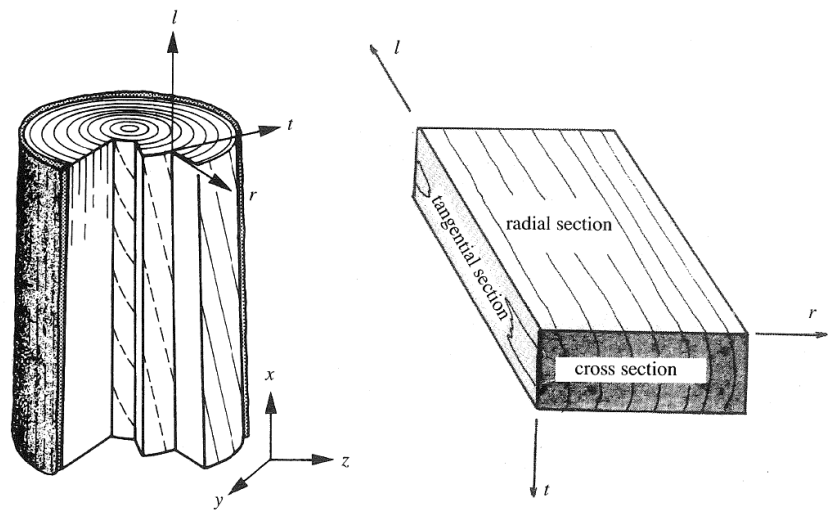


Figure 2.2: Illustration of the local orientation system with the associated section of the wood [2]

2.1.2 Moisture related behavior

Sorption of moisture

Wood is a hygroscopic material, which means that it strongly interacts with water because it has the capability to adsorb or desorb moisture. In wood, water can be found in two forms: bound water in the cell walls and free water in liquid, solid or gaseous form in the lumen of the wood cells. The fiber saturation point (FSP) is the point where cell walls are saturated with bound water and additional water will localize itself in the lumen. The MC of wood is evaluated according to equation 2.1, with the ratio of the mass of water to the mass of dry wood.

$$u[\%] = \frac{m_g - m_o}{m_o} 100 \quad (2.1)$$

With m_g being the mass of moist wood and m_o the mass of dry wood. The procedure of this measurement is described in the standard [13]. Once a tree is cut down, its water content decreases to reach an equilibrium with the relative humidity (RH) of the ambient atmosphere. This value is called the equilibrium moisture content (EMC). The relation between the relative humidity of the air and the EMC is expressed by a sigmoid called a sorption isotherm.

Numerous theories for water sorption mechanisms to describe the sorption isotherms are available. Several of them make the assumption that water molecules attach on sorption sites in the wood in a multilayered manner. Thus, many equations based on different physical and mathematical models have been proposed. Some of these theories are presented in Skaar [14]. Brunauer et al. [15] and Dent [16] both proposed a model for multilayer adsorption of gas that can be expressed by the equation below.

$$\frac{h}{u} = A + Bu - Cu^2 \quad (2.2)$$

where h is the RH of the air. Simpson [17] performed an analysis of existing models and tested their accuracy to fit experimental data of EMC. He mentioned that, even though it has no physical meaning, a fifth order polynomial expression can express sorption isotherms as well as all the presented physical models.

Diffusion of moisture

Below the FSP, water movement in wood can happen in two ways; via bound water diffusion in the wood cell walls and water vapor diffusion in the lumens of the cells. However, as a first approximation, it is possible to combine all the diffusion processes under one diffusion

coefficient and insert it in models of steady state diffusion based on Fick's first law.

$$J = -D\nabla c \quad (2.3)$$

where J is the flow and D the diffusion coefficient. In general case and as express in 2.3, the concentration is considered to be the driving force for diffusion. However, in wood, several authors have shown that other potential may be used, e.g. moisture content, chemical potential, spreading pressure, activated water molecule, etc... [18, 19, 20, 21].

For unsteady state diffusion and a diffusion coefficient dependent on the concentration and temperature, one can use the Fick's second law.

$$\frac{\partial c}{\partial t} = \nabla (D(c, T)\nabla c) \quad (2.4)$$

which, for simplified cases with a constant diffusion coefficient and one dimensional diffusion turns into:

$$\frac{\partial c}{\partial t} = -D \frac{\partial^2 c}{\partial x^2} \quad (2.5)$$

Diffusion coefficient

The determination of diffusion coefficients is very important, particularly in the wood drying field. Analytical solutions based on mathematical models don't sufficiently describe the reality, principally because MC independent diffusion coefficients cannot be used for wood [22]. Therefore, numerical models were used to find the best coefficients corresponding to experimental data.

Inverse numerical methods to identify water transport in wood were carried out successfully [23, 24, 25]. For beech wood, Agoua et al. [26] determined constant diffusion and transfer coefficients with a worst case error reach of 10%. Olek et al. [25] used a method to identify the transient bound water diffusion coefficient where the experimental data were obtained during an unsteady-state experiment and the model was based on Fick's second law expressed with a diffusion coefficient dependent on the driving force (equations 2.6 and 2.7).

$$D = D_0 e^{dM} \quad (2.6)$$

With M in the case of Olek et al. [25] representing the reduced water content.

$$M = \frac{u - u_i}{u_e - u_i} \quad (2.7)$$

u_i and u_e denote the initial and equilibrium moisture contents, respectively. Note that instead of the reduced moisture content M , some other studies [27, 28] used the MC or the water concentration [29]. The accuracy of the solutions improved with diffusion coefficients given by the exponential expression in 2.6 instead of constant ones. The values for beech diffusion coefficients determined in this study are summarized in table 2.1.

Wood direction	$D_0 \cdot 10^{-10} (\text{m}^2 \text{s}^{-1})$	d
Longitudinal	7.53	
	30.08	-1.73
Radial	1.50	
	2.46	-0.66
Tangential	0.39	
	0.54	-0.16

Table 2.1: Identified diffusion coefficient for beech.

More recently, two studies [30, 28] proposed a relationship for diffusion coefficients of spruce and glue line in laminated boards. These works also brought to light that the coefficients of various synthetic adhesives are some order of magnitude lower than those of the wood and therefore offer some resistance to moisture transport. The behavior of the welded joint toward moisture transport is unknown, but is important to determine if one wants to express the MC field of a welded piece and all the resulting phenomena in terms of induced stresses or varying properties.

2.1.3 Mechanical behavior

Elastic behavior

In linear elasticity, the strains and stresses are linked by the generalized Hook's law.

$$\epsilon_{ij} = C_{ijkl} \sigma_{kl} \quad (2.8)$$

\mathbf{C} is the elastic compliance matrix whose Voigt notation, for an orthotropic material, is symmetric and expressed by nine independent variables [31].

$$\mathbf{C} = \begin{pmatrix} \frac{1}{E_t} & -\frac{\nu_{rt}}{E_r} & -\frac{\nu_{lt}}{E_l} & 0 & 0 & 0 \\ -\frac{\nu_{tr}}{E_t} & \frac{1}{E_r} & -\frac{\nu_{lr}}{E_l} & 0 & 0 & 0 \\ -\frac{\nu_{tl}}{E_t} & \frac{\nu_{rl}}{E_r} & \frac{1}{E_l} & 0 & 0 & 0 \\ 0 & 0 & 0 & \frac{1}{G_{tr}} & 0 & 0 \\ 0 & 0 & 0 & 0 & \frac{1}{G_{rl}} & 0 \\ 0 & 0 & 0 & 0 & 0 & \frac{1}{G_{tl}} \end{pmatrix} \quad (2.9)$$

In this case, and for the compliance matrix to be symmetric, $\nu_{tr}/E_t = \nu_{rt}/E_r$, $\nu_{tl}/E_t = \nu_{lt}/E_l$ and $\nu_{rl}/E_r = -\nu_{lr}/E_l$. Values for the elastic constants from literature [32, 33] are given in table 2.2 and are used as a reference throughout this work. The properties of spruce are given to compare hard and soft woods.

According to Dinwoodie [33], the modulus are MC dependent and given by equations 2.10 and 2.11

$$E_d = E_{ref} [1 + 0.015 (u_{ref} - u)] \quad (2.10)$$

$$G_d = G_{ref} [1 + 0.025 (u_{ref} - u)] \quad (2.11)$$

With the subscript d indicating the direction of the property and E_{ref} and G_{ref} the modulus at $u_{ref}\%$ of MC. According to the results of Hering et al. [34], the MC changes seem to have little effect on the Poisson's ratios and they will consequently be considered as constant throughout this work.

Species	E_l	E_r	E_t	G_{lr}	G_{lt}	G_{rt}	ν_{lr}	ν_{lt}	ν_{rt}
	[GPa]						[-]		
Spruce	10	0.8	0.45	0.8	0.9	0.08	0.37	0.47	0.43
Beech	14	2.28	1.16	1.64	1.08	0.47	0.45	0.51	0.75

Table 2.2: Elastic constants given in the literature for beech and as comparison with a softwood type (spruce)

Hygro-mechanics

In an effort to model the hygromechanical behavior of drying board, Ormarsson et al. [6] developed a model based on the strain rate. It is assumed that the total strain rate $\dot{\epsilon}$ is the sum of the strain rates due to mechanical loadings $\dot{\epsilon}_{el}$ (presented above), due to swelling or shrinkage $\dot{\epsilon}_{MC}$ and a coupled strain rate between mechanical loads and moisture changes; the mechano-sorptive strain rate $\dot{\epsilon}_{MC\sigma}$. Viscoelasticity and mechano-sorption are needed to model the hygro-mechanical behavior of wood over long time periods and in changing RH conditions, which is not the case in this work.

$\dot{\epsilon}_{el}$ can be derived from equations 2.8 and 2.2. $\dot{\epsilon}_{MC}$ and $\dot{\epsilon}_{MC\sigma}$ are dependent on the rate of moisture change \dot{u} .

$$\dot{\epsilon}_{MC} = \alpha \dot{u} \quad (2.12)$$

$$\dot{\epsilon}_{MC\sigma} = m \sigma |\dot{u}| \quad (2.13)$$

$\alpha = (\alpha_t, \alpha_r, \alpha_l, 0, 0, 0)^T$ is defined by the strain moisture induced coefficients, i.e. the percentage of dimension change per percentage of MC change. m is a matrix containing mechano-sorption coefficients for the coupling of the mechano-sorptive strains. Additional use of this model in other studies [7, 8] has shown that material properties must be carefully determined as well as the cylindrical material orientation.

2.2 Fracture mechanics

2.2.1 Basics of linear elastic fracture mechanics

The design of structures based on the strength properties of a material assumes a homogeneous and idealistic material without any defects. During the 19th century, many accidents occurred due to unexpected failure, which highlighted that pre-existing flaws and cracks in the structure can lead to stress concentration and early failure [35].

The problem was first studied by Griffith [36] who considered an energetic approach and performed the energy balance of a cracked body:

$$U = U_s + U_p + W \quad (2.14)$$

where U is the total energy, U_s and U_p are the strain and potential energies, respectively, and W is the surface energy due to crack formation, i.e. the formation of two new surfaces of length $2a$ ($W = 4S\gamma$). The potential energy is equal to the additive inverse of the work F of the applied loads. At equilibrium, the expression can be written as:

$$\frac{dU}{dS} = \frac{d}{dS}(U_s - F + W) = 0 \quad (2.15)$$

or

$$\frac{d}{dS}(F - U_s) = \frac{dW}{dS} \quad (2.16)$$

dS is the surface increment of the crack. The left hand side of equation 2.16 is the energy available for crack propagation called the energy release rate (ERR) and is represented by the symbol G .

$$G = \frac{d}{dS}(F - U_s) \quad (2.17)$$

The right hand side of equation 2.16 represents the resistance R to crack propagation. A critical state is reached at the onset of crack propagation when the ERR is equal to R and is denoted as critical ERR or G_c .

In the elastic case of the loading of a body with a crack at a constant displacement δ (i.e. displacement control), the variation of potential energy during a crack length extension of da is given by:

$$dU_s = \frac{1}{2}\delta dP \quad (2.18)$$

Since no displacement occurs, the work of the external load is zero and, according to equation 2.17, the ERR can be written as:

$$G = -\frac{\delta}{2b} \frac{dP}{da} \quad (2.19)$$

With b the width of the body. Considering the compliance C as the ratio of the displacement

and the load, one has:

$$\delta = CP \quad (2.20)$$

and by derivation of equation 2.20 with respect to a and insertion in 2.19, one finally has an expression for the ERR:

$$G = \frac{P^2}{2b} \frac{dC}{da} \quad (2.21)$$

A similar analysis in the case of load control leads to an equivalent relation, thus showing that the ERR does not depend on the loading type.

Another approach of fracture mechanics involves expressing the stress field around the crack tip with a parameter that enables computing the stress components in the vicinity of the crack tip. K_i is called the stress intensity factor (SIF) in mode i (see below) and is dependent on the far field stress, the crack length and the geometry of the problem. Similar to the ERR, a critical value of the SIF can be considered as a material property defining the resistance of the material to crack propagation.

In a solid, a crack can be loaded in three basic modes, as illustrated in figure 2.3.

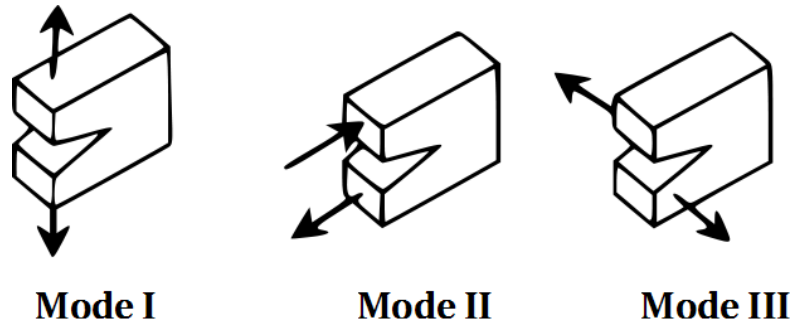


Figure 2.3: Illustration of the three basic modes of crack loading.

Mode I, or opening mode, occurs when the stresses are normal to the crack plane. Mode II, or sliding mode, occurs when the stresses are parallel to the crack and cause in-plane shear. Mode III, or tearing mode, is due to shear stresses in the second direction of the plane (out-of-plane shear). However, in real structures with complex shapes and loading conditions, mixed mode condition is most likely to occur, i.e. that not only one of the pure modes applies at the crack tip but a combination of several of them. In this case, the ERR corresponding to

each pure mode can be added to compute the total ERR in the mixed mode.

$$G_T = G_I + G_{II} + G_{III} \quad (2.22)$$

The previous relations were developed within the frame of the linear elastic fracture mechanics (LEFM), i.e. for materials that exhibit brittle behavior. However, this is not the case for most materials, because many phenomenon like plasticity, micro-cracking, friction or fiber bridging can dissipate energy and act as toughening mechanisms. A fracture process zone (FPZ) can develop ahead of the crack tip and thus R will no longer remain constant, but instead becomes a function of the crack length. This is the so called R -curve behavior. However, many materials such as wood or concrete for example are considered as "quasi-brittle" [37], since they show limited strain hardening before their maximal strength, but exhibit a softening behavior due to the FPZ. In such a case, Hillerborg [38] developed the concept of fictitious crack to account for the FPZ where a portion of the crack undergoes non-constant closing stresses.

2.2.2 Mode I fracture in the wood field

There are overviews concerning the fracture properties of wood in the works of Stanzl-Tschegg and Navi [39] and Navi and Stanzl-Tschegg [40]. During crack propagation, softening behavior is reported and fiber bridging occurs behind the crack tip. Like the other mechanical properties of wood, the fracture characteristics are also influenced by moisture, i.e. they tend to decrease with increasing MC [41, 42, 43]. The maximal value of the stress intensity factor (i.e. fracture toughness K_{Ic}) is reached at 16% MC [44] or between 7% and 13% MC [45]. Prokopski [46] even found an opposite trend of K_{Ic} with MC of oak and pine. Obviously, the correlation between MC and crack resistance is not clear in all aspects.

Experimental testing methods for mode I fracture in wood include the DCB [47, 48, 49], the wedge splitting [50, 51, 52] or bending test with single edge notched beam (SENB) specimens [53, 54, 55, 56, 57]. For mode I fracture of glued wood investigations, the DCB specimens is frequently applied due to its simplicity in processing [58, 59, 60, 61, 62, 63]. Some authors have selected the tapered version of DCB specimens [64, 65, 66, 67] to obtain a linear variation of the compliance with the crack length and increase the chance obtaining a stable crack propagation. It is generally agreed that wood can be considered as a quasi brittle material and that a cohesive zone (or FPZ) develops at the front of the crack tip. Therefore, some authors [54, 68, 69] used the concept of equivalent crack length and modeled the crack propagation with a cohesive bilinear law accounting for the micro-cracking ahead of the crack tip and fiber bridging behind it.

2.2.3 Mode II fracture in the wood field

Mode II fracture in the field of plain wood and wood joined with conventional adhesives is already well documented. Among different specimen types used to investigate mode II fracture, the end notched flexure (ENF) specimen is common, since stable crack propagation is normally observed. In the literature, the RILEM TC 133 report [70] gives an interesting overview of early work to determine fracture energy (G_f) with the help of a tapered ENF. In this work, the specimens are further separated under opening mode, after crack propagation using the ENF 3 points bending (3-ENF) test. The differences in fracture surfaces morphology enable measuring the crack propagation length in mode II and therefore G_f . While the influences of several experimental parameters were studied, the conclusion on the effect of MC of the wood was that dry specimens (< 5%) showed unstable fracture. Non-tapered specimens are also used with either the 3-point or 4-point bending (4-ENF) test. The drawback of the former test is that it gives stable crack propagation only when the initial crack length to half span length ratio is greater than 0.7 [71, 72]. Although the 3-ENF is a convenient simple setup to measure G_{II} at crack propagation initiation, the 4-ENF test is better, due to a resulting longer zone of stable crack propagation. In composites, Schuecker and Davidson [73] have validated the use of the 4-ENF test to measure G_{IIc} . Conditions for an accurate computation of G_{IIc} are that the crack length should be measured several times and with sufficient precision. The 3-ENF test was also used in the field of wood adhesive joints [65, 74, 75].

2.2.4 Mixed mode I/II fracture in the wood field

Several types of specimens to test wood and wood joints' mixed mode fracture have been suggested in the literature. Among the most used, one can find the mixed mode bending test (MMB) [76, 77], the single leg bending (SLB), the asymmetrical DCB [78] or the asymmetrical wedge splitting [79]. Singh et al. [80] and de Moura et al. [81] focused on the mixed mode fracture of adhesive wood bonds. In this case, the propagation of the crack is usually constrained at the interface between the wood pieces, i.e. in the joint interphase. In an early work, Valentin and Caumes [82] reviewed different kinds of specimens to test pure and mixed modes fracture and suggested the use of compact tension shear (CTS) specimens associated with an Arcan device for wood mixed mode fracture investigations. Since then, various studies have used different versions of the Arcan device first developed by Banks-Sills et al. [83] to test, for example, interfacial and adhesive failure [84, 85, 86, 87, 88], shear properties of wood [89, 90] or fracture properties of wood [82, 91, 92]. Moutou Pitti et al. [93] suggested a modified CTS specimen shape that allows stable crack propagation in mixed mode. In all these works, the authors highlighted the ability of the Arcan test to provide a wide range of various mixed modes with the same specimen dimensions, simply by rotating the testing device. Recently, Ginest et al. [94] used the Arcan device to compare the strength values of solid and welded beech, but since no cracked specimens were used in this work, data on the energetic fracture criteria for welded wood joints under mixed mode conditions could not be determined. Bending tests with SENB specimens are usually used to test mode I fracture, (see section 2.2.2), but one can

find examples where it is used for mixed mode testing by varying the angle of the crack to vary the mixed mode ratio [95]. An analogue test in the wood field is mentioned in Petersson [96] to illustrate "mildly non linear " compared to a "catastrophic" load-displacement structural behavior of the wood beam with a notch. In this case the crack propagates not in the notch direction, but perpendicular to the notch, thus following the grain of the wood.

2.3 Friction welding of wood

2.3.1 Welding technology

The welding of wood is a connection method between wood pieces without addition of any adhesive. It is based on the friction welding process already well known in the metal and polymer fields. Welding of wood was first mentioned by Suthoff et al. [97] who suggested a joining method for wood pieces without glue with the help of a rotational or linear friction movement. In the early 2000's, welding of wood started to be intensively investigated by different research institutes that used different welding technology (see figure 2.4). At the Chair of Timber Construction of the Swiss Federal Institute of Technologies, research using orbital friction technology was conducted [11, 4]. Intensive investigations of linear vibration technology were performed at the Bern University of Applied Sciences [3, 98, 12] and at the LERMAB-ENSTIB of the University of Nancy [99, 100, 101]. Rotational welding was first investigated by Pizzi et al. [102] and Kanazawa et al. [103]. Rotational welding technology has been applied to structural building elements [104, 105] and exterior applications [106, 107] with satisfactory results.

2.3.2 Microstructure of the welded joint

Gfeller et al. [3] concluded in their work that the adhesion at the interface is generated from wood fibers entangled in a matrix of molted and re-solidified wood substances (figure 2.5(a)). Properzi et al. [108] showed that this fiber-matrix composite is almost absent for some species, like oak for example. In this case, mechanical properties are more sensitive to welding condi-

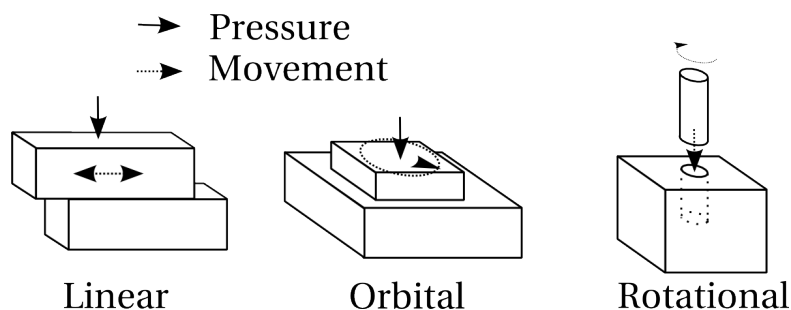


Figure 2.4: Illustration of the different friction welding technologies.

tions because the bonding is ensured by direct welding of the cellular walls of each wood part. The microstructure of the welded joint was studied by X-ray micro-densitometry [99, 108] and by confocal [11], optical [98] and SEM [109, 11, 12]. The results revealed that the welding process leads to a certain degree of densification at the interface due to the joining material at the bond location as well as due to the compression of the adjacent wood cells owing to the thermo-mechanical effects. Ganne-Chedeville et al. [98] identified three different anatomical heat affected zones. X-ray computed tomography (CT) was used by Vaziri et al. [110] to evaluate the density of the joint. Correlations were found between the process parameters and the final density. However, the latter could not be correlated with water resistance. In another study, Vaziri et al. [111] showed that CT scanning was a useful tool to detect cracks in a welded joint.

2.3.3 Mechanical properties of the welded joint

The mechanical strength of linear welded joints was investigated by tensile shear tests [112]. Many studies [3, 109, 12, 113] have since sought to optimize these properties by varying the process parameters and conditions (welding time and pressure, amplitude, surface quality, etc). With a welding time of 4.5 seconds and welding pressure of 1.3 MPa and a fixed frequency of 100 Hz, Ganne-Chedeville [12] found that beech joints are able to withstand stresses up to 9 MPa. The same work, plus others [10, 11], concluded that the mechanical strength strongly decreases when in contact with water. The influence of the orientation of the wood fibers on the shear strength is reported in Properzi et al. [108] and Omrani et al. [114], but opposite conclusions were drawn. The difference between these two studies is mainly the welding parameters, which may explain that in some case (longer welding time and lower frequency [108]) a difference was observed between parallel- or cross-grain specimens, whereas no differences

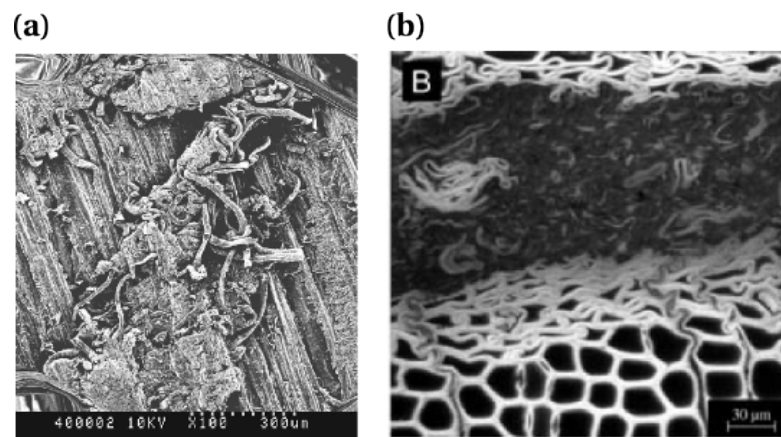


Figure 2.5: (a) SEM picture of joining material composed of wood fibers embedded in a molten lignin matrix [3]. (b) Confocal microscopy of a welded joint with densified zones on both sides of the joint [4]

were apparent in the study of Omrani et al. [114]. However, the testing method could also be questionable, since the wood single lap configuration with a cross-grain specimen induces tensile stresses in the radial direction that are close to the maximal strength.

A study led by Mansouri et al. [100] showed that the use of a 150 Hz welding frequency enables to decreasing the welding time and thus avoiding fibers expelling at the interface and char formation. In that way, it seems possible to improve the shear strength and water resistance and also highlight the strong influence of the process parameters. Differences due to welding frequency were also observed by Delmotte et al. [115] at the chemical level. The mechanical strength properties of welded joints of beech were studied by Ginest et al. [94] in tension and shear, as well as in mixed loadings using an Arcan device. The maximal strength for the pure mode loadings are unexpectedly low compared to previous works (1.73 and 4.64 MPa respectively for tension and shear).

In order to evaluate the fracture characteristics of the welded joint, Ganne-Chedeville et al. [116] used a double cantilever beam (DCB) test with an experimental compliance method that enabled measuring the mode I critical ERR of welded joints at MC levels of around 12%. Values obtained are in the same range as standard adhesives, i.e 106 J m^2 , however a high variability was also reported. Omrani et al. [101] performed the same test but with parameters associated with a 150 Hz frequency and studied the influence of fibers orientation and wood species on the value of G_{IC} .

2.3.4 Numerical modeling of the welded joint

Prediction of the strength of a welded assembly by a numerical model was investigated by Vallée et al. [117] and Hahn et al. [118]. The variability of the experimental results was taken into account with a probabilistic method based on Weibull's statistics. Good agreement was found between the model failure prediction and the experimental results. Oudjene et al. [119] proposed FE numerical analysis of wood pieces assembled with the help of welded dowels. The plasticity of wood was taken into account and the joint was modeled as a master-slave contact with a Coulomb friction model. The failure was considered as brittle and the model showed good correlation with experimental data, although no characterization of the mechanical properties of the joint were performed.

2.4 Summary

In this chapter, the general structure and properties of the wood material are presented. The intense work already carried out on wood fracture mechanics shows the importance of the topic, but the complexity of the material leads to challenging issues and sometimes contradictory results. Few studies about the fracture of welded joints are available and have been, until now, limited to MCs of around 12%. Most of the mechanical investigations carried out on the welded joints involved measuring the shear strength, and the water resistance is

evaluated by measuring the evolution of the shear strength after a given immersion time in water. However, no study gives a systematic relationship between MC and properties, such as strength or fracture properties. Furthermore, since the fracture behavior of the welded joint is not fully characterized, no model is available to describe the delamination of the welded pieces.

3 Materials and methods

Throughout this work, several experimental methods are used to characterize the material properties. The following chapter explains the preparation of the specimens and describes the experimental and numerical methods. At the beginning of the chapter, the welding process for the preparation of the specimen is described and for consistency, the welding parameters are kept constant. Numerical methods to model fracture of the joint are compared and a model for the wood material is given. Then the following sections describe in detail the various experimental methods and the corresponding numerical models that are used in the different chapters of this work.

3.1 Wood preparation and friction welding process

Beech (*Fagus sylvatica*) wood planks are cut out of the same tree trunk and stored in a climatic chamber (20° C / 65% RH). At EMC, beams with desired dimensions are machined and the thickness is reduced with a planing machine. The exact dimensions of the parts to be assembled by welding depend on the anticipated tests and are presented in the next sections.

Linear friction welding is used to join the wood parts together in order to produce usable pieces to be subsequently machined and tested. The welding process is divided into two steps, namely the friction and the holding steps. During the friction step, an oscillating movement is imposed onto the upper table of the machine by an electromagnetic system through a metallic spring. The oscillation's frequency is given by the natural frequency of the table and the spring, and is, in the frame of this work, around 100 Hz. The amplitude can be set between 2 and 4 mm and is chosen to be 3 mm. Pressure is applied by a hydraulic system on the lower table. For this work, the pressure is kept constant and equal to 1.5 MPa. During the holding step, the pressure stays the same as during the welding step, but the oscillation is stopped. A summary of the welding parameters is shown in table 3.1 and figure 3.1 presents the welding machine.

If not mentioned otherwise, the direction of the oscillations corresponds to the longitudinal directions of the wood parts. The angle of the year rings with the welded interface is kept

Friction			Holding	
time [s]	pressure [MPa]	amplitude [mm]	time [s]	pressure [MPa]
2.4	1.5	3	7	1.5

Table 3.1: Welding process parameters for specimens production

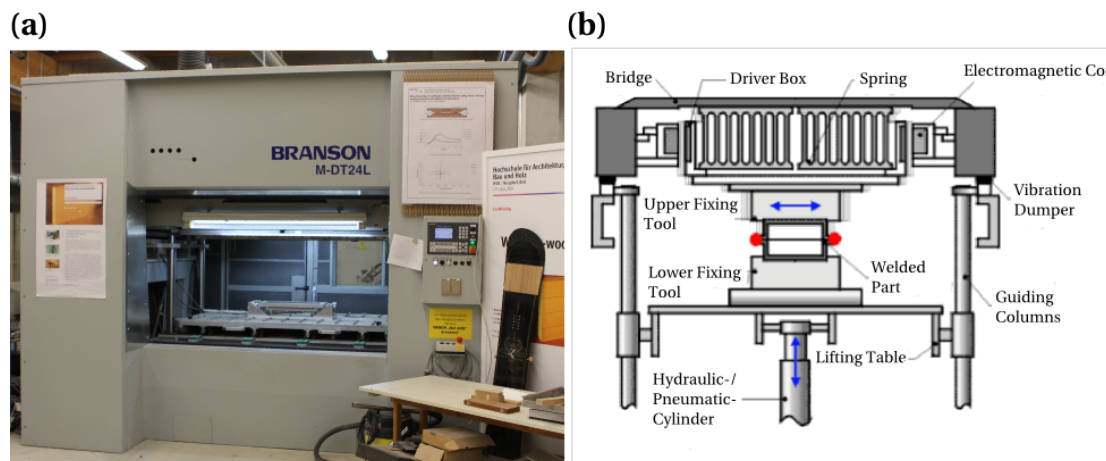


Figure 3.1: (a) Photograph and (b) syochematic representation of the welding machine (www.bransoneurope.eu).

constant and equal to 90° (i.e. the tangential direction of the wood is normal to the welded interface). The size of the welded pieces and the way they are machined to produce the specimens are further explained in the following sections of this chapter.

3.2 Moisture related properties

3.2.1 Equilibrium state

When needed, the RH of the environment (e.g. in desiccators or climatic boxes) is tailored with saturated salt solutions. The list of all the salts used during this work is shown in table 3.2. A slight variation of the real RH from the expected one is possible depending on the temperature and purity of the solutions but the exact EMC of the wood is always determined with control specimens by the oven dry method [13].

The determination of densities, hygro-expansion coefficients and EMCs is performed by placing wood specimens in a desiccator with the appropriate salt solution. At equilibrium, the mass and dimensions of each specimen is measured and the exact RH is read on a data logger located in the desiccator. The specimens cut out of a plank have initial dimensions of $10 \times 10 \times 50 \text{ mm}^3$ and are first oven dried to reach 0 % of MC. They are then placed stepwise in different climatic conditions with ascending RH. The temperature is controlled and kept constant at

23°C and four specimens for each direction are tested.

Salt	Abbreviation	Expected RH (%)
Potassium hydroxide	KOH	9
Potassium acetate	CH ₃ COOK	22
Potassium carbonate	K ₂ CO ₃	44
Sodium nitride	Na ₃ N	65
Potassium chloride	KCl	85
Ammonium dihydrogenphosphate	NH ₄ H ₂ PO ₄	93
Potassium sulfate	K ₂ SO ₄	97

Table 3.2: Salts used to set the RH in climatic boxes

3.2.2 Moisture transport

Specimen and setup

The first step of the specimen preparation consists of the joining, which is achieved by welding 3 wood parts (500 x 90 x 15 mm³) to produce 3-layer pieces (figure 3.2(a)). Prismatic specimens shown in figure 3.2(b) (90 x 90 x 45 mm³) are machined out of these pieces and the lateral and bottom surfaces are sealed with aluminum tape to avoid moisture diffusion through these surfaces.

In a second step, the specimens are stored in a climatic chamber (20°C / 85% RH) in order to produce a MC gradient between the upper surface and the interior of the welded piece. After a determined amount of time of 12, 27 and 57 days, specimens are taken out of the climatic chamber in group of 5 for a MC assessment of their different layers.

At the exit of the climatic chamber, each specimen is reduced to a size of 60 x 60 x 45 mm³ and then cut in two smaller pieces along the height of the specimen. Finally, small slices parallel into the welding interface are cut in order to have two slices per wood layer (figure 3.2(c)). The slices are weighted and subsequently stored in an oven at 103°C. After complete drying, the MC of each piece is calculated according to the oven-dry method.

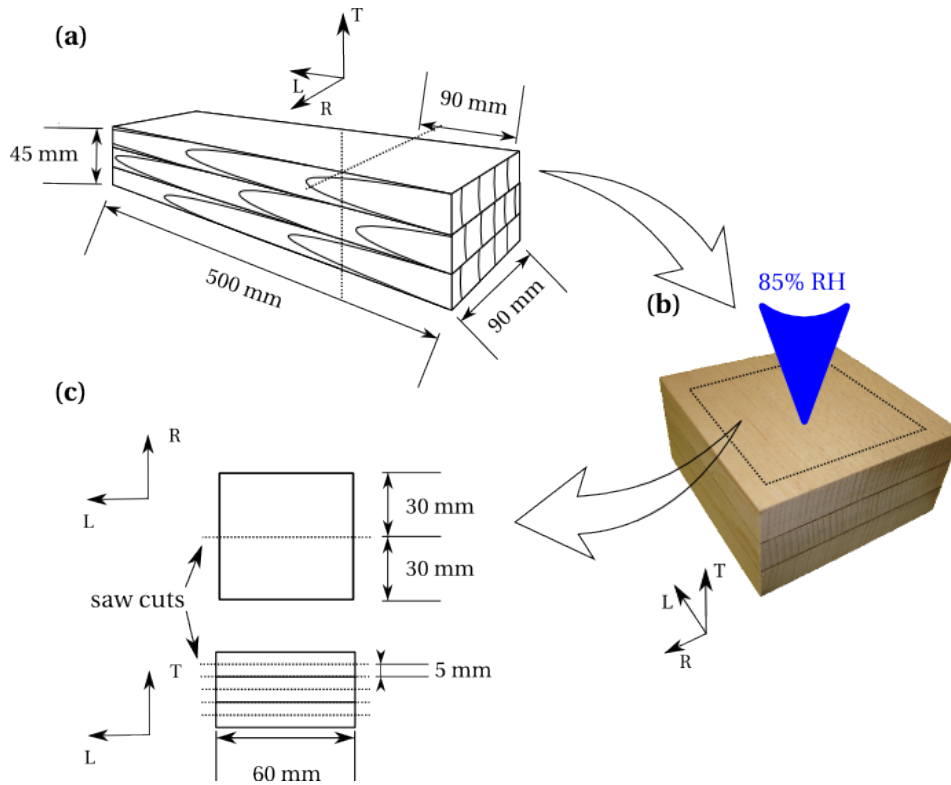


Figure 3.2: (a) Sketch of the 3-layer welded piece. (b) Picture of sample ready to be sealed and stored in new climatic conditions (85% RH). (c) Sketch of the cuts after the diffusion test.

3.3 Mode I testing

3.3.1 Specimen preparation

The wood parts to be welded have the dimensions $500 \times 30 \times 5 \text{ mm}^3$. To introduce an initial crack in the weld, grease is applied on the surfaces to be welded over a distance of 100 mm to avoid friction and thus welding during the process. The final geometry of the specimen, designed according to the standard D5528-01 [120], is shown in figure 3.3.

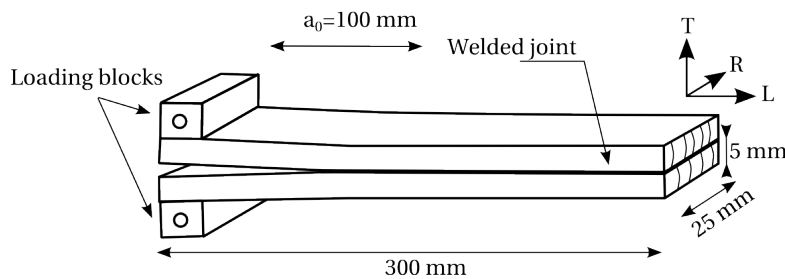


Figure 3.3: Sketch of the DCB specimen.

Four groups of five samples each are placed into four climatic boxes with different RH, attained by equilibrium of the environment with saturated salt solution (for details see table 3.2). The following four MC levels are measured and considered: 6.4, 12.0, 16.2 and 22.0%.

Once EMC is reached, the dimensions of the specimens are measured and their lateral surfaces are covered with a white brittle paint and vertical thin lines are drawn every millimeter to help track crack propagation during testing. Lastly, aluminum blocks with a through hole are glued on the extremities of the beams to serve as load application pins.

3.3.2 DCB test

The DCB specimens are tested on a uniaxial testing machine (INSTRON 5848 Microtester) with a 2 kN load cell and constant pulling rate of 2 mm min^{-1} (see figure 3.4). Pictures are taken of the lateral marked surface at regular time intervals during the test with the help of a camera Guppy from Allied Vision Technologies equipped with a 50 mm lens. It follows that the crack tip position can be measured with a precision of $\pm 0.5\text{mm}$, which is considered accurate enough given the relative total length of the crack. During the test, load, displacement, and photographs of the advancing crack tips are recorded and stored for evaluation. Given the low load levels that are reached, it is considered that the stiffness of the machine is high enough so that the cross beam displacement is equal to the loading point displacement. The mass is measured after removing the specimens from the box, as small variations of the specimen's MC may occur. The MC loss during testing is very small and its effects are negligible.



Figure 3.4: Experimental configuration of the DCB test

3.4 Mode II testing

3.4.1 Specimen Preparation

The specimen preparation of beech wood and the welding parameters are similar to that of the DCB specimen presented in section 3.3.1. Grease is applied on the surface to avoid welding and thus create the initial crack starter at 95 mm from the loading point. A sketch representing the geometry of the specimens is presented in figure 3.5.

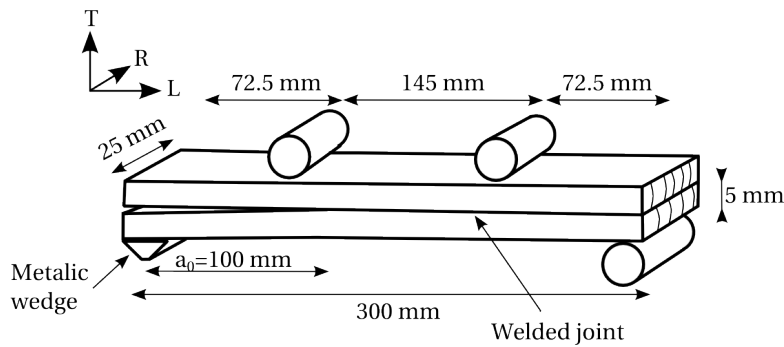


Figure 3.5: Sketch of the geometry of the ENF specimen and the test configuration.

The methodology to obtain samples with determined EMCs is also the same as in section 3.3.1. Control specimens show that the following EMCs are obtained: 6.1, 11.9, 16.8 and 22.1%. To avoid friction between the specimen and the supports, the supports are mounted on roller bearings. To impede the specimens from sliding away, a metallic wedge with a triangular section is glued onto one of the beam's extremities. Specially designed roller prevents the specimen from sliding during loading (see figure 3.6(b)). Before testing, the initial crack tip position is enlarged to 100 mm by inserting a razor blade between the wood beams. This step should sharpen the initial crack tip and facilitate crack growth.

3.4.2 4-ENF test

The four point bending test is performed on a uniaxial testing machine (INSTRON 5848 Microtester) with a 2 kN load cell that is mounted above the upper supporting arm. The setup is designed to minimize friction between the specimen and the setup's supports, i.e., all four supporting cylinders are mounted on roller bearings. One of the lower supports is machined to fit the wedge block glued on one of the specimen's beams (see figure 3.6(a)). Furthermore, to avoid friction between initial crack faces, a Teflon sheet is inserted in the crack prior to the test.

The span between the lower supports is 290 mm long and the span between the upper supports is set equal to one half, i.e. 145 mm. With this configuration, the initial crack tip is located in between the two upper supports, at a distance of 27.5 mm to the nearest support (i.e. left). The

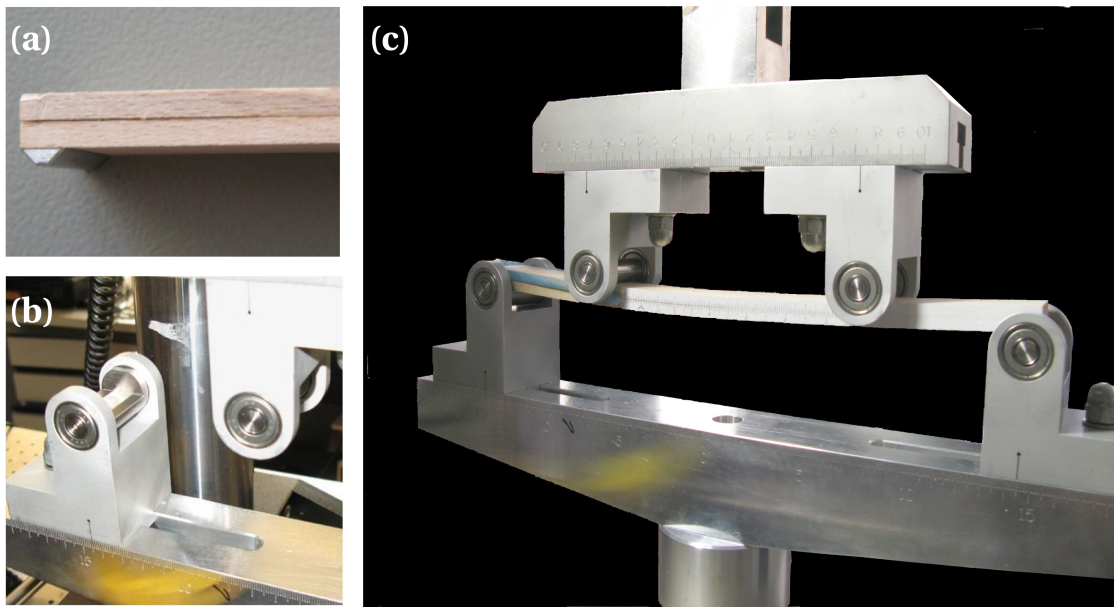


Figure 3.6: (a) Metallic wedge glued on the specimen's lower beam and (b) detail of the lower support with a machined notch in the roller. (c) General view of the configuration of the 4-ENF setup for mode II testing.

upper part is pushed down at a constant displacement speed of 2 mm min^{-1} and the load and cross-beam displacement are recorded every 2 s. To track the crack advancement, pictures of the lateral marked surface are taken every second

3.5 Maximal strength testing

3.5.1 Tensile specimen

The initial wood parts to be welded have the dimensions $500 \times 20 \times 30 \text{ mm}^3$ (respectively for l, r and t directions). The welding occurs on the surface $500 \times 20 \text{ mm}^2$. Half of the welded piece serves to manufacture the uniaxial tensile specimens and the other one for the torsion specimens described in section 3.5.3. The thickness is reduced by planing to 10 mm, and 5 mm slices are cut with a circular saw. The final shape of the specimen is presented on figure 3.7(a)). The surface normal to the longitudinal direction is polished with 240 and 800 SiC paper, which lets the cellular structure of the wood appear. This is necessary for digital image correlation (DIC) studies for surface displacement measurements. The conditions for obtaining the specimens EMC are the same as described in section 3.3.1. A total of eight specimens are tested per condition.

3.5.2 Tensile test

A uniaxial machine is available with a climatic chamber with stable RH and temperature conditions, controlled by appropriate sensors. A glass window adapted on the chamber enables taking pictures of the polished surface (perpendicular to the loading direction) during the test. Right before starting the test, the specimen is clamped in the fixture and the chamber is closed, followed by a waiting time of around 5 min for stabilization of the temperature and RH. The specimen is pulled to failure at a displacement rate of 0.33 mm min^{-1} . After the test, the mass and dimensions of each sample are measured. The natural structure of wood easily enables measuring surface displacements and deducing the strains by DIC with the photographs taken.

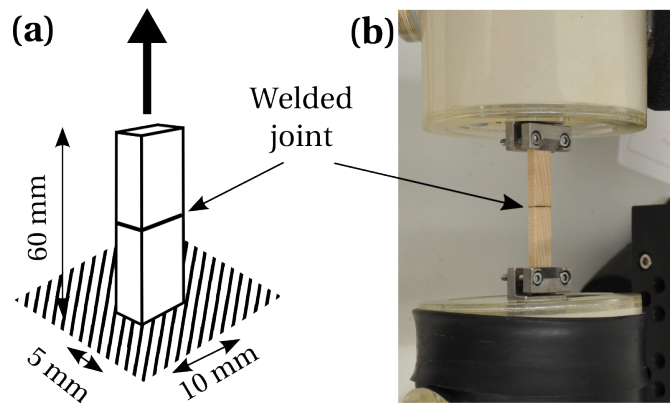


Figure 3.7: (a) Schematic representation of the tensile specimen. (b) Photograph of the tensile test setup.

3.5.3 Torsion specimen

The torsion specimens are prepared with a plug cutter from the other half of the welded piece that the tension specimen were derived from (section 3.5.1). The dimensions of the welded pieces are $500 \times 20 \times 60 \text{ mm}^3$. Thus, the cylindrical specimens with a 15 mm radius are manufactured so that the weld is situated at the middle of the 60 mm long specimen (see figure 3.8(a)). Afterward, four groups of eight specimens each are stored in the climatic box and weighed. One day before the testing, the mass and exact dimensions of the specimens are determined. Then, they are left in the climatic box for one more day. Due to the anisotropic swelling, the section of the specimens at EMC is not circular, but rather slightly elliptical; thus, the dimensions of the two principal axes are measured and used in the shear stress calculation.

3.5.4 Torsion test

The torsion tests are performed on an MTS 809 with an axial-torsional load cell of 10 kN axial load and 100 Nm torque. The specimen is placed in the setup with a 20 mm distance between

the grips and is subsequently loaded at a constant rate of 5° min^{-1} until failure. During the torsional loading, the axial system compensates for displacements such that the axial load is zero throughout the test duration. Torque and angle are recorded at 10 Hz frequency. For the setup and specimen configuration, see figure 3.8.

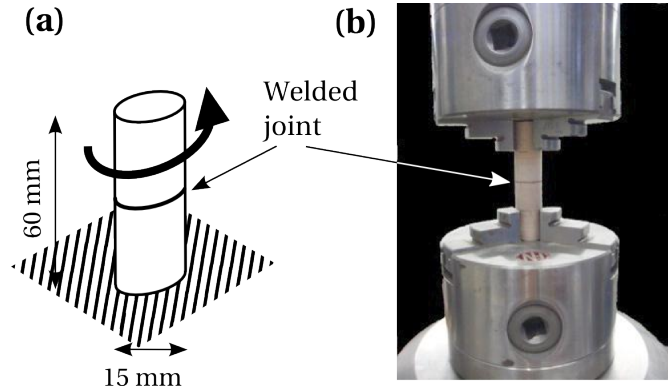


Figure 3.8: (a) Schematic representation of the torsion specimen. (b) Photograph of the torsion test setup

3.6 Arcan test

3.6.1 Specimen preparation

Out of the wood planks, single wood parts are manufactured to permit the welding of parts with various fibers orientations (figure 3.9(a)). The orientation of the fibers are carefully selected to always have the tangential direction of the wood in the direction of the thickness, i.e. perpendicular to the welding plane. The other two directions (radial and longitudinal) are varied for each welded piece type (figure 3.9(a)), which are described according to the angle that the longitudinal direction of each layer makes with the welding oscillation direction (i.e. 0-0, 0-90 and 0-45).

Prior to the welding, the planks are planned and cut to the following dimensions:

- *Long*: $120 \times 55 \times 10.3 \text{ mm}^3$
- *Trans*: $120 \times 90 \times 10.3 \text{ mm}^3$
- *Mid*: $90 \times 90 \times 10.3 \text{ mm}^3$

The denominations *Long*, *Trans* and *Mid* refer to the specimen cutting in different in-plane directions (figure 3.9(b)) that will serve to test the different in-plane directions properties and are machined after the welding process that takes place according to section 3.1.

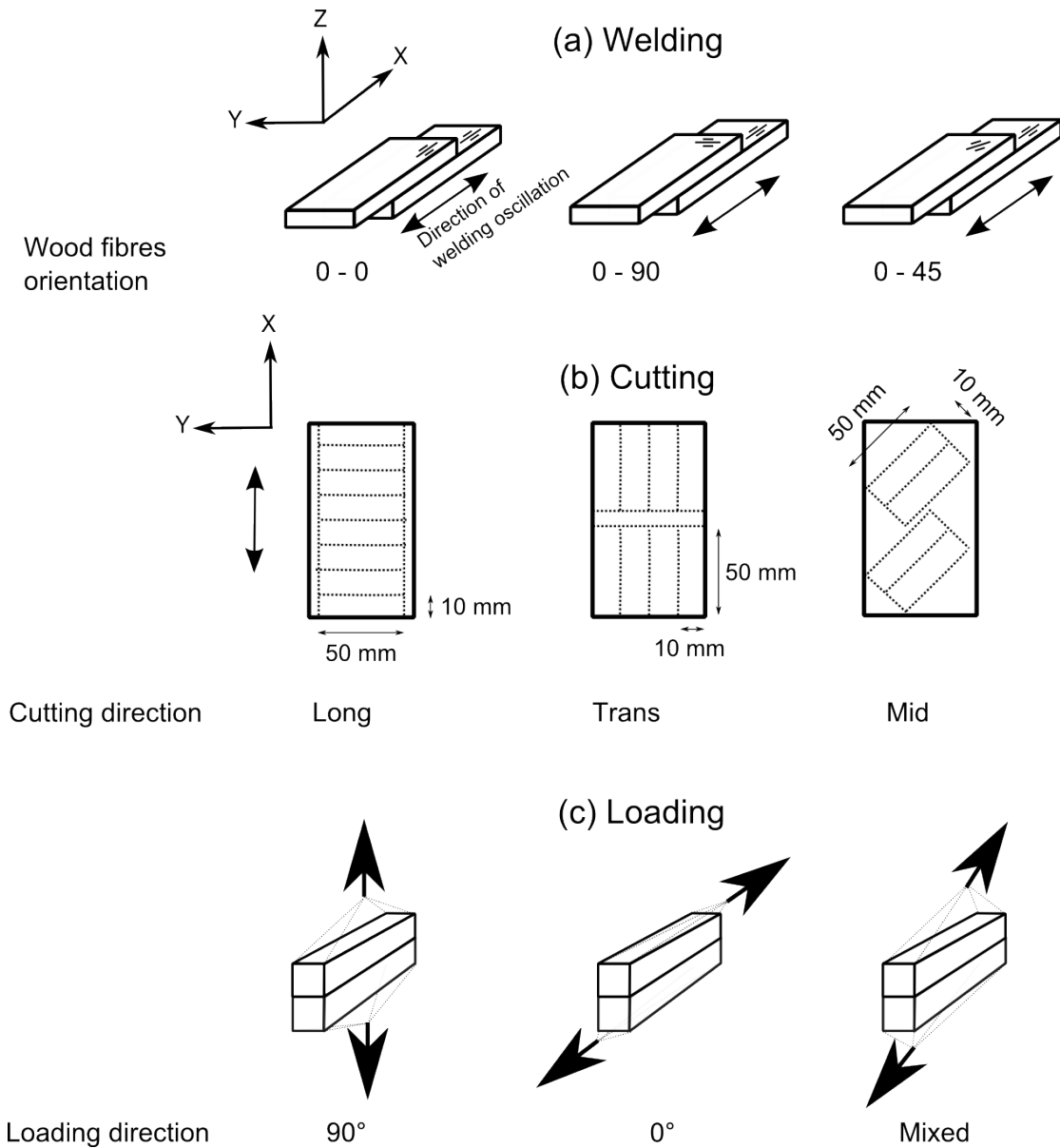


Figure 3.9: Schematic representation of the preparation process and testing of the Arcan specimens. See text for details.

Specimen for strength test

The Arcan device used in this work imposes the following geometrical limitations to the specimens: the height must be equal to 20 mm, the width smaller or equal to 10 mm and the length smaller or equal to 70 mm.

The specimens are initially cut at dimensions of $10 \times 20 \times 50 \text{ mm}^3$, either perpendicular to the direction of the welding oscillations, parallel to the oscillations or at an angle of 45° (see

figure 3.9(b)). A numerical analysis based on the model presented below is used to determine the optimal dimensions leading to the most homogeneous stress distribution on the joined interface and also taking into account practical machining constraints. More particularly, numerical studies are carried out to investigate the effects of side grooves or variation of length. A detailed explanation of these studies is given in section 7.1.1. The details of the geometry used for the experimental work are presented in figure 3.10.

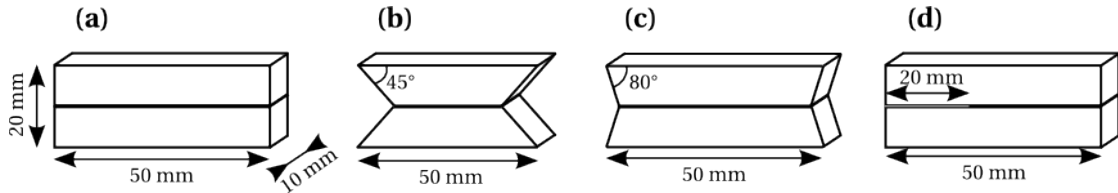


Figure 3.10: Sketch of the Arcan specimens with the dimensions for the strength tests in tension (a), shear (b) and mixed loading (c). (d) represents the specimen for fracture testing.

The specimens and the necessary side grooves are cut using a circular saw and wood support plates are glued with epoxy resin at the top and bottom of each specimen to be inserted in the clamping system of the Arcan device . The final shapes of the specimens are shown in figure 3.11.

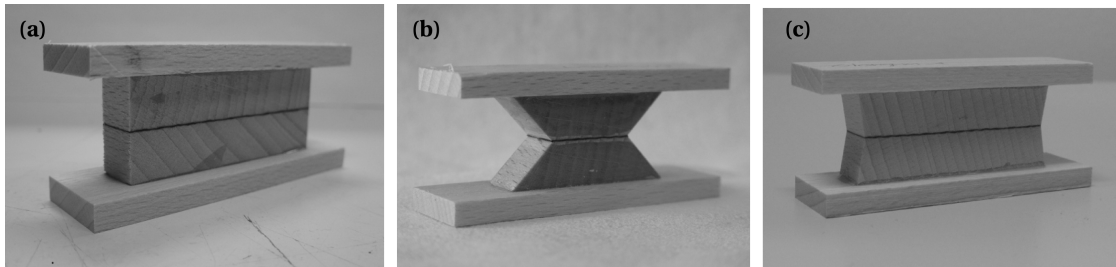


Figure 3.11: Examples of specimens for the Arcan test in (a) tension, (b) shear and (c) mixed loading

Specimen for fracture test

The geometry of the CTS specimens for all fracture tests (i.e. mode I, mode II and mixed modes) are similar to those used for tensile tests (see previous section). Before gluing the support plates, a band saw of 0.3 mm thickness is used to cut a notch from one edge of the specimen, along the joined interface and over a distance of 19.5 mm. To initiate the crack in the joining material, the notch is further increased with the help of a razor blade until it reaches ~20 mm and the length is precisely measured with a binocular magnifier. For the fracture testing, only parallel (0-0) and cross grain (0-90) specimens with the *Trans* cutting direction are produced.

3.6.2 Experimental methods

The Arcan testing device is presented in figure 3.12. The orientation of the device can be varied to reach different loading angles with respect to the weld plane. Shear is achieved with a 0° loading angle and tension with 90° (instigating mode II and mode I for the cracked specimens, respectively). In between, mixed modes are possible with various angle steps of 15° . The same device is used for the strength analysis (with loading angles 0° , 45° and 90°) and for the fracture analysis (with loading angles of 0° , 15° , 30° , 45° and 90°).

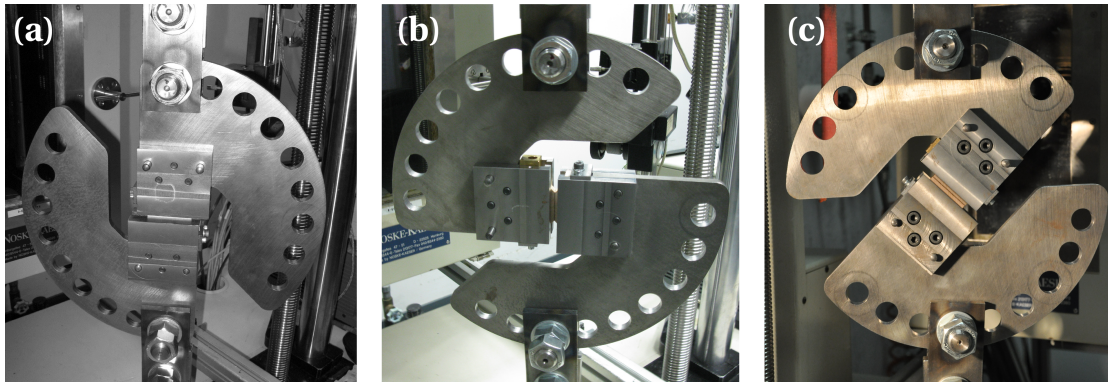


Figure 3.12: Photograph of the Arcan setup mounted for (a) tensile testing, (b) shear testing and (c) mixed mode testing at an angle of 45° .

3.7 Mixed mode crack propagation

3.7.1 Specimen preparation

SENB specimens

The wood plank's thickness is reduced by planing to 8 and 5 mm and subsequently cut to the following dimensions:

- Length = 100 mm
- Width = 80 mm

The planks planned to 8 mm are cut to the above lengths. Whereas, both types of parts with radial and longitudinal directions along the length are produced from the planks planned to 5 mm. The wood parts are selected to have the tangential direction along the thickness. Each welded piece has two layers, with one thick part (8 mm) and one thin part (5 mm) welded together either with the same grain orientation (specimens 0-0) or with cross-grain direction (specimens 0-90).

Three specimens ($100 \times 25 \times 13 \text{ mm}^3$) are cut out of each welded piece and a notch is machined with a 0.3 mm thick band saw in the middle of the thin part until it reaches the joint. The specimen is presented on figures 3.13(a) and (b). To be able to increase the span length while avoiding the effect of the curvature of the year rings in the radial direction, wood piece extensions ($25 \times 25 \times 13 \text{ mm}^3$) are glued with epoxy resin on both sides of the specimens. Before the test, the lateral surface is covered with white paint to allow visual tracking of the crack front.

MMB specimens

From wood preparation until gluing of the loading blocks, the fabrication of the specimens for the MMB test are similar to the DCB specimens used in chapters 3.3.1 and 3.4.1. The final specimens are 300 mm long with a width of 25 mm and a total thickness of 10 mm. An initial crack of 100 mm is induced by the use of grease to avoid friction, and therefore bonding, followed by an initiation in mode I by inserting a metallic blade. To avoid the effect of the curvature of wood year-rings, only 0-0 specimens are prepared.

3.7.2 Experimental methods

4-SENB test

The setup is a 4-pt bending test with a total span length of 135 mm as presented in figure 3.13(c). The decision is made to work with a 4-pt rather than with a 3-pt setup in order to avoid the effect of the upper support in the vicinity of the notch and also to have a constant bending moment along the propagation length. The specimens are placed so that the notch is located in the middle of the span length and polymeric pads are placed between the specimen and the supports of the device to avoid indentation of the wood. The distance between the supports is 45 mm and a Guppy camera is installed to capture pictures of the lateral surface at a frequency of 4 Hz. Calibration of the camera gives a pixel size of $33.07 \mu\text{m}/\text{px}$. The test is carried out at a constant cross-head speed of 3 mm min^{-1} and load and displacement values are recorded at a frequency of 10 Hz. For most of the specimens, monotonic loading until about 2.5 mm of displacement are performed, but two loading-unloading cyclic tests are additionally carried out. On each cycle there is an increment of displacement of 0.5 mm. One cyclic test has no waiting time after each cycle and the second has a relaxation time of 1 hour after each loading and unloading step.

MMB test

A test standard ASTM D6671 [121] is used to calculate the lever length $c = 190 \text{ mm}$ and the half span $L = 145 \text{ mm}$ in order to have a mixed mode ratio of 0.3, which is validated by FE analysis in a second step. The ratio of 0.3 is chosen to correspond to the ratio computed with the VCCT for the 4-SENB configuration. The experimental setup of the MMB is presented in figure 3.14.

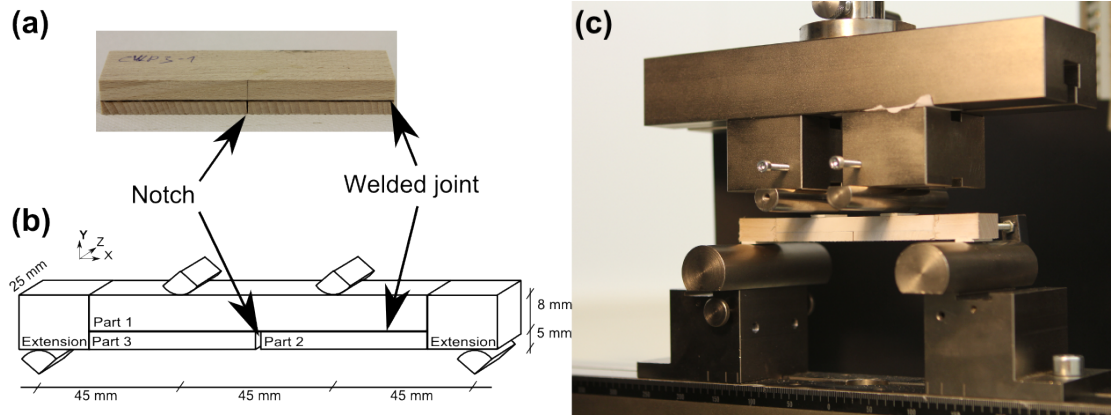


Figure 3.13: (a) Specimen after welding and cutting of the notch in the thin layer (5mm). (b) Sketch of the specimen and the testing situation. (c) Photograph of the setup for 4-SENB

During the test, the loading speed is constant and set to 0.6 mm/min and a picture of the lateral surface is taken with a Guppy every second throughout the test. The load, measured with a 10 kN load cell, and the cross head displacement are also recorded at a frequency of 10 Hz. For one specimen, a cyclic test is performed (4 cycles) at various stages of the crack propagation.

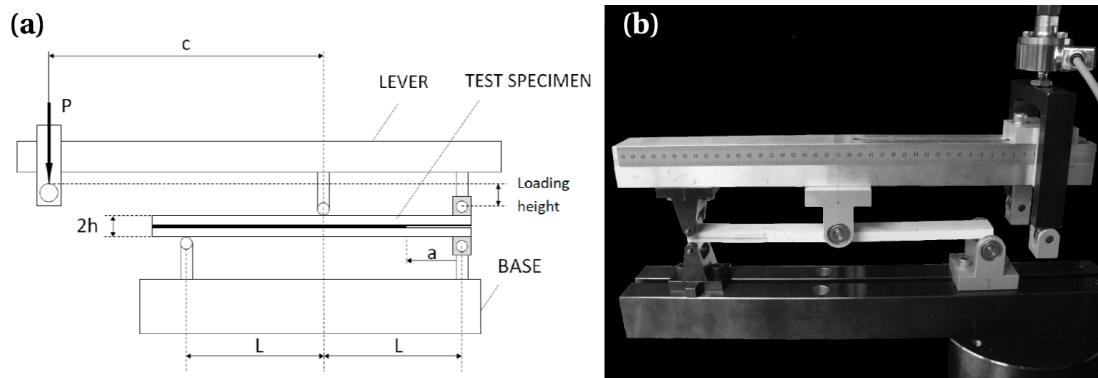


Figure 3.14: Sketch (a) and photograph (b) of the MMB setup

3.8 Fracture of joint modeling

In this work, numerical analysis is generally used to model crack propagation (chapters 5, 6 and 8), but also to help to determine material properties by inverse methods (chapter 4) or by combined work with experimental data (chapter 7) to determine mixed mode fracture characteristics. FE methods are constructed with the commercial software Dassault Simulia Abaqus/CAE 6.12-1.

3.8.1 Cohesive elements models

Cohesive elements are special purpose elements that are used to model the mechanical response of an interface. The behavior of the cohesive elements is defined by a traction-separation law (see figure 3.15) and includes a linear elastic behavior determined by a stiffness E_K , followed by damage initiation and propagation when a maximal nominal stress criterion is reached:

$$Max \left\{ \frac{\langle t_n \rangle}{t_n^0}, \frac{t_s}{t_s^0}, \frac{t_t}{t_t^0} \right\} = 1 \quad (3.1)$$

or when a quadratic criterion is reached, which is used in this work for mixed mode modeling in chapter 8:

$$\left\{ \frac{\langle t_n \rangle}{t_n^0} \right\}^2 + \left\{ \frac{t_s}{t_s^0} \right\}^2 + \left\{ \frac{t_t}{t_t^0} \right\}^2 = 1 \quad (3.2)$$

Subscripts n, s, and t stand for the direction of the nominal stresses when deformation is respectively purely normal to the interface (mode I), purely in the first and second shear directions. The Macaulay brackets indicate that no damage is initiated by pure compressive stresses [122]. The t_n^0 , t_s^0 and t_t^0 are the peak values of the traction-separation law and are directly associated with the maximal tensile and shear strengths of the joint that are experimentally determined during this work.

The advantage of cohesive elements is the possibility to include progressive damage leading to an increase of compliance until failure. This technique accounts for the FPZ ahead of the crack tip where energy is somehow dissipated. It is suitable to model most cases of damage mechanisms and enables combining concepts of fracture and damage mechanics. Using cohesive elements implies that the crack path is predetermined, because the joint is represented by a layer of cohesive elements and the crack cannot propagate outside this region. However, in the case of a wood welded joint at a macroscopic level, the crack propagation is constrained at the interface between the adjacent wood parts and the cohesive elements are perfectly appropriate for this situation.

A sketch of the traction-separation law for mixed mode is presented in figure 3.15. G_{Ic} and G_{IIc} are the critical ERR in the pure modes and represent the area under the damage part of the traction-separation curves. In mixed modes, the total ERR is computed according to equation 2.22 and it represents the area under the damage part of the curve when the criterion

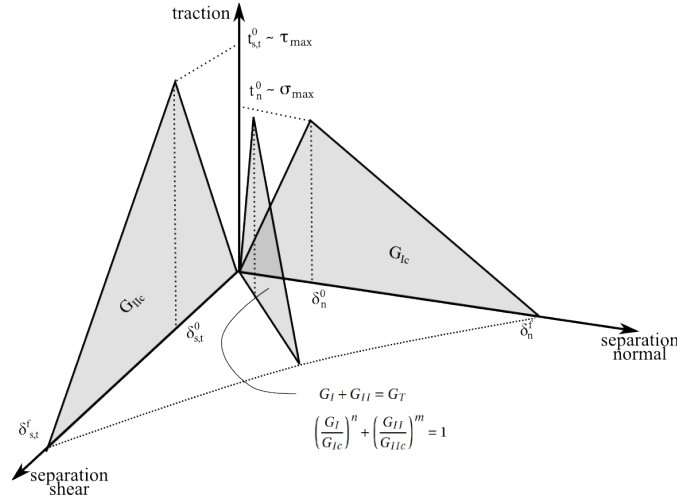


Figure 3.15: Schematic representation of the cohesive law in normal and shear mode as well as in mixed mode.

for mixed mode fracture is equal to one (equation 3.3).

$$\left(\frac{G_I}{G_{Ic}} \right)^n + \left(\frac{G_{II}}{G_{IIc}} \right)^m = 1 \quad (3.3)$$

The joining material is very thin in comparison with the specimen's thickness, thus it does not contribute to the global elastic loading during the tests. However, in the numerical simulation, the elastic stiffness of the cohesive elements cannot be infinite. In this work, it is assumed that the separation value at which damage initiates (δ_n^0) is equal to a tenth of the maximal separation (δ_n^f). Thus, the stiffness of the cohesive elements is calculated with equation 3.4 (here for mode I).

$$E_K = \frac{9(t_n^0)^2}{2G_{Ic}} \quad (3.4)$$

The cohesive layer has a geometrical thickness of 0.150 mm, which corresponds to its real thickness, which can be observed with optical microscopy. However, its constitutive thickness is set to one so that the nominal strains correspond to the separation. The mesh of the cohesive layer is 5 times smaller than the mesh of the wood parts (i.e. 0.1 mm). The cohesive layer is attached to the wood beam with a tie constraint.

3.8.2 VCCT

VCCT is a numerical technique that can be used to compute and separate ERR in the various modes. It is based on the LEFM and makes the assumption that the energy needed to close a crack is equal to the energy released by the opening of this same crack. The principle of calculation are presented in figure 3.16 for a 2D model with four-node elements for the sake of clarity. A more complete description of the VCCT is presented in the paper by Krueger [123].

One can compute the ERR in the basic modes with the shear (w) and opening (u) displacements of nodes m and m^* and the loads applied on node n with equation 3.5 and 3.6. Similar reasoning can be held for a 3D model and to compute G_{III} .

$$G_I = \frac{1}{2\Delta a} P_x (u_m - u_{m^*}) \quad (3.5)$$

$$G_{II} = \frac{1}{2\Delta a} P_y (w_m - w_{m^*}) \quad (3.6)$$

VCCT enables not only modeling crack propagation when a given criterion is fulfilled, but also allows determining the ERRs in all three modes at any loading step. Equation 3.7 gives an energy based crack propagation criterion with a mixed mode power law defined by an

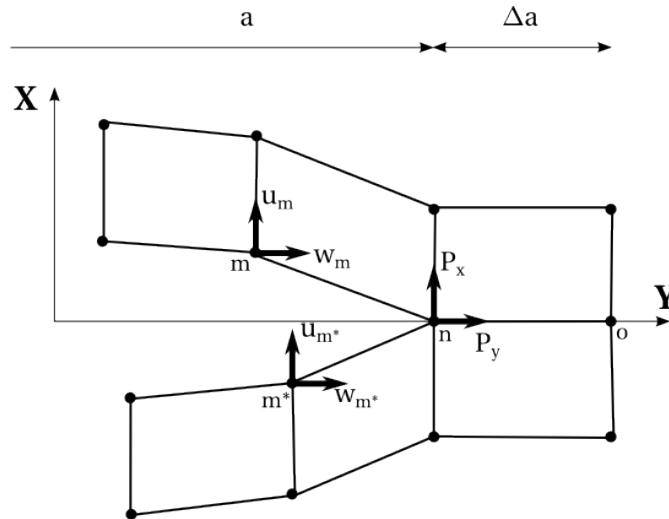


Figure 3.16: VCCT for ERR calculation on a 2D model.

effective ERR ratio.

$$\frac{G_{equiv}}{G_{equivC}} = \left\{ \frac{G_I}{G_{Ic}} \right\}^n + \left\{ \frac{G_{II}}{G_{IIc}} \right\}^m + \left\{ \frac{G_{III}}{G_{IIIc}} \right\}^p \quad (3.7)$$

3.9 Summary

The production of the specimen by friction welding was explained. Then the experimental methods to characterize the wood properties were presented and the first model for moisture diffusion was also presented. An explanation of the preparation the beam specimens and measurement of the fracture characteristics based on standardized methods was given. The Arcan device was introduced as a method for mixed mode fracture investigation that enables measuring both, strength and fracture properties in various loading angles. Two additional methods were presented to investigate mixed mode crack propagation. Finally, cohesive elements and VCCT were introduced to model crack propagation.

4 Moisture related properties

The internal MC and therefore the physical and mechanical properties of the wood are strongly related to the climatic conditions of the surrounding environment. This chapter aims at characterizing the interaction between the wood and the environment in order to determine useful parameters to model the MC field in the welded pieces, which in turn is linked to the elastic properties of the wood and the hygric stress state. The sorption isotherm and expansion coefficients of the wood used throughout the whole thesis are determined. In most of practical applications, the environmental conditions are not stable and transient analysis should be used. To be able to describe the influence of changing humidity conditions, the effect of the welded joint on transient moisture diffusion is studied and diffusion coefficients are identified.

4.1 Equilibrium state

The different equilibrium states obtained in the desiccator at various RH enable computing various physical properties that are presented in table 4.1.

The variations of dimensions relative to the oven dry state enable calculating the expansion coefficient for each direction and the results are presented on the graph and in the table of

RH (%)	MC (%)	Density (g/cm ³)	$\Delta l_l / l_l^0$ (-)	$\Delta l_t / l_t^0$ (-)	$\Delta l_r / l_r^0$ (-)
0	0	0.716	0	0	0
9.9	2.1	0.720	0.0015	0.0108	0.0010
42.9	6.5	0.729	0.0023	0.0203	0.0408
50.7	7.8	0.732	0.0028	0.0228	0.0462
84.2	15.1	0.742	0.0033	0.0381	0.0911
97.0	23.2	0.751	0.0036	0.0514	0.1172

Table 4.1: Moisture dependent properties of the wood.

Chapter 4. Moisture related properties

figure 4.1. These values are consistent with the literature, for example, Niemz [32] reported the following expansion coefficients: $\alpha_l=0.4\%$, $\alpha_r=4.3\%$ and $\alpha_t=13.4\%$.

Figure 4.2 presents the sorption isotherm in black calculated by fitting the values given by Vorreiter [5] for adsorption and desorption of moisture at 20°C. The data determined during this work and in the adsorption phase appears in red in figure 4.2 and lies slightly below the curve at 20°C. Since the temperature is $23 \pm 1^\circ$ the observed tendency is totally normal. The parameters of equation 2.2 that describe the sorption isotherms are given in table 4.2. Thus, the internal MC of the wood can be expressed as a function of the RH of the environment.

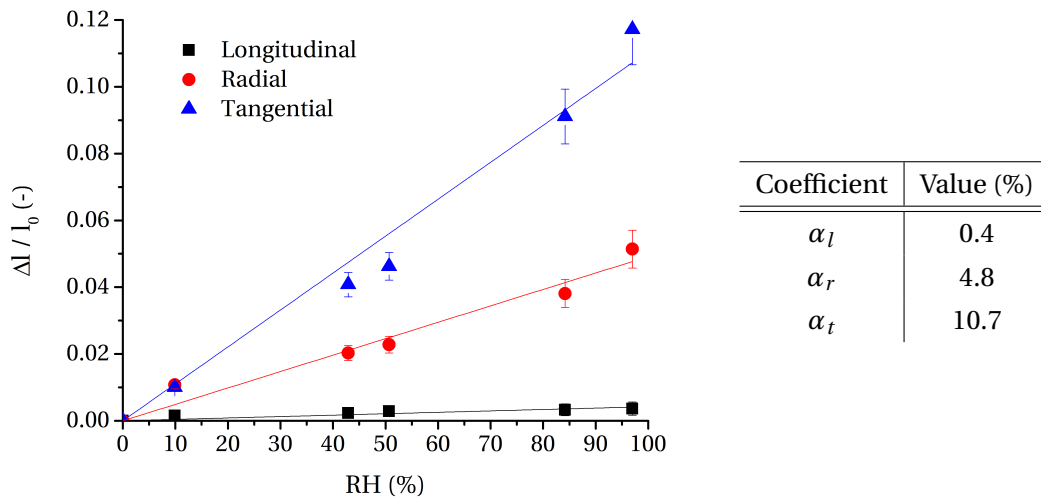


Figure 4.1: left: Evolution of the dimensions with changing MC. right: Corresponding hygro-expansion coefficients in the range of MC from 0 % to the FSP.

Parameter	20°C		23°C
	Adsorption	Desorption	Adsorption
A	1.5531	1.5199	3.0635
B	$1.4152 \cdot 10^{-1}$	$1.6226 \cdot 10^{-1}$	$1.4107 \cdot 10^{-1}$
C	$1.2251 \cdot 10^{-3}$	$1.4293 \cdot 10^{-3}$	$1.3338 \cdot 10^{-3}$

Table 4.2: Parameters of the sorption isotherm curve.

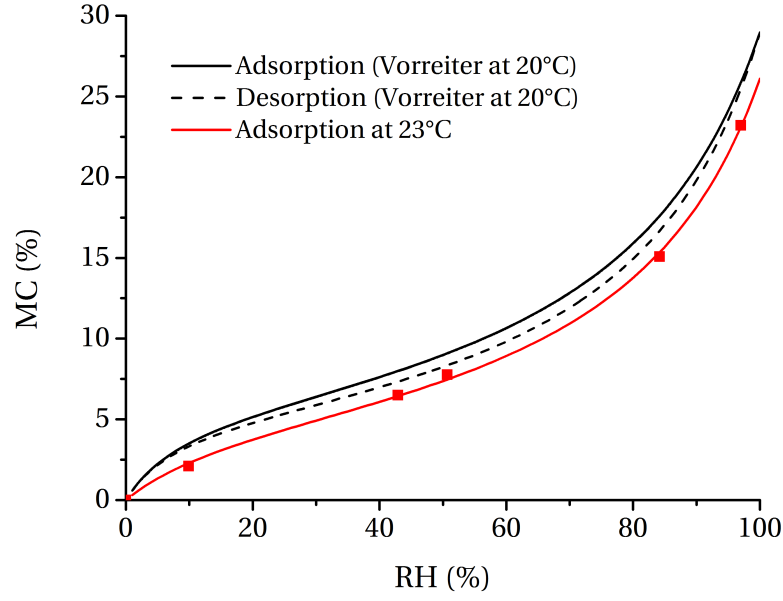


Figure 4.2: Sorption isotherm for beech wood. In black are the curves calculated based on data by Vorreiter [5]. The red curve is the adsorption calculated with experimental values. The parameters of relation 2.2 are expressed in table 4.2.

4.2 Moisture transport

After a predetermined diffusion time and removal of the welded specimen out of the climatic chamber, it is then sliced so that two MCs in each wood layer can be measured. These are graphically represented in figure 4.3 at various diffusion times.

Finite element model

A 2D symmetric heat transfer FE analysis is performed with a model constituted of three layers of wood of 15 mm thickness separated by a 0.15 mm thick layer with heat conductive properties. The thinner layers represent the welded joint.

In order to easily implement moisture diffusion in standard FE software, Gereke [30] suggests making an analogy between moisture and heat transport. Fourier's law for heat transfer (equation 4.1) can be compared with equation 2.5.

$$\frac{\partial T}{\partial t} = -\frac{k}{c_p \rho} \frac{\partial^2 T}{\partial x^2} \quad (4.1)$$

where T is the temperature, k the coefficient of heat transfer and c_p the specific heat. Therefore,

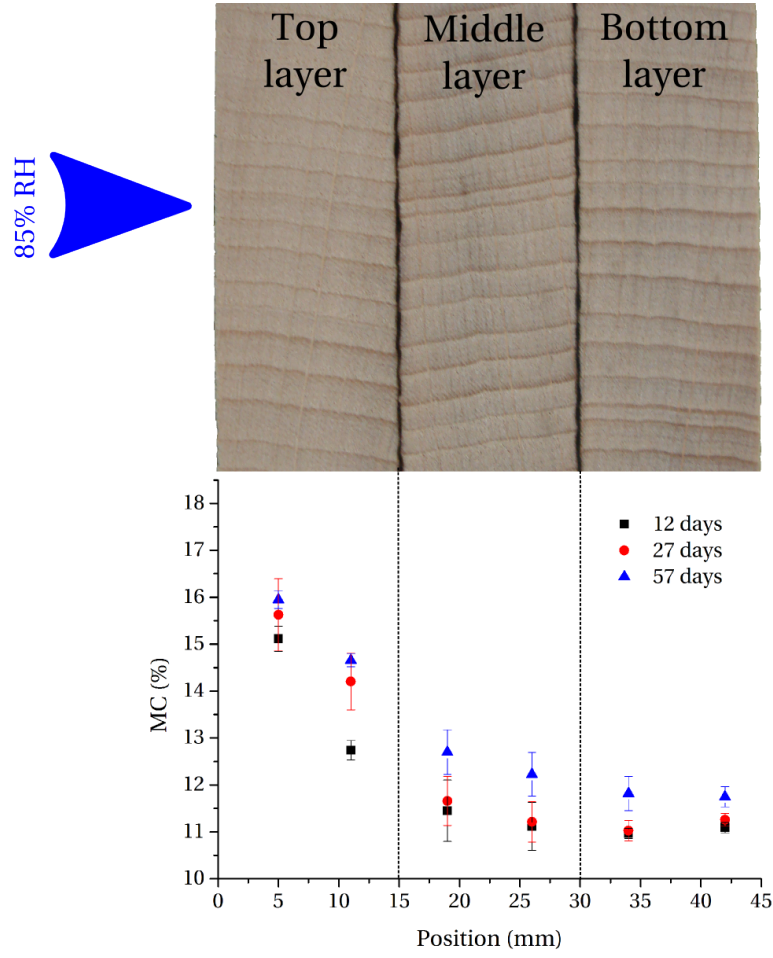


Figure 4.3: Experimental MCs measured as a function of the position in the specimen and the diffusion time.

moisture diffusion can be described with a heat diffusion model by identifying c with T and taking $D = k$ and $c_p \rho = 1$. The elements used are quadratic coupled temperature-displacement with reduced integration. The mesh in the wood part is refined in the vicinity of the joint, which is itself composed of 3 layers of elements. The effect of the external moisture is modeled by a surface film boundary condition expressed by equation 4.2 and applied to the top surface. The value of the sink MC u^0 is the EMC corresponding to the RH of the environment, i.e 17.5% in this case. h is a film coefficient set to unity.

$$-J = h(u - u^0) \quad (4.2)$$

By using the diffusion coefficient, which is dependent on the MC, and presented in table 2.1, in the FE model, one obtains the MC profiles that are shown in figure 4.4 together with the

experimental data. Although the profile after 12 days seems to be well predicted, at longer diffusion times the deviation becomes significant, more particularly in the middle layer.

To improve the prediction of the model, the parameter D_0 and d of equation 2.6 are identified to express the coefficient of diffusion of the joint. An inverse identification method is used that combines a MATLAB routine with a FE analysis. After solving the FE model presented in section 4.2, the MC values are extracted on a path running along the symmetry axis. Since the mesh is finer in the neighborhood of the joint, the values are interpolated at regular space intervals of 0.225 mm and an average value is calculated over each distance corresponding to the thickness of the experimental slices in which the MC was measured. An error vector is built, which is expressed by the difference of the FE model MCs with objective data (i.e. the corresponding experimental MC measured in each slice). The optimization process iteratively varies the parameters to be identified until the error vector is minimized, i.e. the difference between the numerical and the experimental MCs are the smallest. At the end of the identification process, the parameters of diffusion that best approximate the MC profile in the welded piece are discerned. A flowchart of the inverse identification process is presented in figure 4.5.

The initial diffusion parameters are those from the literature presented in table 2.1, for both the wood and the joint. In a first step, only the joint diffusion parameters are identified. The results show that the diffusion coefficient of the joint is one order of magnitude lower than that of the wood and therefore offer a resistance to moisture transport that is visible on the graph of figure 4.6(a) where the MC curves are no longer continuous but show a step at each joint position. In this way, the moisture levels of the middle layer are better captured by the model, but the values at 57 days are still slightly underestimated.

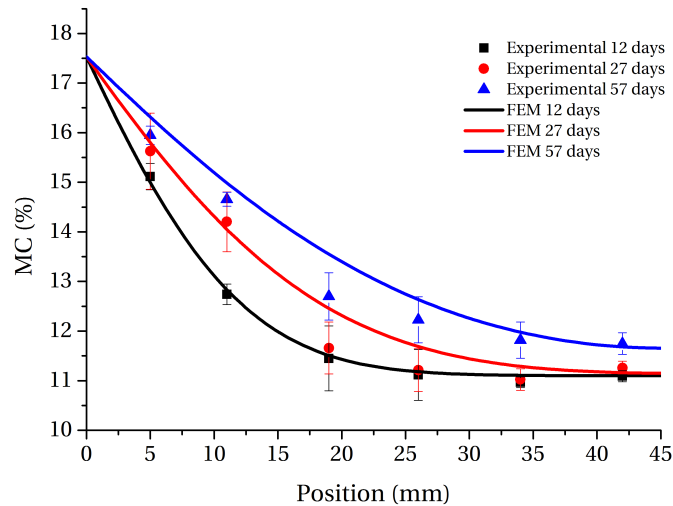


Figure 4.4: Comparison of the experimental values with numerical results. In this case, the same diffusion coefficient for wood and for the joint is used.

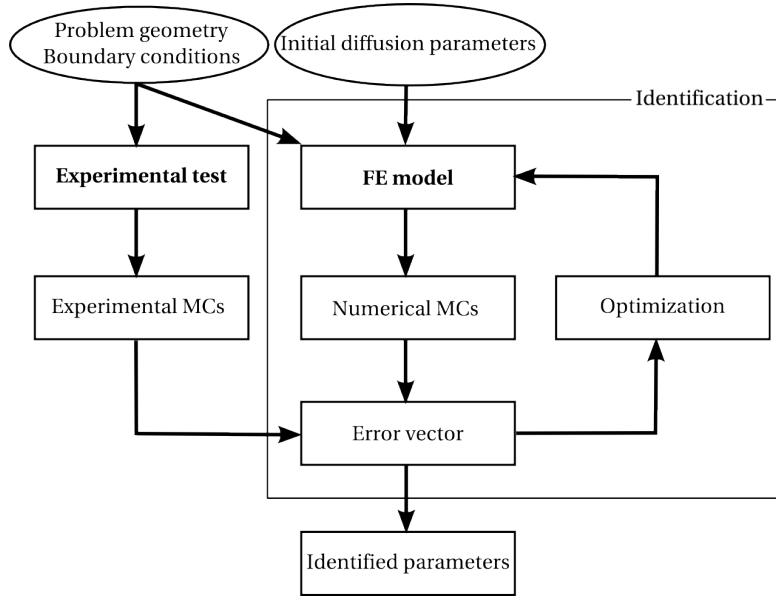


Figure 4.5: Flowchart of the identification process.

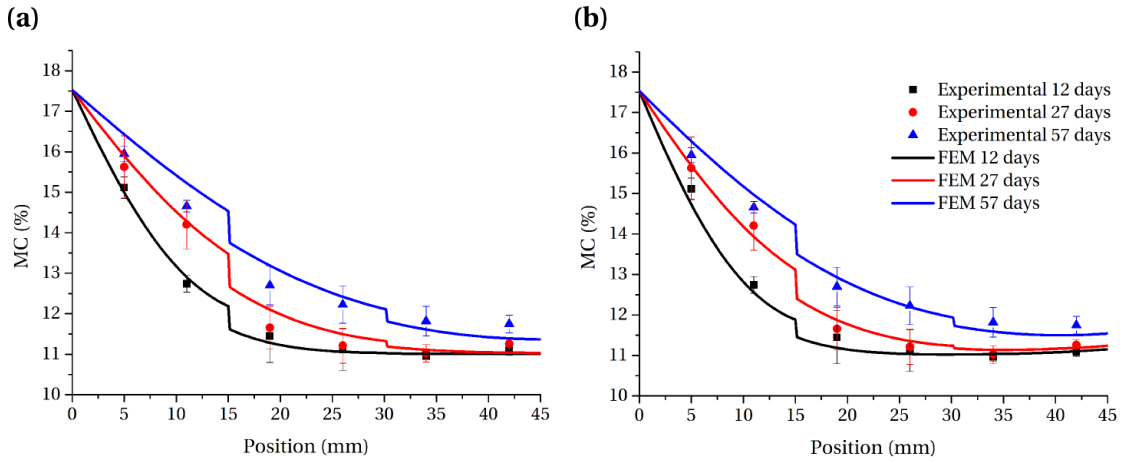


Figure 4.6: Moisture content profile within the pieces. The curves are the result of the identification of the coefficient of the joint and the dots are the experimental data. In (a) the coefficient of diffusion of the joint is identified while the other parameters are left constant. In (b) the diffusion coefficient of wood and film coefficient are identified with a constant coefficient of the joint.

The very last experimental data in the bottom layer seems to be above the initial MC and suggests that the aluminum foil is not totally impermeable and that a small amount of diffusion occurs also from the bottom surface. Since inverse identification is strongly dependent on the experimental conditions, it is possible that the coefficient identified by Olek et al. [25] for beech does not suit our experimental conditions. The natural variability of wood properties can also explain some differences. Therefore, a second identification process is carried out for the diffusion coefficient parameters of the wood. Furthermore, convection is allowed from the bottom layer, but with a high transfer resistance i.e, the film coefficient h expressed in equation 4.2 is set as a parameter to be identified.

The results of the FE modeling with the identified parameters are shown on figure 4.6(b) and present an acceptable prediction of the experimental values. Indeed, with a small amount of diffusion from the bottom surface ($h = 1.34 \cdot 10^{-7} \text{ mm s}^{-1}$) and a slightly lower coefficient of diffusion than the one identified by Olek et al. [25], the maximal relative error reaches 3.8%. The evolution of the diffusion coefficient with the MC is presented in figure 4.7. We see that the identification of the wood coefficient gives results very close to the value found in the work of Olek et al. [25] but the sensitivity to MC is slightly increased. The identification of the joint coefficient of diffusion leads to a value that is one order of magnitude lower than that of wood with the same behavior with MC increase, i.e. the coefficient decreases.

The diffusion coefficient usually reported in the literature for spruce [124, 28] has the opposite behavior by increasing MC, which is theoretically explained by Skaar [14] who present a general mechanism for diffusion of bound water with concentration as driving force. However, in the case of beech wood [25, 29, 28] and scots pine [27] decreasing coefficients with increasing

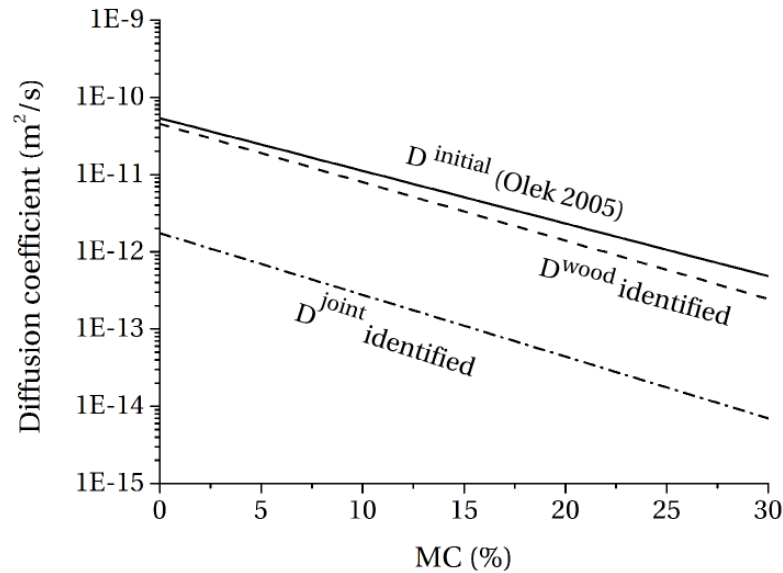


Figure 4.7: Evolution of the moisture diffusion coefficients with the MC below FSP.

MC have been identified by inverse methods. The underlying reasons are not yet totally clear, but the authors mentioned that the choice of the function describing the dependency of the coefficient with MC is of great importance. Therefore, an analysis based on a non-Fickian behavior might lead to other results [30]. It must be also noted that the various studies used different experimental conditions, leading to different boundary conditions that might affect the result of an inverse method identification. Even better accuracy could be achieved with additional tests on the wood alone and with better controlled experimental conditions, in order to have as few as possible parameters to identify at the same time. Nonetheless, this test demonstrates that the welded joint acts as a barrier for moisture diffusion, which leads to a high gradient of MC on either sides of the joint, possibly resulting in high damaging stress due to hygro-expansion. The reason for a lower diffusion coefficient of the joint is certainly due to the denser and less porous joining material than the wood, but also due to the wood cells surrounding the joining material subjected to a heat treatment during the welding and becoming subsequently less hygroscopic.

Parameter	Material	
	Wood	Joint
$D_0 \text{ (m}^2/\text{s)}$	$0.45243 \cdot 10^{-10}$	$0.017398 \cdot 10^{-10}$
d	-0.173941	-0.183988

Table 4.3: Identified diffusion parameters (see equation 2.6)

4.3 Summary

In this chapter, the hygro-mechanical properties of the wood were determined by measuring physical data at various EMCs. Most of them are already available in the literature and they are crucial for the modeling of wood hygro-mechanical behavior. Considering the high variability of the wood material and the simplicity of the measurements, it makes sense to ascertain these properties in order to have a correct characterization of the material that is used.

The moisture diffusion properties of the welded joint were not available and the inverse method used in this work enabled identifying suitable parameters to express moisture diffusion through the joint. The results show that the joint acts as a barrier hindering the moisture transport through a welded piece, because its diffusion coefficient is about one order of magnitude lower than that of the wood. In addition to having determined the diffusion properties of the joint, one saw that this situation led to a high MC gradient across the joint with potential issues due to hygro-expansion strains. The results presented in this chapter complete the knowledge on the behavior of welded wood joints and will assist modeling the MC field of a welded wood piece in transient conditions and its subsequent stress states due to swelling and shrinkage.

5 Mode I crack propagation

The failure of welded wood joints as a consequence of their contact with water and their decrease in strength is reported in the literature. It is most likely that, like other mechanical properties of wood, the fracture characteristics of the welded joint are affected by moisture. The goal of this chapter is to investigate and understand the effects of moisture on the pure mode I fracture characteristics of the welded joint and to provide information to model the crack propagation in mode I.

For this purpose, DCB specimens are produced and brought to various EMCs. DCB tests are carried out and the ERR in mode I is computed using an experimental compliance calibration data reduction method. Besides the fracture tests, the maximal tensile strength of the joint is evaluated with a uniaxial tensile test performed using specimens at the same EMCs than those of the DCB. A FE model is constructed with cohesive elements in order to model crack propagation and the simulated behaviors at various MCs are compared with the experimental ones.

5.1 Experimental tests

5.1.1 DCB test and energy release rate

Typical load-displacement curves of the DCB specimens are shown in figure 5.1 and the scatter of the experimental curves is illustrated with a grey error zone. The dashed lines are the results of FE modeling and are commented on section 5.2. The limits of the error zones are calculated by adding or subtracting the standard deviation to an average load value calculated out of four experimental curves at each displacement. The increase of moisture has mainly two effects. Firstly, the maximal load is smaller at the highest MC (22%) and secondly, post peak behaviors are also different depending on the MC level. Although crack propagation is stable, the dry specimens (6%) show intervals of sudden crack length increment. Such propagation features seldom occur in the specimen with 12% MC and are totally absent in samples with 16% and 22% MC.

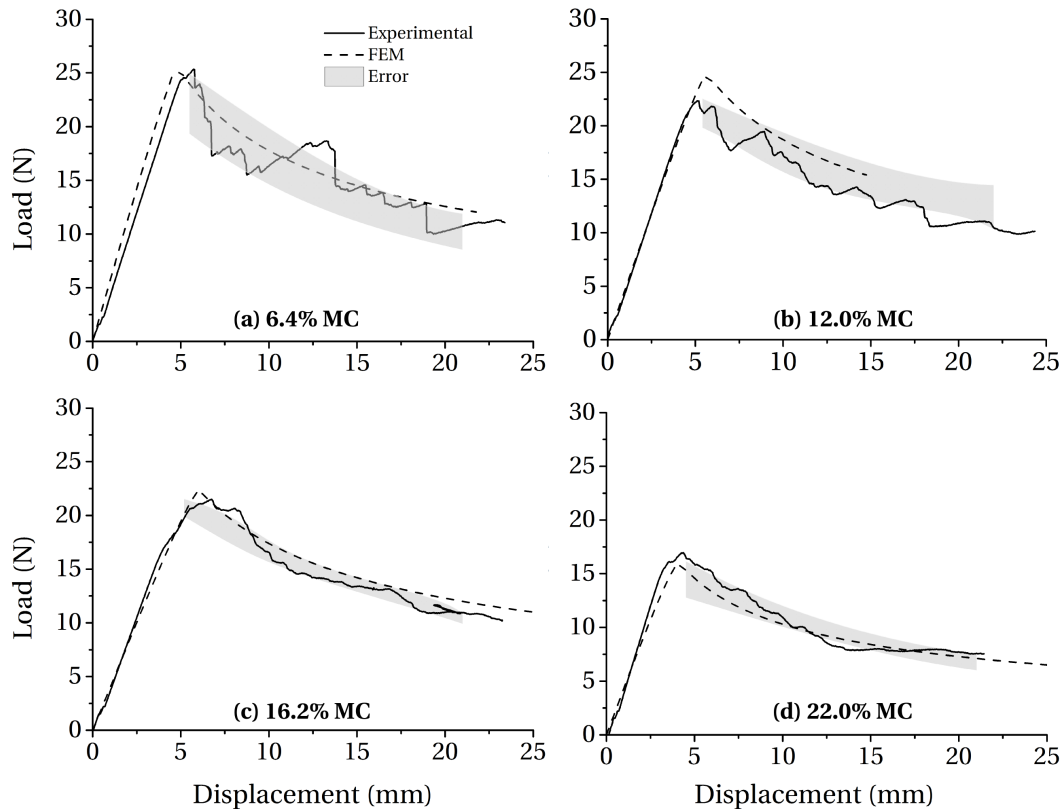


Figure 5.1: Comparison of typical load-displacement experimental curves (straight lines) with results obtained by FEM (dashed line). The relative error, represented by the gray area, is calculated according to the standard deviation of the experimental data (see text for details).

A scheme of the two parts of a specimen after fracture at 22% MC is presented in Figure 5.2 and the SEM photograph of the lower part of a fractured specimen. The crack propagates at the interface between wood and the joining material, with frequent crossing over reaching the opposite interface. The cracked specimens at the other MC's show a similar pattern, except for the pulled out fibers that are not present.

Photographs of the fracture surfaces for the four levels of MC are displayed in Figure 5.3, which do not show an effect 16% MC. However, at 22% MC, long wood fibers are visible at the surface of the joining material. In dry conditions, these fibers are embedded in the matrix and break during fracture and only short fiber fragments are elevated above the surface. At higher MC, the fibers are pulled out from the matrix, as if the adhesion between the fibers and the matrix material had deteriorated due to the moisture.

Energy release rate is calculated for each point corresponding to a crack propagation onset. The measured load P and the applied displacement enable calculating the compliance corresponding to the crack length a measured during testing. Values of compliance in terms of a

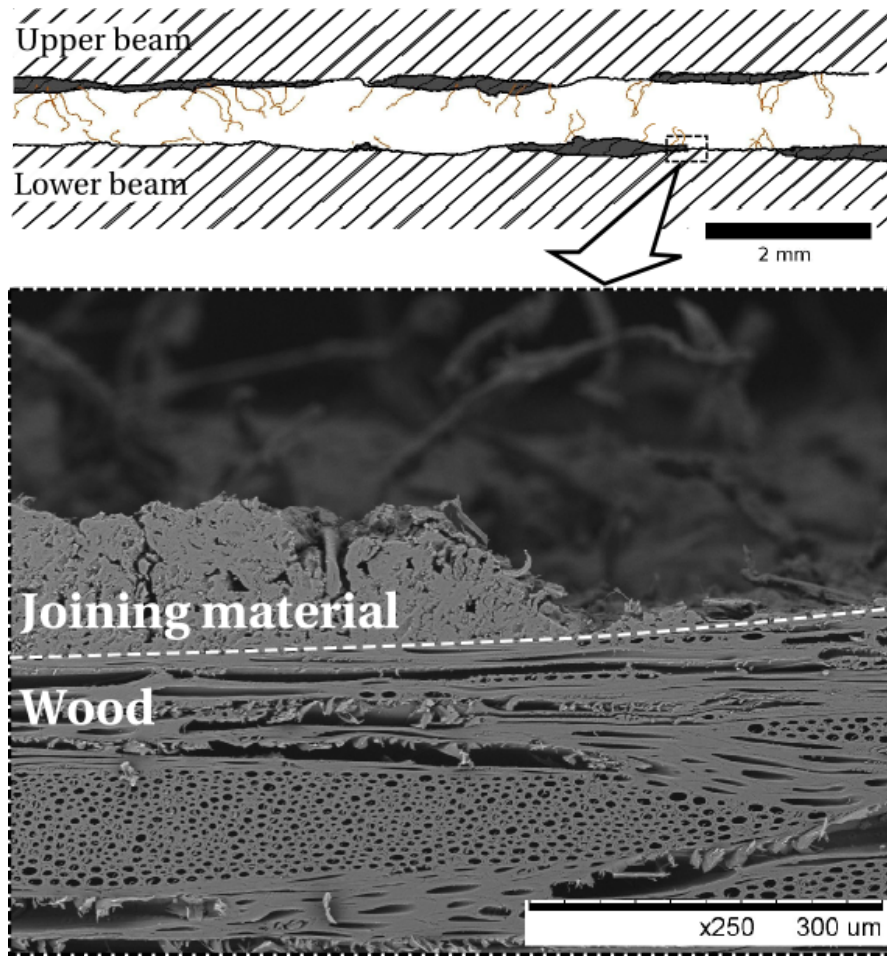


Figure 5.2: At the top is a schematic representation of the crack path on a moist specimen (22% MC) after separation of the joint. The pulled out fibers are the brown lines coming out of the joining material in black. The photograph at the bottom is a magnification showing the detail. The SEM picture shows the transition of the crack path that crosses the joint material from one interface to the other.

can therefore be fitted with a power equation for subsequent processing:

$$C(a) = C_1 a^m \quad (5.1)$$

Once C_1 and m are determined, the derivative is calculated and inserted in equation 2.21 to compute G_{Ic} . The points presented on Figure 5.4 are average values of G_{Ic} calculated in the post peak region and the error bars are obtained from the standard deviation of the data. Although the results are scattered, R-curve behavior is not seen at any level of MC tested, which shows that the FPZ is negligible. At low levels of MC, the G_{Ic} values are quite similar, however

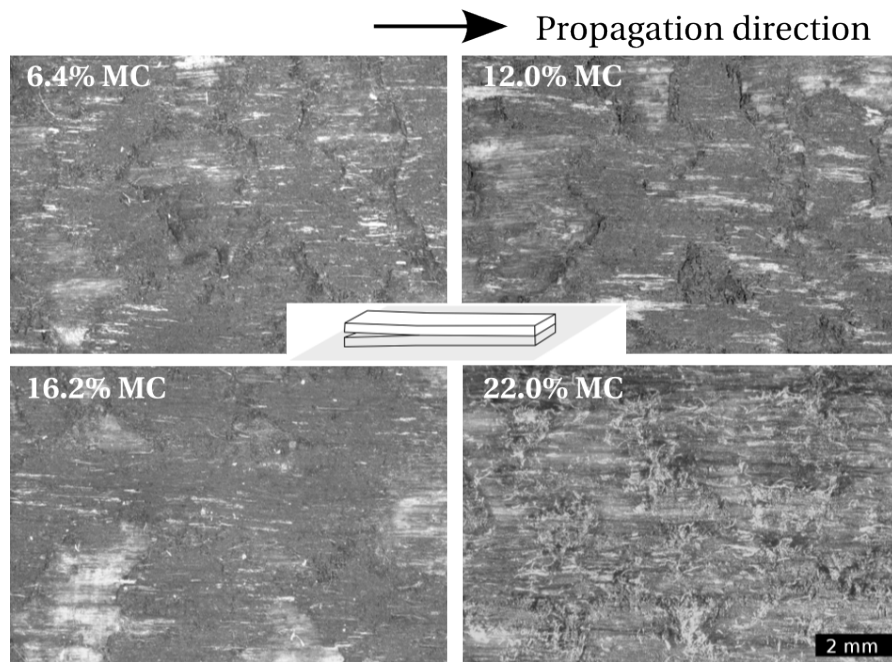


Figure 5.3: Optical light microscopy photograph of the fracture planes for all four different MCs. The fracture surface exhibits islands and valleys formed by the welded material. The opposite surface has the negative print of these features. At this scale, only the moist specimens exhibit a fleecy surface. This is due to long fibers coming out of the joining material.

a strong decrease at high MC can be noticed. The results show a similar behavior to those of Kretschmann and Green [45], who investigated the K_{Ic} of pine, and the change of fracture properties can be well expressed as a function of MC by a second order polynomial expression. Based on this, a maximum of G_{Ic} should be at ca. 11% MC. Although the trends for fracture properties as a function of MC are similar for wood and the welded joint, the magnitude is more elevated for the joint. Indeed, while the reduction of fracture toughness measured by Kretschmann and Green [45] reached 39%, the ERR of the welded joint is reduced by 52%.

In order to identify the source of the difference of ERR between dry and moist specimens, surface profiles are performed on the cracked specimens with the lowest (6%) and highest (22%) MC. The device used for the roughness profile is a non-contact optical profilometer from Breitmeier Messtechnik and the fractal dimension is determined by the box counting method with the ImageJ plugin FracLac 2.5. The roughness and the fractal dimension, which are shown in table 5.1, do not reveal significant differences, thus suggesting that the fracture mechanisms are not fundamentally different. However, the matter is complex and, as reviewed by Charkaluk et al. [125], a different relationship, or no correlation, were found between the fractal geometry and the fracture toughness in various works. For a deeper analysis, the concept of anomalous scaling successfully used by Morel et al. [66] for wood fracture should be used to take into account the anisotropy of crack development in quasi-brittle material.

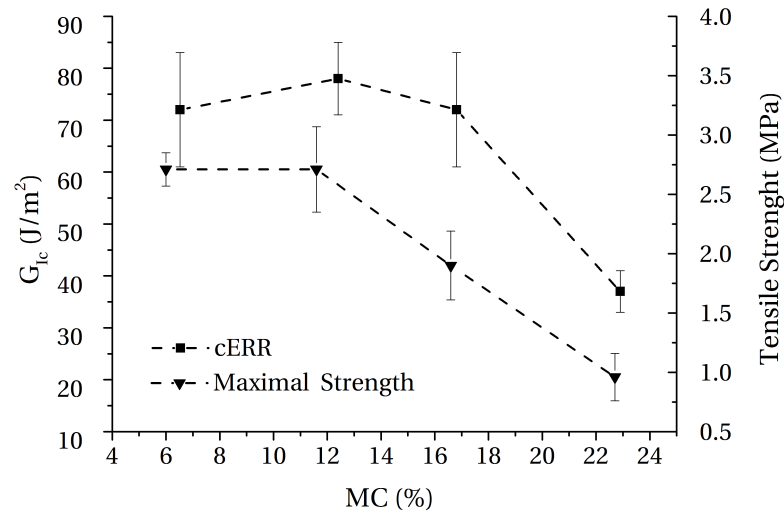


Figure 5.4: Evolution of the critical energy release rate (G_{Ic}) and the maximal tensile strength of the welded joint in terms of the corresponding MC.

However, in this case, and as experimentally demonstrated below, the decrease of fracture properties is mostly due to the change of strength of the joining material. The sensitivity of the joining material toward water is also highlighted by Placencia Peña et al. [126], who showed that the joining material's solubility in water is much higher than the unaffected wood. One can therefore say that physico-chemical changes occurring during the welding process leads to a very moisture sensitive material, which in turn affects the strength and fracture properties.

Data	Values at various MC	
	6.4%	22.0%
Roughness R_a (μm)	15 ± 2	20 ± 3
Weaviness W_t (μm)	126 ± 30	123 ± 25
Fractal dimension D	1.32 ± 0.04	1.36 ± 0.02

Table 5.1: Roughness and fractal data of the fractured surface.

According to the results of Majano-Majano et al. [43], the fracture characteristics of a welded wood joint determined here are quite close to those of thermally treated beech. Although the welded joint is composed of totally new material, this indicates that the welding of wood probably has the same effect on the properties as standard heat treatments applied to wood. In comparison with untreated beech, welded joint, independent of the MC, requires about 3 to 4 times less energy for the crack to propagate, i.e. the joint is the weakest part in a welded wood assembly.

5.1.2 tensile test and maximal strength

The load-displacement curves obtained from the tensile tests show waviness due to machine alignments when working in displacement control. However, as fracture always occurs in the joints, the maximal loads measured make it possible to calculate their maximal tensile strength that are presented in figure 5.4.

A few attempts on new specimens and with load control give much smoother curves and enable treating the data with the DIC (example of stress-strain curves at each MC is presented in figure 5.5). Interestingly, but maybe not statistically significant, only the high MC specimens demonstrate discernible damage initiation prior to failure, which is characterized by a relatively flat curve. Nonetheless, in all cases, the failure occurs in a brittle manner. The strain calculated results from the displacement are measured along lines placed on each side of the images, hence playing the role of an optical extensometer (see the "total" extensometer in figure 5.6(a)).

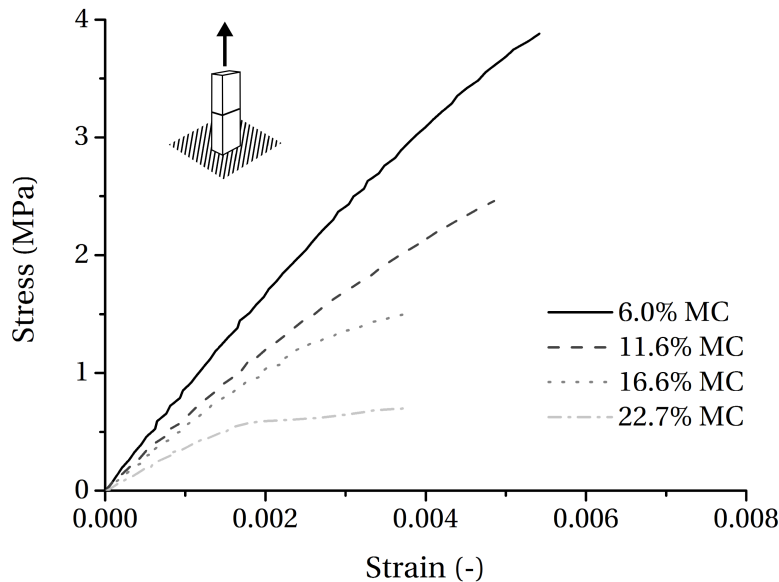


Figure 5.5: Representative stress-strain curves obtained during the tensile test at different MCs.

DIC enables measuring the displacement anywhere on the pictures, and therefore computes the strain for any chosen parts. The results of the attempts to measure the strain of the joining material and the wood are presented in figure 5.6(b) for a specimen at 11.6% MC. Due to the small thickness of the joint and its wavy shape, it is difficult to obtain the strain for this material only and with enough precision. In contrast, the slope of the linear curve for the wood part results in an elastic modulus of 1048 MPa. This is close to the theoretical value computed for a wood at 11.6% MC with equation 2.10, which gives a value of 1116 MPa for the tangential direction. This demonstrates that the method is valid but needs some improvement in order

to correctly work with the joint. A higher magnification may permit focusing on the joining material part, and therefore allowing optimal selection of the location for the displacement's measurement.

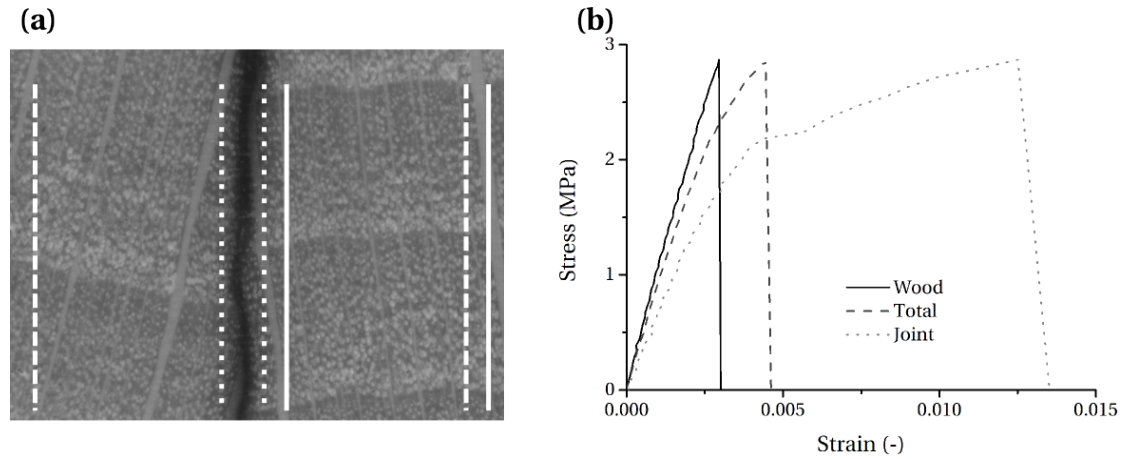


Figure 5.6: (a) Location of the lines along which the displacements are measured to compute the strain. Straight lines serve as an optical extensometer for the wood part, dotted lines for the joint and dashed lines are the strain over the total width of the picture. (b) Strain-stress curves corresponding to the different extensometer presented in (a).

Similarly to the fractured surface of the DCB specimen, fibers are clearly visible in the broken interfaces of the moist specimens (Figure 5.7). The maximal strength values plotted in Figure 5.4 in terms of MC, illustrate that the maximal strength strongly decreases with increasing MC above 12%. Apparently the moisture also decreases the stiffness, as well as the strain at failure (Figure 5.5).

The equilibrium MC calculated for the tensile specimens are slightly different than those of the DCB specimens. This small deviation can be due to the slightly different environmental conditions at the time of weighing the reference specimens. Supposedly, the influence of this has a negligible effect on the elastic constants. As a matter of fact, the largest MC difference encountered (0.7% MC) induces a change of 1.3% on the value of the longitudinal modulus. Therefore, the MCs corresponding to the DCB specimens are used in the calculations.

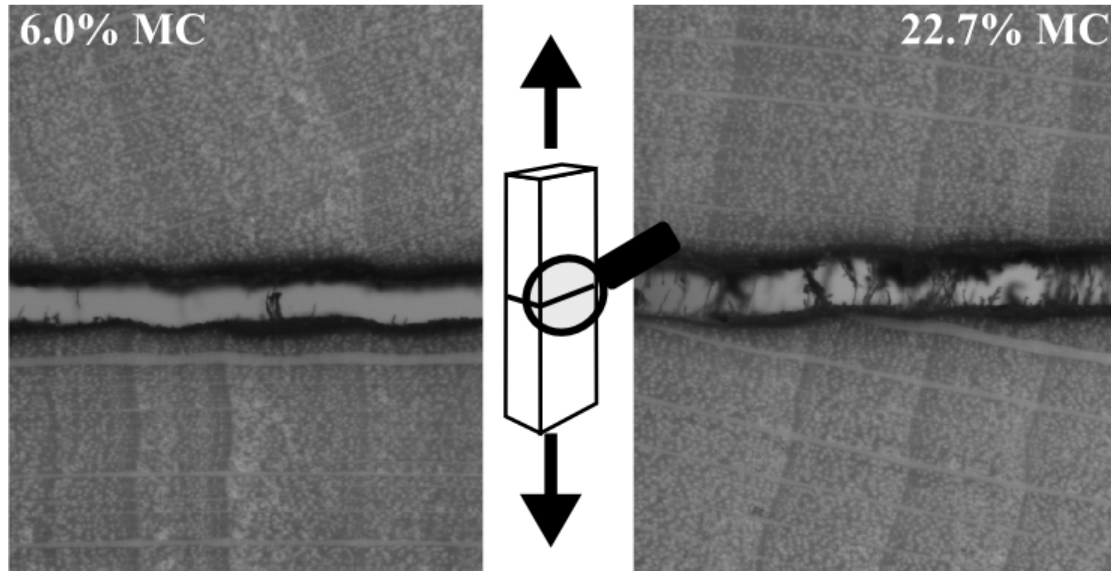


Figure 5.7: Close images of the fractured joint (black part in the middle) after failure of the tensile specimen. Fibres entanglement between the two broken parts differentiate the dry (left) and moist (right) specimens.

5.2 Finite elements modeling

A two dimensional FE model to simulate crack propagation in the DCB specimen is constructed. The wood beams are represented with quadrilateral plane strain elements and the elastic properties for beech. The sketch of the model is shown in figure 5.8. To simulate the loading blocks, reference points are placed 5 mm below (A) and above the specimen surface at B and at a distance of 5 mm from the end of the beams. The reference points are linked to a 10 mm long node set on the surface of the beams with a beam multi-point constraint (MPC). A has only a rotational degree of freedom and the vertical displacement is imposed on B.

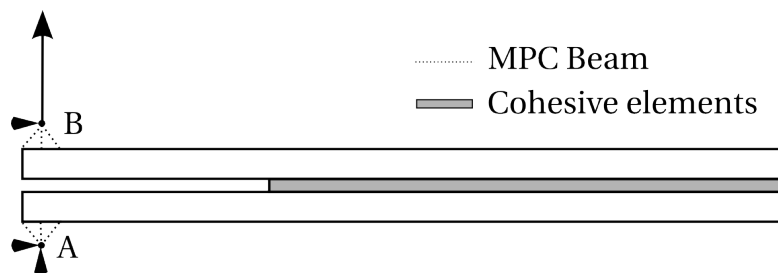


Figure 5.8: Schematic of the DCB FE model (see text for detail).

During this work, the wood properties are considered as linear elastic. In the Abaqus software, engineering constants that are dependent on the MC are used. A table is constructed according to the reference elastic properties presented in table 2.2 for beech and the relations 2.10

Properties	Values at various MC			
	6.4%	12.0%	16.2%	22.0%
t_n^0 (MPa)	2.7	2.7	1.9	1.0
G_{Ic} (J/m ²)	72	78	72	37

Table 5.2: Experimental data of the tensile and DCB test.

and 2.11. A predefined field is included to specify the appropriate state of MC and therefore select the corresponding elastic properties. These considerations apply to all models throughout this work and the specificities of each model are presented later.

The maximal strength and critical energy release rates are experimentally measured and presented in table 5.2 and inserted in the cohesive law presented in figure 3.15. Figure 5.1 shows the load-displacement curves obtained experimentally and those obtained by FEM (dashed lines). Although the scattering of the experimental curve can reach 15%, the model describes the observed experimental maximal loads and post-peak behavior quite well. Coureau et al. [127] and Morel et al. [68] demonstrated that the presence of fiber bridging during wood fracture requires the use of a bilinear damage law. In the present study, however, a simple linear damage law is sufficient to model the crack propagation during a DCB test. This fact shows that the fiber bridging effect does not have to be considered, although optical observations seem to indicate the presence of fibers on the fractured surfaces of the wet specimens (Figure 5.3). The decrease of the initial slope on the simulation curves with increasing MC is due to the elastic moduli of wood. The different moduli values decrease with MC according to equations 2.10 and 2.11, therefore, the slope is steeper in the case of elastic loading under dry conditions. The differences in the slopes of the simulated curves and the experimental ones can be explained by the natural variation of the longitudinal modulus of the wood.

5.3 Summary

In this chapter, it was demonstrated that it is possible to determine the critical energy release rate of the joints at different MC with a DCB test. The influence of MC on the fracture properties is obvious, because the specimens with high MC (22%) have G_{Ic} values about half the value of those with low and intermediate MC at 6 – 16%. The optical observations revealed MC dependent differences and support the idea that moisture has a strong influence. The fracture surface of the high MC specimens exhibit pulled-out fibers, which have shown to have limited toughening effect. The tensile tests highlighted the declining tendency of the joining material properties with increasing MC. ERR and maximal strength values show a similar trend at high MC. Accordingly, the loss of fracture toughness is mainly due to the poor performance of the joining material. A FE model representing the DCB test configuration is built based on the experimental data of the DCB and tensile tests. The results show that a linear cohesive law with the parameters determined in this chapter can accurately model the behavior of welded

Chapter 5. Mode I crack propagation

wood joints under the MC conditions examined in this work. Most of the results presented in this chapter appear in Rheme et al. [128].

6 Mode II crack propagation

Following mode I, this chapter investigates the effects of MC on the mode II fracture characteristics. The approach is similar to that of the previous chapter, but here the fracture propagation is investigated in pure mode II with a 4-ENF test. In order to determine the parameters of a cohesive law, shear strength of the joining material is evaluated at various MCs with a torsion test. Crack propagation is modeled with cohesive elements and compared with the experimental data. Finally, some considerations about the effect of friction occurring in the experimental device are presented.

6.1 Experimental tests

6.1.1 4-ENF test and energy release rate

In the typical load-displacement curves obtained during the 4-ENF test for different MCs (figure 6.1), the experimental error is represented by a grey area, which is calculated according to the standard deviation of the experimental curves. The curves can be divided into three zones. At the beginning, there is a part exhibiting elastic behavior and later, at some critical load, the crack propagation initiates and advances. This step is characterized by an evolution at a nearly constant load. Once the crack tip reaches the location of the second support, the propagation is stopped, and the load starts to increase again.

Photographs presented in figure 6.2(a) illustrate the crack propagation. The shear effect is visible by the relative movement of the vertical marking after the crack growth. The crack propagates in the interface between the joint material and the wood with frequent crossing of the welded joint to reach the other interface (figure 6.2(b)). In all cases, the crack advances within the bond without affecting the wood. Fracture surfaces look very similar to those observed in mode I propagation (chapter 5). In the present case, however, the presence of fibers on the split bond's surfaces of moist specimens (22% MC) is much less evident than in the case of mode I fractions. It is likely that the translational relative movement of the two surfaces smoothed the pulled-out fibers, which are pressed again into the surface.

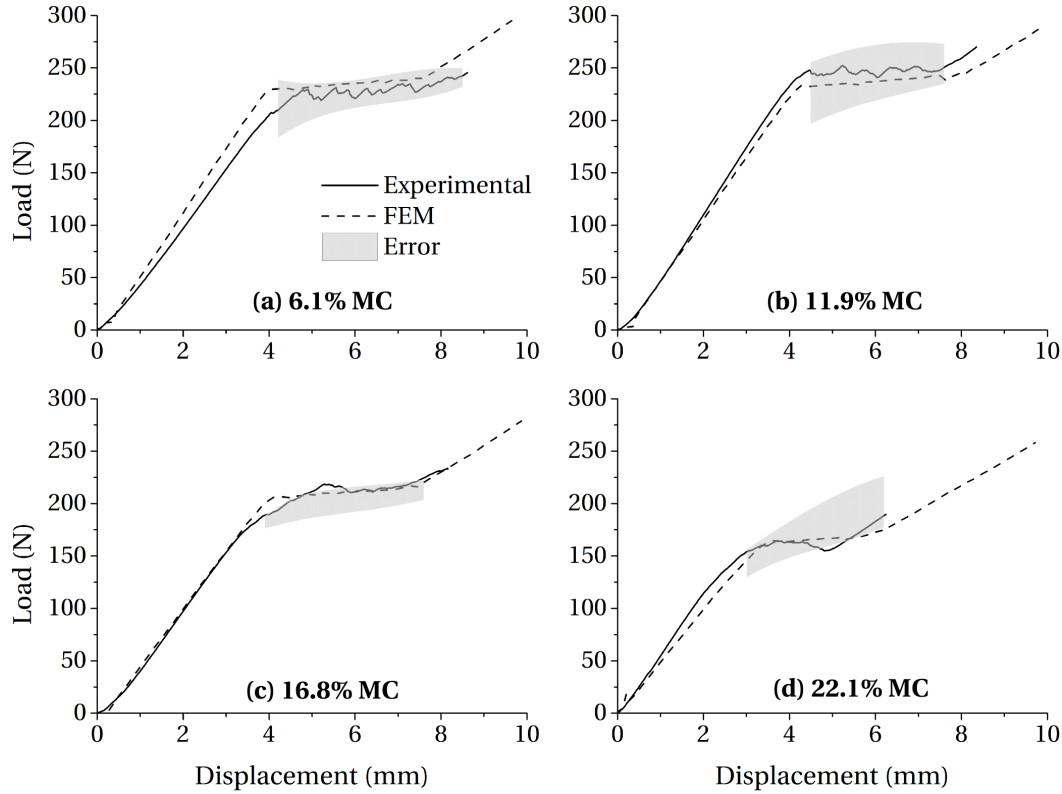


Figure 6.1: Examples of load displacement curves obtained with the 4-ENF test at various MCs

Energy release rate calculation G_{IIc} can be expressed by the same relation as that for G_{Ic} (see equation 2.21). In the case of the bending test with the ENF specimen, the expression of the compliance $C(a)$ in terms of the crack length a can be fitted with a linear expression $C(a) = C1 a + C2$. Therefore, the derivative of this last expression with respect to a gives the value of $C1$, which is needed to solve equation 2.21.

Despite an initial lower value of G_{IIc} , calculated at the loss of linearity of the initial part of the load-displacement curve, all further values are nearly constant, within the experimental error, and lack any discernible R-curve behavior. Therefore, as soon as the load plateau is reached, the values of G_{IIc} are taken into account for the calculation of the average. These values of G_{IIc} and their variation with MC are presented in figure 6.3 and show a similar trend to that in mode I.

A small difference of the average values can be noticed between specimens with 6 - 12% MC. However, at MCs higher than 12%, the critical ERR seems to decrease. The values of G_{IIc} are twice as high as those of G_{Ic} . Comparison with solid wood is difficult as no value of G_{IIc} for beech has been found in the literature. In mode II fracture of spruce, Yoshihara [71] introduced grooves on the lateral surfaces to achieve rectilinear crack growth, in order to lower the load necessary for crack propagation and therefore to avoid bending failure of the specimen before

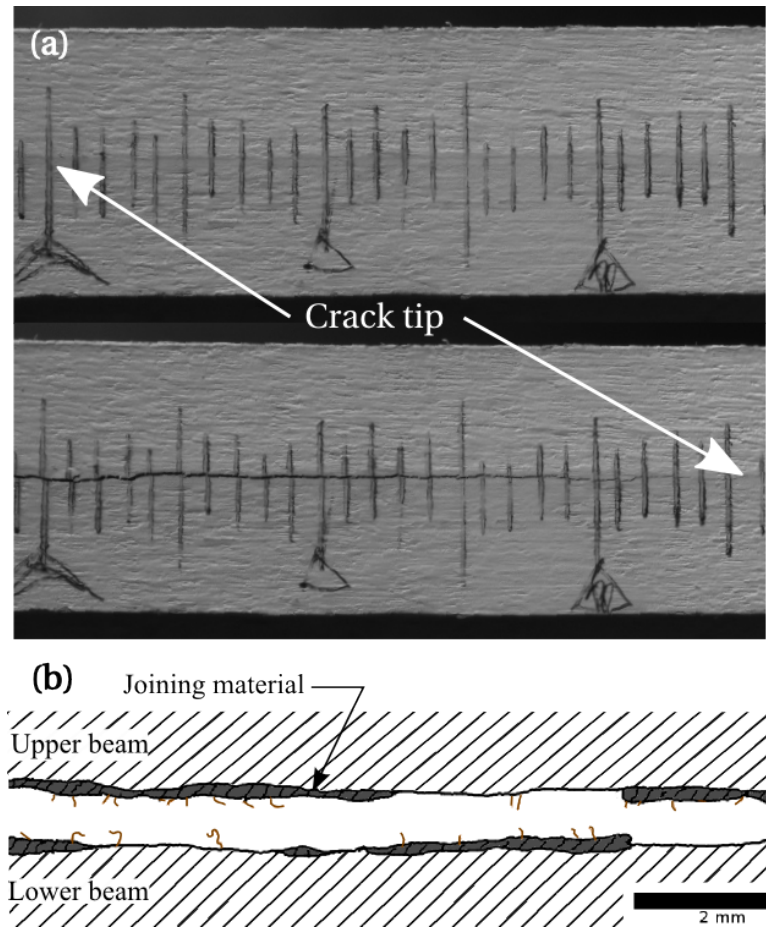


Figure 6.2: (a) Photograph at the beginning of the test (top) and after 25 mm of crack propagation (bottom). The distance between each vertical line is 1 mm. (b) Sketch of the lateral surface of the ENF specimen after separation, which is based on optical microscopy observations. The dark parts represent the joining material and the wood beam appears striped. Fibers are indicated by the thin lines.

crack propagation. In the case of the welded joints, no reduction of the section is necessary for crack propagation in mode II, indicating that the value of G_{IIc} of the joint is probably lower than that of solid wood. For comparison, a few tests are performed with solid beech wood specimens taken from the same plank, from which the welded specimens were produced. Grooves are also necessary to avoid bending failure. Unfortunately, such features prevent accurately observing the crack length and therefore it is only possible to calculate a G_{IIc} at initiation. At 12% MC, this value is 550 Jm^{-2} , which is comparable with spruce [71] and about four times higher than the G_{IIc} of the welded joint.

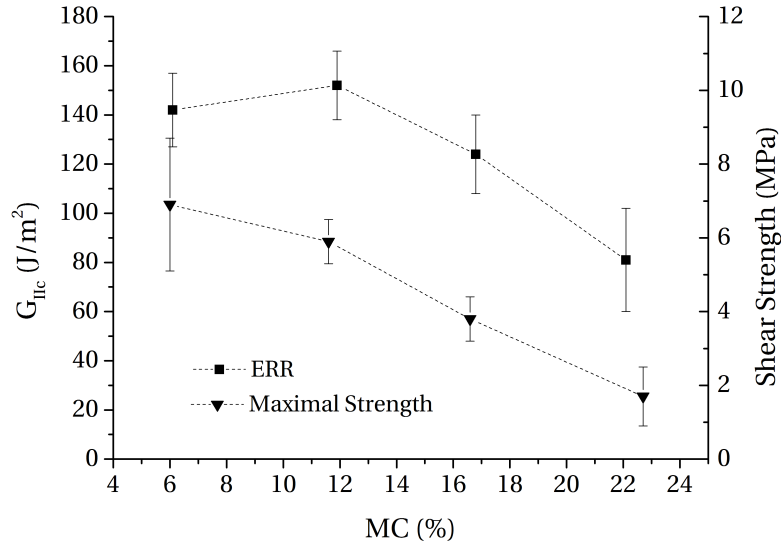


Figure 6.3: Evolution of the critical energy release rate (G_{IIc}) and the maximal shear strength of the welded joint as a function of the MC of each group of specimens.

6.1.2 Torsion test and maximal strength

Typical curves obtained from the torsion tests are presented in figure 6.4(a) for all four different MC. Moisture led to the decrease in both the angle and torque at failure. The calculation of the maximal shear strength is approximated with equation 6.1.

$$\tau_{max} = \frac{16T}{\pi HB^2} \quad (6.1)$$

T is the torque at failure, H and B are the long and short axis lengths of the elliptical section. The maximal shear strengths are plotted in figure 6.3 as a function of MC. The error for the dry specimen is relatively large, but a constant decrease of the average values with increasing MC is clearly visible. Three main types of torsion failure are observable. As shown in figure 6.4(b), failure can occur totally in the joint (most of the time) or partially in the joint and in the wood. This is particularly true for dry specimens (6% and 12% MC) with a calculated maximal strength in the order of magnitude of the maximal shear strength of beech [5, 129]. In this work, only the specimens with a total failure in the joint are considered for calculating the average of the shear strength of the joint in equation 6.1.

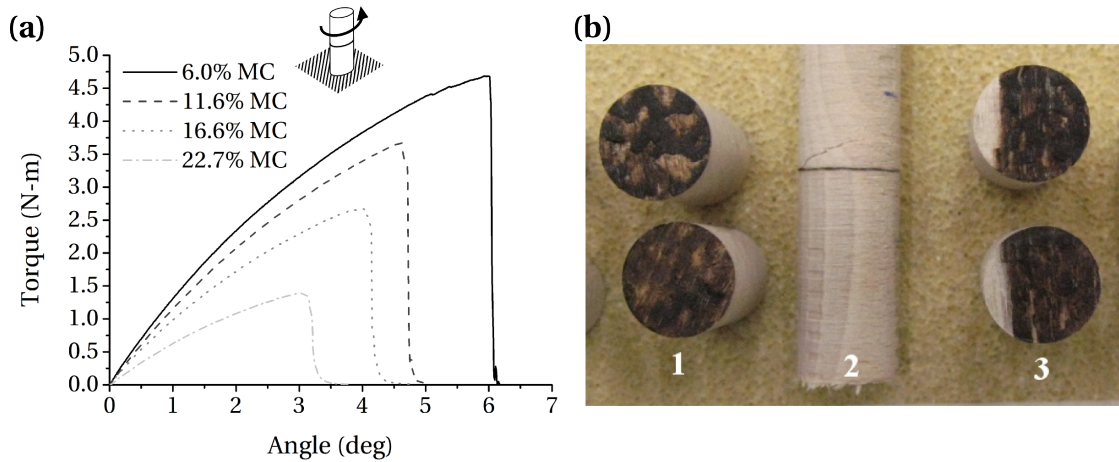


Figure 6.4: (a) Torque related to the angle of rotation during the torsion test. One representative curve for each MC is presented. (b) Torsion specimens after fracture. Three types of fracture occurred. (1) Fully in the welded joint, (2) partially in the joint and mainly in wood, and (3) partially in wood and mainly in the joint.

6.2 Finite elements modeling

The problem is considered to be two dimensional and plane strain and the wood beams are represented with quadratic quadrilateral elements. The glued metallic wedge inserted in the left hand support is represented by a 10 mm long node set at the bottom surface of the lower beam. This set is constrained with a MPC at its middle point (A) that only has a rotational degree of freedom. The other supports are modeled by disk sectors filled with quadratic triangle elements. Beam MPCs link the surfaces of the sectors with their centers (B, C and D). The displacement is imposed on a reference point (E) that is linked to the two upper supports centers by a beam MPC.

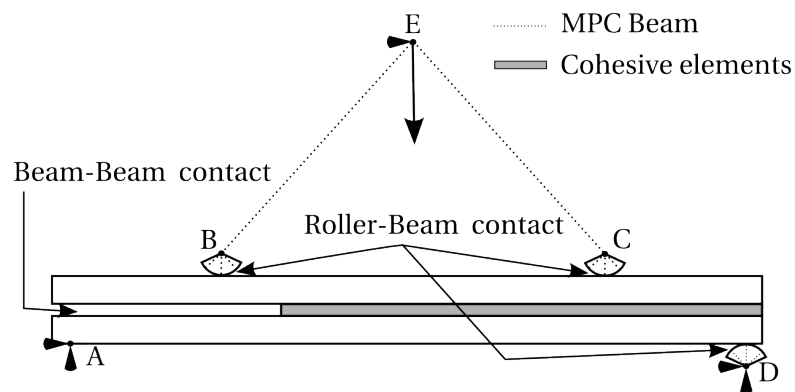


Figure 6.5: Schematic of the FE model (see text for detail)

Frictionless contacts in the tangential direction and hard contact in the normal direction is

Chapter 6. Mode II crack propagation

set between the supports and the beams (roller-beam contact), and between the two internal surfaces of the beam (beam-beam contact). In this way, interpenetration of the different material domains is avoided while simulating a frictionless process. Calculation with penalty tangential behavior and a coefficient of friction $\mu = 0.4$ (equivalent to wood to wood and wood to steel friction [130]) is performed.

Supports B, C and D are composed of steel with elastic mechanical properties (i.e., $E = 210$ GPa, $\rho = 7800$ kg m⁻³, $\nu = 0.3$). The high stiffness of the cohesive elements renders the calculations quite unstable and thus explicit formulation is needed to enable an unconditionally stable calculation. The wave propagation solution induces a jagged load-displacement curve in the simulation. The properties of the cohesive elements are the results of the experimental test and are presented in table 6.1.

Properties	Values at various MC			
	6.1%	11.9%	16.8%	22.1%
t_s^0 or t_t^0 (MPa)	6.9	5.9	3.8	1.7
G_{IIc} (J/m ²)	142	152	124	81

Table 6.1: Experimental results of the torsion and 4-ENF test

The curves shown in figure 6.1 (dashed lines) are smoothed with a moving average over 7 points. Interestingly, the numerical curves fall within the range of the experimental data, if the experimental variability are taken into consideration. The slope of the initial part of the simulated curves, which corresponds to the elastic response of the wood beams, gradually increases with decreasing MC. This clear effect is due to the modulus evolution caused by MC. Note that the slopes of the experimental curves for a given MC show larger variations due to natural variability of the wood.

The presented model is sufficiently representative of the reality and seems to be suitable to investigate the effects of friction on the test's results. Sources of friction during the test are located either between the two wood beams, i.e. on the crack faces, or between the supports and the specimen. In the simulation reported herein, the coefficient of friction is set to 0.4 in both cases, which correspond to either wood-wood or steel-wood friction. Figure 6.6 shows the effect of friction on the numerical curves, which are compared with the experimental curve of a specimen at 12% MC. The frictionless and beam friction curves are slightly different, but still in the range of the variation of the experimental curve. On the other hand, the friction of the supports on the specimen has quite important effects on the load-displacement curve: the initial slope is steeper and the maximal load is higher. Such a curve would not allow computing a correct G_{IIc} . The setup in this study was effective in eliminating large parts of the friction.

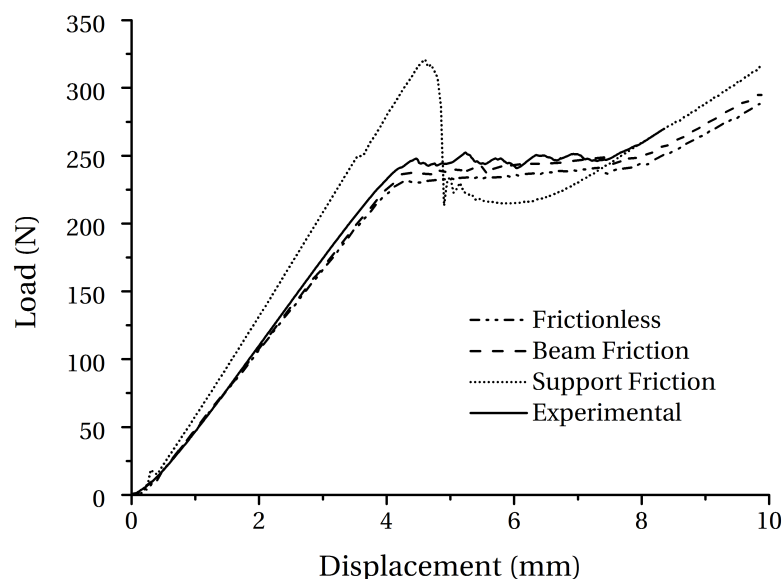


Figure 6.6: Effect of friction on the load-displacement response according to the FE modeling. Friction between the support and the specimen has much more influence than friction between the beams of the specimen. “Beam Friction” indicates the friction between the two wood beams. “Support Friction” refers to friction between the supports and the specimen. In both cases, the coefficient of friction is assumed to be $\mu = 0.4$.

6.3 Summary

The 4-points bending of ENF specimens was suitable for the study of mode II fracture of welded joints and stable crack propagation was observed. However, the influence of friction must be reduced to a minimum. Otherwise, the friction between the loading support and the specimen may induce important artifacts on the load displacement data measured. The critical ERR and the maximal shear strength were measured at different MCs, and these properties clearly showed decreasing tendency with increasing MC. A numerical study showed that the cohesive elements with a linear damage law were sufficient to model the welded joint. Like mode I, mode II fracture induced crack propagation in the joining material and confined between the wood interfaces. Unlike the conventional glues, the joining material does not penetrate the wood; thus, the adhesion is relatively weak in the case of welded joints. Wood cells and the joining material are dissimilar and the external loads easily weakened the assembly. It is highlighted in a quantitative manner that the welded joint is very sensitive to moisture. The studies presented in this chapter are the topic of a recent publication [131].

7 Crack initiation and mode mixity

In service life, the simultaneous application of tension and shear loads leads to a mixed mode state at the crack front. Moreover, in the case of wood, mode mixity is also induced by the anisotropic properties of the material and is therefore more relevant for real applications. Furthermore, wood engineered products are often produced by the bonding of different layers with cross-grain directions and it is therefore important to quantify the effect of this parameter on the joint properties.

The work presented in this chapter aims at understanding the mechanical behavior of welded wood joints in mixed mode loading. The following topics are investigated: 1) the influence of the wood fibers orientation on the mechanical properties, 2) the isotropy of the mechanical properties in the plane of the joint and 3) the characterization of mixed mode fracture behavior. Welded pieces with various fibers orientation are produced by linear friction welding and specimens are machined in these pieces. A strength analysis is performed in tensile, shear and one mixed mode using an Arcan device to investigate the maximal strengths of the welded joint. FE modeling is used to design the specimen shape in order to achieve the best homogeneous stress distribution over the welded joint. Fracture investigations are carried out using the same experimental device but with pre-cracked specimens loaded at various angles inducing different mode mixity. FE modeling associated to VCCT is used to separate the ERR and to determine a criterion for mixed-mode fracture of welded wood joints.

7.1 Strength analysis

7.1.1 Specimen design

Before manufacturing the specimens, parametric studies are performed using a numerical model to investigate the effect of the geometry of the specimens on the stress distribution onto the joined interface.

A 3D model is built and consists of two 3D deformable parts representing the two adherents of

the joint. Each part is assigned its own cylindrical coordinate system that serves as reference for the material orientation. The origin of the coordinate system is situated at a distance of 300 mm from the center of the part to represent the actual year ring orientation. The Arcan device is modeled according to its real dimensions, but its gripping system is simplified and modeled as a rigid steel block and therefore elastic properties of steel are used ($E=210$ GPa, $\nu=0.3$) and the specimen is then attached to this with a tie constrain. The geometry and the arrangement of the cylindrical coordinate systems are presented in figure 7.1.

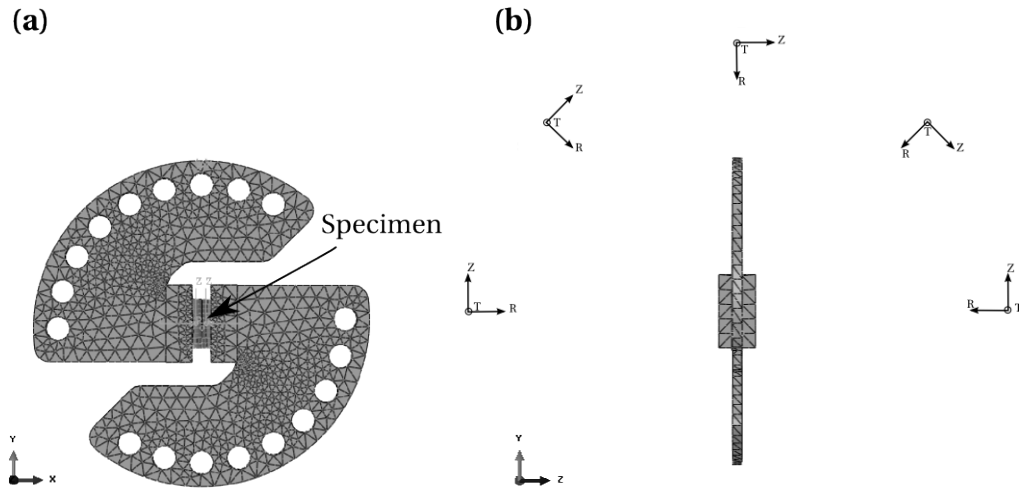


Figure 7.1: (a) View of the Arcan setup and specimen as modeled in Abaqus. (b) Organization of the cylindrical coordinate systems around the part. In this case, the R, T and Z axes represent respectively the radial, tangential and longitudinal directions.

A tie constraint is used to link the two wood adherents and the load is applied on a reference point situated at the center of the loading hole of the Arcan device, which is itself linked to the internal surface of the hole by a link MPC. Furthermore, the displacement of this control point is limited to the direction of loading. The opposite reference point is similarly linked to the device and constrained by a pin boundary condition.

In order to evaluate the stress distribution on the interface between the wood pieces and show the effect of different types of grooves, the shear and tensile stresses on a path running along the length of the specimen in the middle of the surface are calculated using the FE model. Figure 7.2 shows the influence of a selection of side groove geometries on normal and shear stress distribution in the joint. The stress values are all normalized to the value in the middle of the profile, and, since the length of the joint varies with the type of groove, the distances are also normalized in this graph. In the case of shear testing, it is found that the optimal solution is a groove with a 45° angle, while, in contrast, it is more advantageous to avoid any groove for the tensile test. It must be noted that the variation of stress in the width is very limited.

When the grain orientation is not in the load direction, attention must be paid not only to the

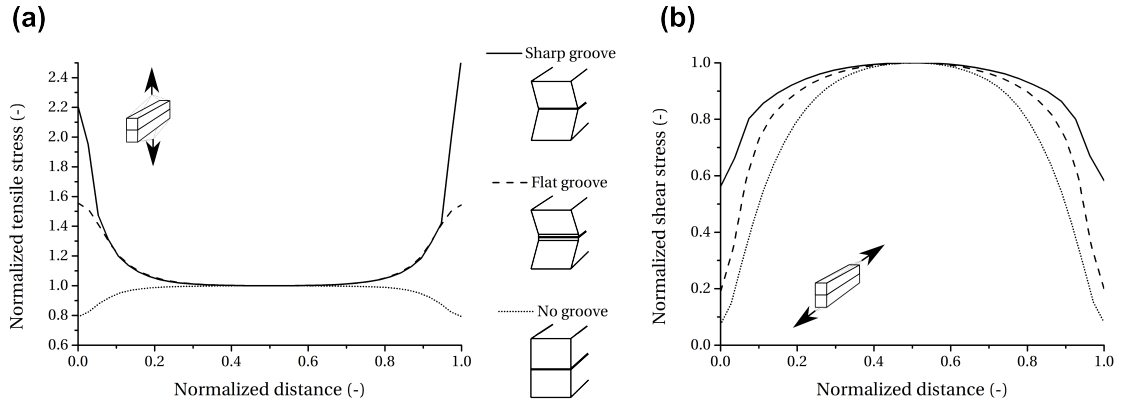


Figure 7.2: (a) Distribution of tensile stress along the interface during tensile test. (b) Distribution of shear stress during shear test. Both graphics show the influence of cut grooves on the sides of the specimens.

stress distribution on the welded interface, but also in the wood. This is the case, for example, for the 0-0 *Long* specimens loaded in pure shear, where both failure in the wood and in the joint are observed (figure 7.3(a)). Numerical analysis shows that under these conditions, high shears (figure 7.3(b)) and tangential tensile stresses (figure 7.3(c)) develop in the bulk of the wood near the free edges or close to the interface. The values of tangential tensile stresses (5.4 MPa) given by the FE modeling are close to the maximal strength reported by Ozyhar et al. [132] and could lead to bulk failure in the wood, while the shear stresses could explain a deviation of the crack from the interface into the wood.

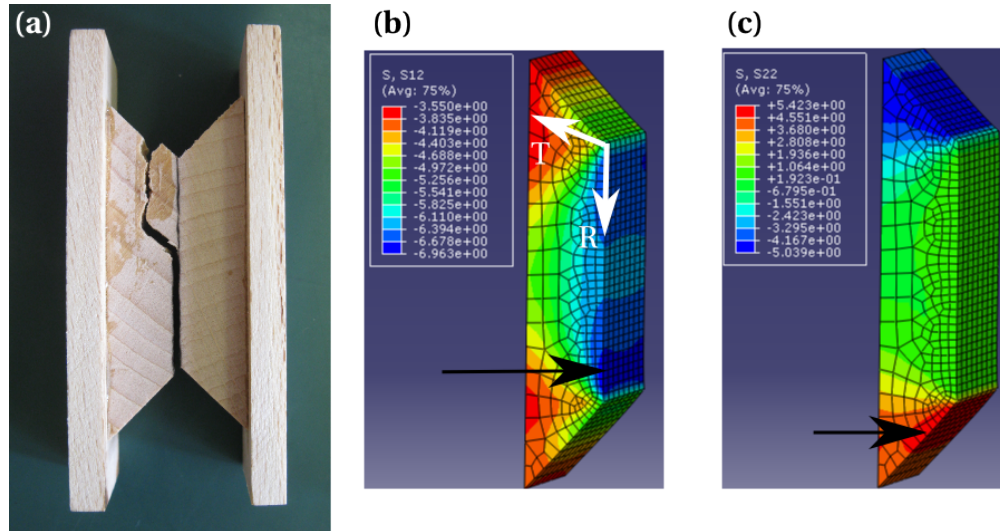


Figure 7.3: (a) Example of specimen that encountered a combined failure in the wood and in the joint. (b) t-r shear stresses distribution in the wood. (c) Tensile stresses in the tangential direction in the wood. The high stress regions are indicated with black arrows.

Attempts to experimentally discriminate between failure initiation in the wood or in the joint were not successful, even with the help of a high speed camera during the test (6000 frame per seconds). After several trials, it appeared to be impossible to design a specimen shape where tangential and radial tensile stresses and shear stresses are all sufficiently reduced. Indeed, the height cannot be reduced and a shorter length results in specimens that are difficult to handle without breaking. Finally, to circumvent this issue in this specific case, the wood surface of the specimens is covered with a thin layer of epoxy resin, which is just sufficient to avoid crack initiation on the free edges of the wood block and restrict total failure in the joint.

Figure 7.4 shows the influence of the angle of the groove on both the tensile and shear stresses distribution along the interface for a loading angle of 45° . In this case, a groove with an angle of 80° is chosen as the best compromise between shear and tensile stresses uniformity. Since the profiles of stresses are considered sufficiently homogeneous in the optimized configurations, the maximal strengths of the joint are computed as the ratio of the experimental failure load over the tested area (average nominal stress).

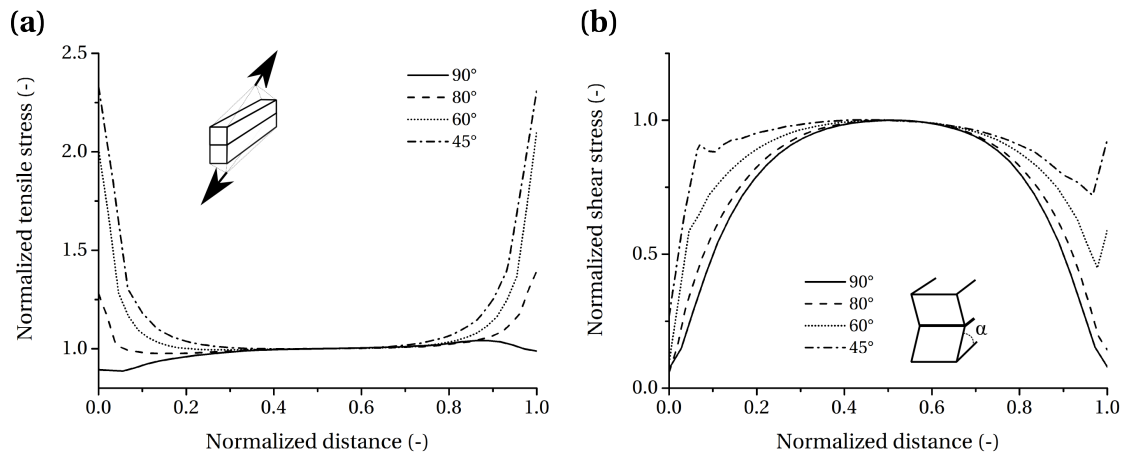


Figure 7.4: Effect of the groove's angle on the (a) tensile and (b) shear stress distributions with a mixed loading.

As specified in section 3.1 the ideal angle of the year ring with the joint interface is 90° . In practice, this condition is not always simple to achieve for each specimen, but numerical analysis showed that for all loading angles, a deviation of this angle up to 45° , which is an extreme case, does not induce more than a 1.8% variation of the stresses on the joint.

7.1.2 Maximal Strength

The measured values of maximal strengths for each group of specimens and for three different loading angles are presented in figure 7.5. Each bar on the graphs represents the average of 5 tested specimens. Despite the sometimes elevated scatter, an ANOVA analysis of all the data confirms that both the in-plane direction (*Long*, *Trans* and *Mid*) and the fibers orientation

(0-0, 0-45 and 0-90) have no influence on the maximal strength of the welded joint, because no statistical difference is observed and the null hypothesis H_0 is accepted with a p-value equal to 0.15, 0.81 and 0.96 for tensile, shear and mixed loading respectively.

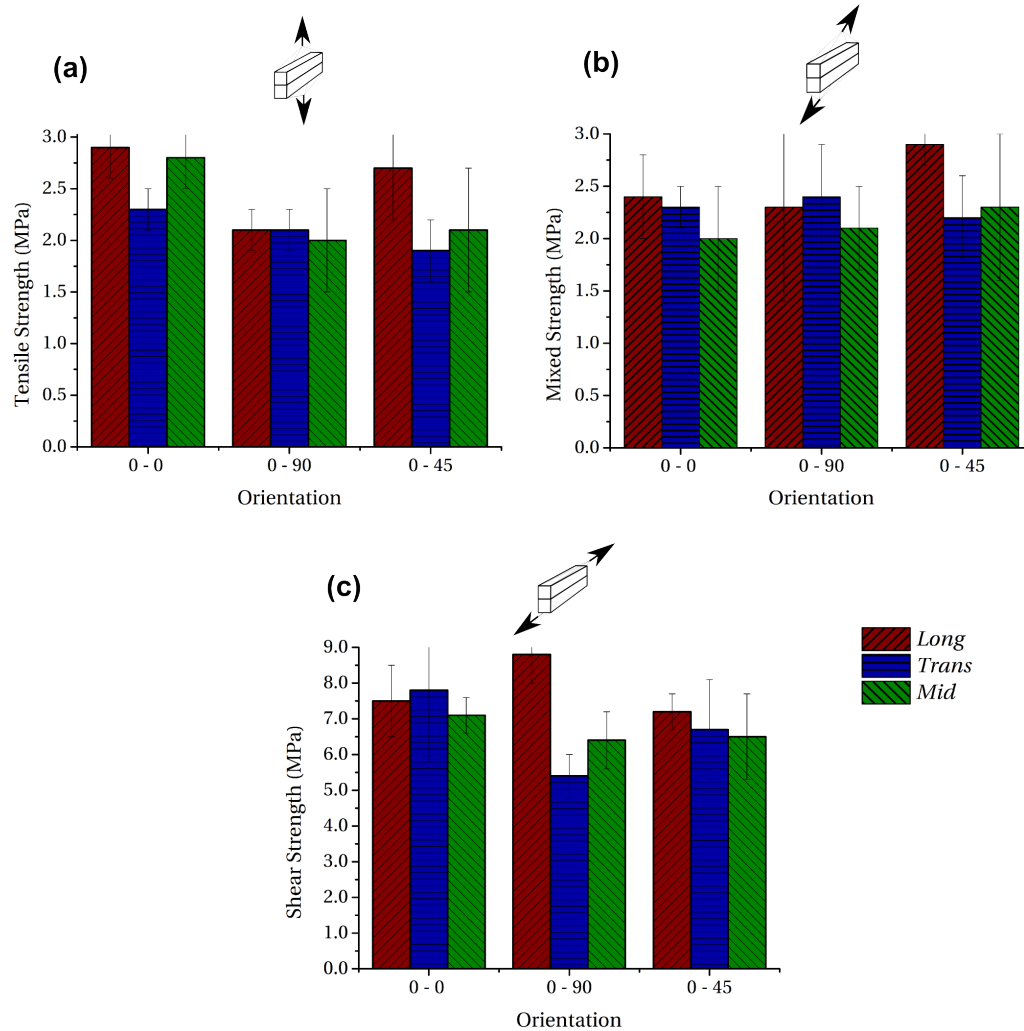


Figure 7.5: Maximal tensile (a), mixed (b) and shear (c) strength measured with the Arcan test.

The results show that the mechanical properties of the joining material can be considered isotropic and that the orientation of the wood fibers during the welding is not a process parameter that has a strong influence on the strength properties of the joining material. Therefore, the maximal strength value can be calculated for each loading angle, by averaging the values of all groups in tensile, mixed and shear loading. The results are summarized in table 7.1. The mixed mode strength value is very close to the tensile strength and seems to indicate that, although the 45° loading angle generates a mixed tensile and shear stress state at the joined interface, the specimens fail at the same level of stress as in tension.

The strength values determined by Ginest et al. [94] with uncracked welded beech specimens

Loading angle	Maximal Strength (MPa)
90° (<i>Tensile</i>)	2.3 ± 0.4
45°	2.3 ± 0.3
0° (<i>Shear</i>)	7.0 ± 1

Table 7.1: Maximal strength value determined with the Arcan test.

(1.73 and 4.64 MPa for respectively tensile and shear strength) are closer to the pure modes values from the notched specimens of this work (see figure 7.13) than the plain strength ones. The shape of the envelop is also very different in mixed mode loadings. In this work, the welding parameters, the Arcan device and the specimens' dimensions are different than those used by Ginest et al. [94] and no direct comparison is therefore possible, but it shows that production parameters and testing conditions have a large influence on the results. However, the strength properties measured in this study are consistent with the results of Ganne-Chedeville et al. [133], who measured shear strength with a tensile shear test of about 8 MPa for beech with similar welding frequency, time and wood MC. Furthermore, and although the testing methods are different, the maximal strength in tension and shear values are similar to those measured in sections 5.1.2 and 6.1.2, respectively, within less than 15% variation.

7.2 Critical energy release rate

For mixed mode fracture analysis, VCCT is used to compute and separate the ERR's on the CTS specimen in a 3D model during a static analysis. A 3D model is used so that the profile of the ERRs along the whole crack front can be investigated. The joint is defined as a master-slave contact pair in the initial conditions, leaving a 20 mm pre-crack on one side. In order to use VCCT to calculate mode mixity, the debonding is enabled in the loading step with a VCCT energy-based crack propagation criterion (equation 3.7). Since propagation is not of interest and only the onset of the propagation situation is modeled, all the critical values of ERR (G_{Ic} , G_{IIc} , G_{IIIc}) and the mixed mode parameters (n , m , p) are set to unity. Subsequently, the effective ERR ratio expressed in equation 3.7, which is a direct output variable, becomes equal to the total ERR.

The volumes of the parts are meshed with linear 3D stress brick elements (C3D8R). The mesh size in the direction normal to the joint plane is set to 0.5 mm and 5 mm in the direction of the crack propagation based on a mesh convergence study. It should be noted that the values of ERR converge when decreasing the element height, but comparatively long element lengths are needed to avoid the effect of oscillating stresses and ERR near the crack front. This is illustrated in figure 7.6.

Figure 7.7 shows examples of ERR values along the crack front for different loading angles corresponding to those experimentally tested (0°, 15°, 30°, 45° and 90°). Except for some side effects, the values of ERR are constant all along the crack front. This numerical analysis

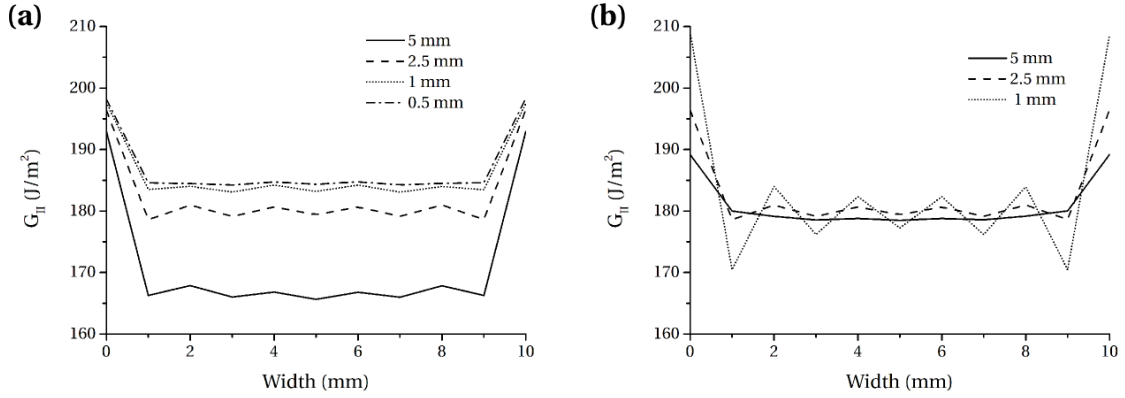


Figure 7.6: (a) Effect of the element's height on the values of G along the crack front. The element length is constant and equal to 2.5 mm. (b) Effect of the element's length along the interface on the values of SERR along the crack front. The height of the elements is constant and equal to 2.5 mm.

enables verifying that the experimental setup gives a well determined pure mode I or pure mode II when loaded at, respectively, 90° and 0° as only G_I or G_{II} values are significant in those cases.

It is revealed that mixed modes seems to occur only when the loading angle is between 0° and 45° , where the mixed mode ratio G_{II}/G_T is equal to 0.08 (figure 7.8). When loading angles are higher than 45° , mode I is even more dominant. The mixed mode ratio is mostly determined by the angle of loading but also partially by the experimental setup (experimental device, specimen geometry, etc ...) and the material properties. This explains why the 0-0 and 0-90 specimens have slightly different mixed mode ratios at the same loading angle.

The experimental load-displacement curves obtained with the Arcan test and the pre-cracked specimens show that unstable crack propagation occurs once the initiation conditions are fulfilled. Therefore, for each specimen, the experimental load at failure is taken as a critical value and is inserted in the numerical model as a loading condition and the calculated ERR's are considered as the critical ERR values. The process to evaluate the data is summarized in figure 7.9. The values of G_{III} are considered negligible and are therefore not reported hereafter.

Figure 7.10 shows the results on a graph giving the values of G_I and G_{II} for all specimens. Each graph presents the results for one of the two different types of fiber orientations (0-0 and 0-90, respectively). The scatter is generally high and mostly due to heterogeneity of the wood and joining material. It is interesting to mention that, in both types of orientation, the introduction of a small ratio of mode II leads to a drastic drop of the fracture energy, even more pronounced for the 0-0 specimens. The critical ERR in pure modes are similar for both welding orientation, but the 0-90 welding orientation seems to have slightly better resistance in mixed mode. Although quite unusual, the fact that the total ERRs are smaller in mixed mode than in pure modes was already reported by Tschegg et al. [79] for wood and Singh et al. [80]

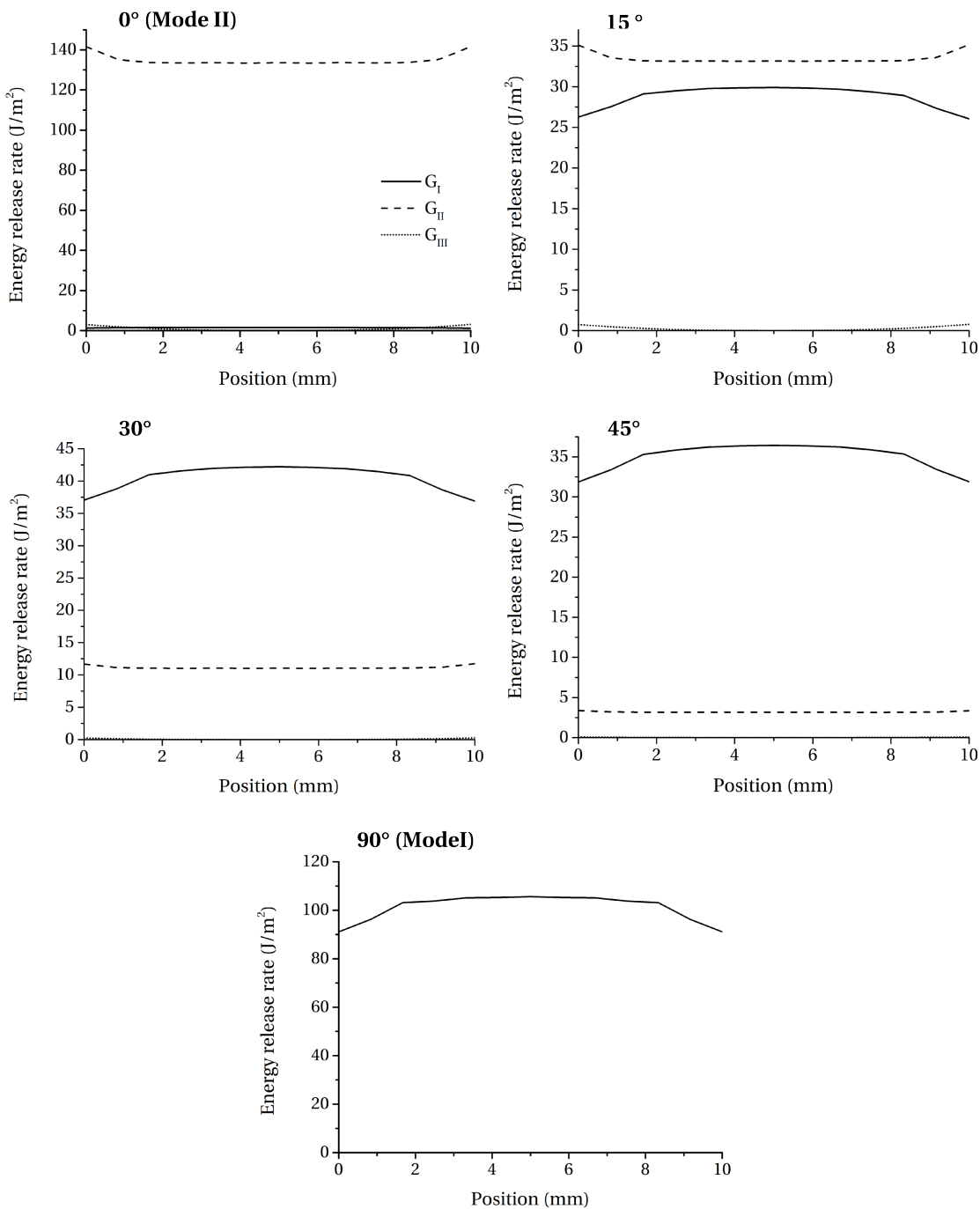


Figure 7.7: Examples of ERR profile along the crack front for each loading angles tested in the experimental part. The loads used in the model are the average of the experimental maximal loads of each group.

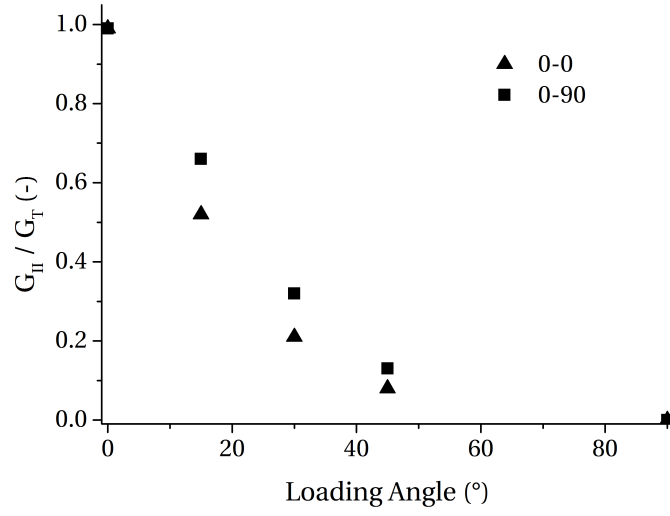


Figure 7.8: Evolution of the mixed mode ratio with the loading angle for both types of specimen orientation.

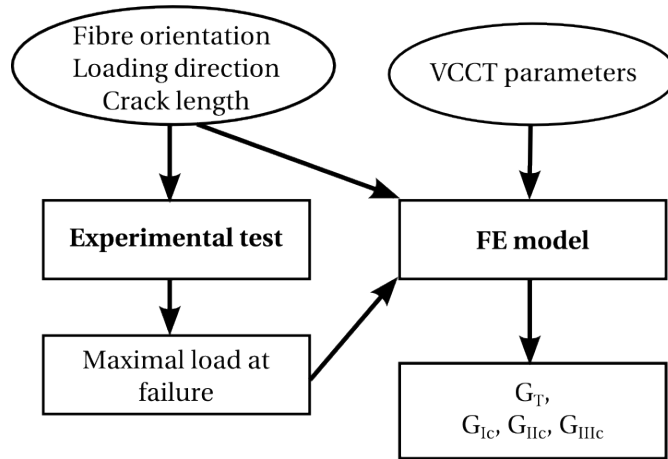


Figure 7.9: Flowchart presenting the process to determine the critical ERR by combining an experimental and numerical approach.

for wood adhesive. The following power expression is used to express the fracture criterion [134, 135].

$$\left(\frac{G_I}{G_{Ic}} \right)^n + \left(\frac{G_{II}}{G_{IIc}} \right)^m \geq \phi^2 \quad (7.1)$$

In equation 7.1, the critical values G_{Ic} and G_{IIc} are computed from the average of the specimens tested with loading angles of 90° and 0° , respectively. The ϕ^2 value is calculated for

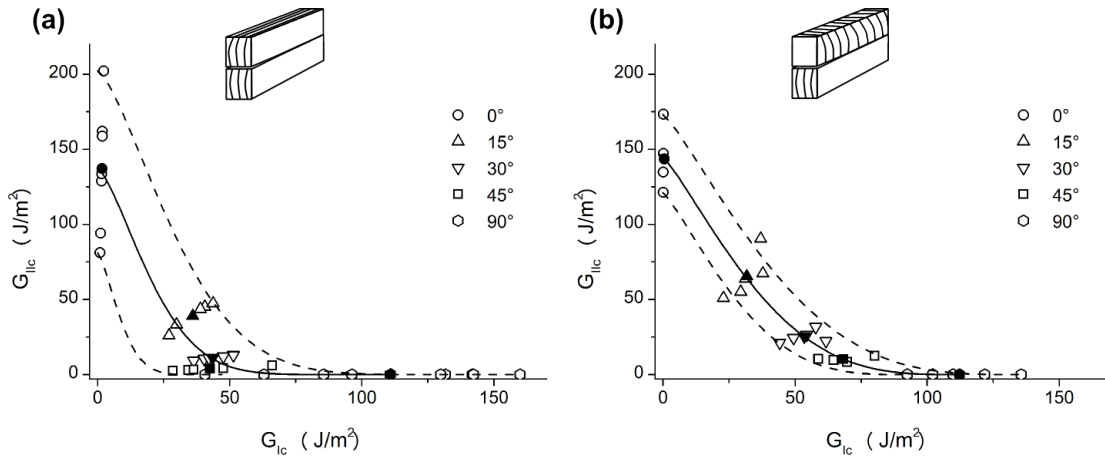


Figure 7.10: ERR values determined with combined Arcan experiment and VCCT, (a) for the 0-0 specimens and (b) for the 0-90. The empty symbols are the individual ERR value for each specimen. The filled symbols show the average value of each group of specimen tested with the same loading angle.

each specimens and the distribution is compared with a normal distribution, which enables identifying the outliers that are consequently excluded from the calculation. The parameters n and m are determined with a least square fitting of the experimental data and are presented in table 7.2. A fracture envelop is determined for ϕ^2 smaller or equal to one, presented on figure 7.10 and shows an unexpected concave shape, highlighting the high sensitivity of the welded joint to mixed mode loading.

Parameter	0-0	0-90
G_{Ic} (J/m²)	110	112
G_{IIc} (J/m²)	137	144
n	1.43	1.22
m	0.12	0.30

Table 7.2: Parameters of the mixed mode power expression (equation 7.1)

By keeping the n and m parameters and using the maximal and minimal values of the pure modes as G_{Ic} and G_{IIc} , one can draw a zone that encompasses all the experimental data, hence separating a safe and critical region where failure is unlikely or certain to occur. The fact that this zone is narrower for the 0-90 specimens is mostly due to the smaller scatter of the results in the pure mode.

It is thought that a better understanding of this complex mixed mode behavior should be sought with the help of a micromechanics analysis, which was not the aim of this study. More particularly, the effect of mode mixity on the crack path within the joining material and fiber

pullout should be investigated, taking into account the heterogeneous nature of the joining material. Indeed, at a microscale and as visible on figure 7.11, the joining material is an heterogeneous mixture of voids, matrix material and wood fibers. Placencia Peña et al. [126] showed that the proportion of soluble and Klason lignin is higher in the joining material than in the wood, which shows that a new material is indeed formed. At this scale, the crack path is highly complex and can no longer be considered linear. The distribution of the fibers in the joining material seems to be random and no preferential orientations or periodical structures can be observed on these micrograph. This further supports the idea that the welding process cancels the anisotropy of the wood by creating a layer of a new isotropic composite material, whose properties are subsequently not influenced by the orientation of the surrounding wood fibers. Also interesting to mention is that the fibers are not only torn off from the wood pieces and mixed in the matrix material, but also simply lifted and embedded in the matrix material, thus offering some anchoring mechanism.

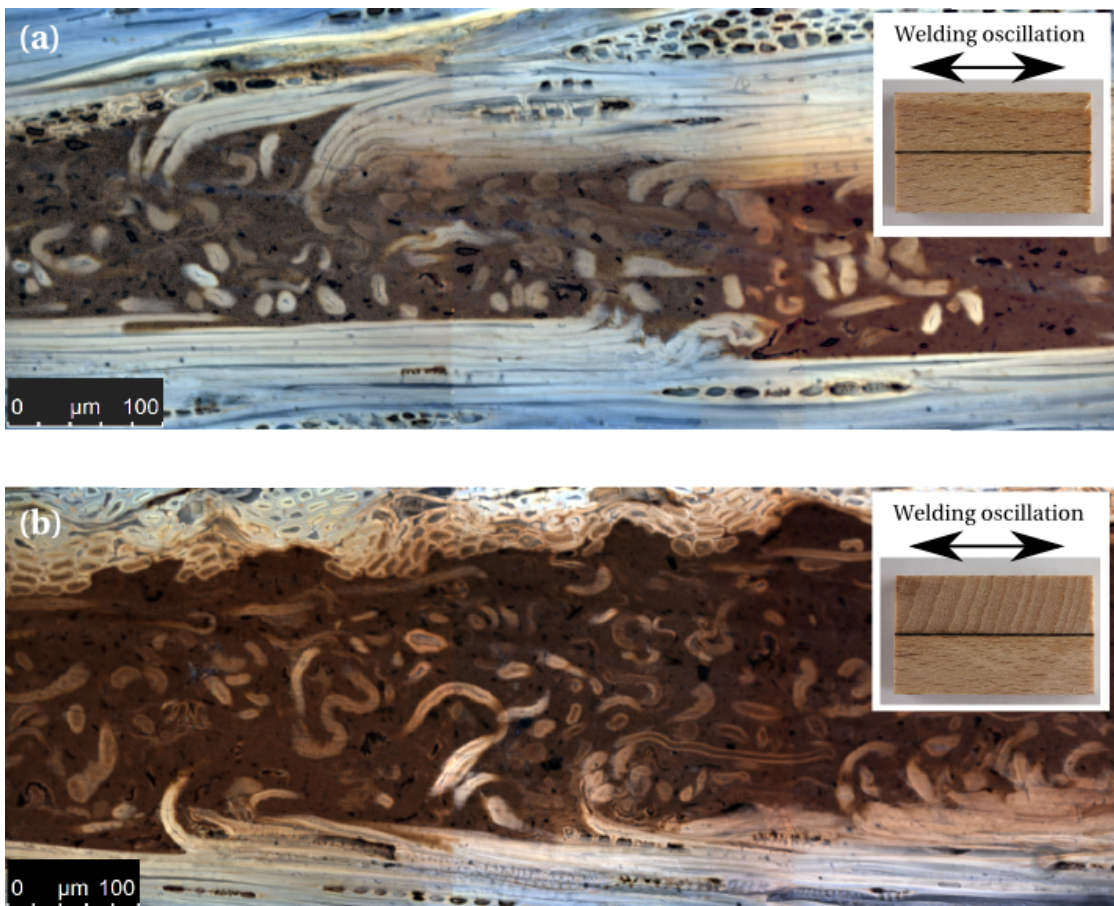


Figure 7.11: Side view of the (a) 0-0 and (b) 0-90 specimens taken with confocal autofluorescence microscopy and optical photography (box). The wood fibers are either blue or yellowish and the joining material is the brown part in the center of the images.

The observed fracture behavior might also be caused by the development of a sub-critical local

damage / plasticity region in the joining material at the crack tip, which could blunt and thus delay crack propagation in the pure mode cases. Although the exact causes for this peculiar mixed mode behavior are currently unknown, the comparison of the Arcan test results with the values determined in chapters 5, 6 and 8 show a good correlation and suggest that the fracture energies are correctly determined by the Arcan test (Figure 7.12).

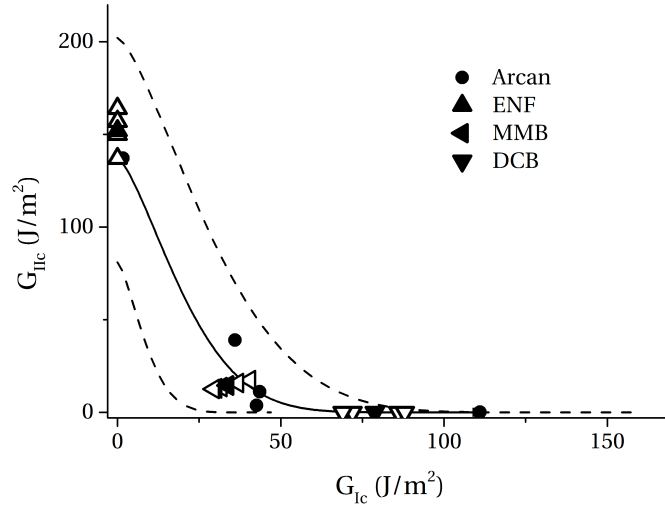


Figure 7.12: Fracture envelop for 0-0 welding orientation compared with the results of ENF, MMB and DCB test.

Figure 7.13 shows a graphical representation of the nominal tensile and shear stresses on the bonded part of the specimens, calculated according to equations 7.2 and 7.3, where P is the average maximal load for each loading angle, S is the bonded surface and α is the angle of loading.

$$\sigma_y = \frac{P}{S} \cos^2(\alpha) \quad (7.2)$$

$$\tau_{xy} = \frac{P}{S} \sin(\alpha) \cos(\alpha) \quad (7.3)$$

It is observed that the nominal stress values do not differ too much between the uncracked and pre-cracked specimens, showing that the failure of the pre-cracked specimen might not be fully driven by the fracture mechanics but also by stress-driven failure initiation.

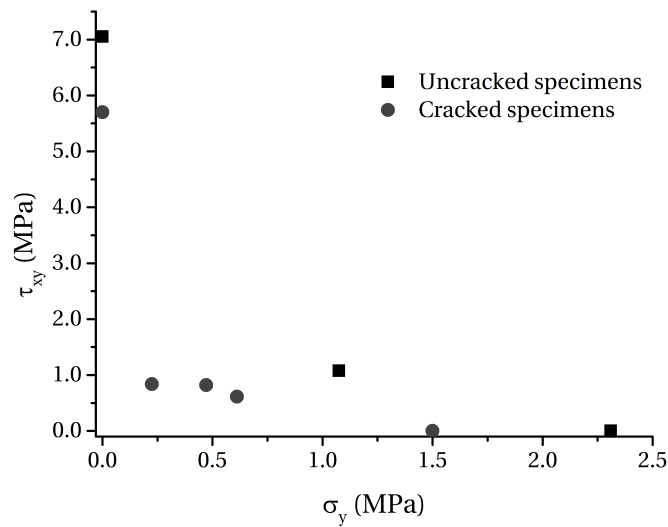


Figure 7.13: Comparison of tensile and shear stresses experienced by the bonded region of the joint for the strength (uncracked) and fracture (pre-cracked) specimens.

7.3 Summary

The chapter presents work on the mechanical characterization of the welded wood joints with an Arcan device and CTS specimens. The strength and fracture properties of welded wood joints were investigated by a coupled experimental and numerical work. The Arcan device proved to be a convenient tool to investigate the effects of mixed mode loading of wood pieces welded with parallel or cross grain direction. The tensile and shear strength of the welded joint were determined and are consistent with the results of chapters 5 and 6. Both properties seem to be statistically independent of the fibers orientation and the in-plane loading direction. Therefore, it can be stated that the fiber orientation of the wood is not an influencing parameter and that the joining material produced by the welding process is isotropic.

The experimental tests with pre-cracked specimens produced unstable crack propagation and sudden failure. The maximal experimental loads inserted in the FE model enabled to compute and separate the ERRs. Parameters for a mixed mode power fracture criterion were determined and show a concave fracture envelop with lower values of ERR in the mixed modes than in the pure modes. Following the results of this chapter, the parameters to describe the mixed mode fracture behavior of welded joints can now be used in FE modeling. These results are also presented in Rheme et al. [136].

8 Mixed mode crack propagation

After the determination of the mixed mode fracture criteria in chapter 7, it is necessary to verify that cohesive elements can be used to predict the mixed mode crack propagation in welded pieces during service life. This task is the aim of this chapter and an experimental method involving a SENB specimen with a four point bending test (4-SENB) is used to mimic the bending behavior of a welded beam with a defect. In a first approximation and to limit the influence parameters, the test is carried out in isothermal and stable humidity conditions, i.e. only external load is applied. The ASTM standard for mixed mode testing [121], which is a more established method, is carried out to verify the previous results. The experimental results are compared with FE models built with cohesive elements to predict mixed mode crack propagation. VCCT is used in parallel to evaluate and separate the ERR in the different fracture modes.

8.1 SENB specimen

As already mentioned, beam specimens with an initial crack loaded in bending are often used to study mode I fracture. However, and particularly in layered material, crack tends to propagate where the resistance is lower, i.e. in the material having the lowest critical ERR. This is typically the case for wood where the crack tend to propagate along the fibers even when the initial crack is perpendicular to these last [137]. The previous chapters have shown that independently of the fibers orientation of the wood, the crack is constrained to propagation within the joint. Therefore with a welded SENB specimen, one can expect to have a propagation perpendicular to the notch under the action of opening and shear forces, i.e. mode mixity.

In order to assess the mode mixity of the 4-SENB test geometry, the values of ERR in mode I and II are determined at the nodes of the crack front by VCCT. Hence, a 3D model is built and composed of wood parts with linear elastic properties. The elastic properties of steel are used for the supports ($E=210$ GPa, $\nu=0.3$). A symmetry boundary condition in the middle of the length of the specimen and a reference point controls the displacement of the upper support

with a rigid body MPC.

Figure 8.1(a) shows an example of the numerical model of the 0-90 specimen with a 5 mm crack and unit displacement imposed on the upper support. By varying the crack length in various static analyzes, it is possible to observe the evolution of the ERRs with crack length. For the same displacement, G_T unsurprisingly reduces with increasing crack length, but one can see that the mixed mode ratio remains constant for crack lengths from 5 to 35 mm at a value of 0.27. With longer crack length, the mixed mode ratio slightly increases until 0.31, certainly due to the influence of the upper support that is placed at a distance equivalent to 45 mm of the crack length. Thus, it can be stated that the crack propagation always occurs in the same mode mixity conditions.

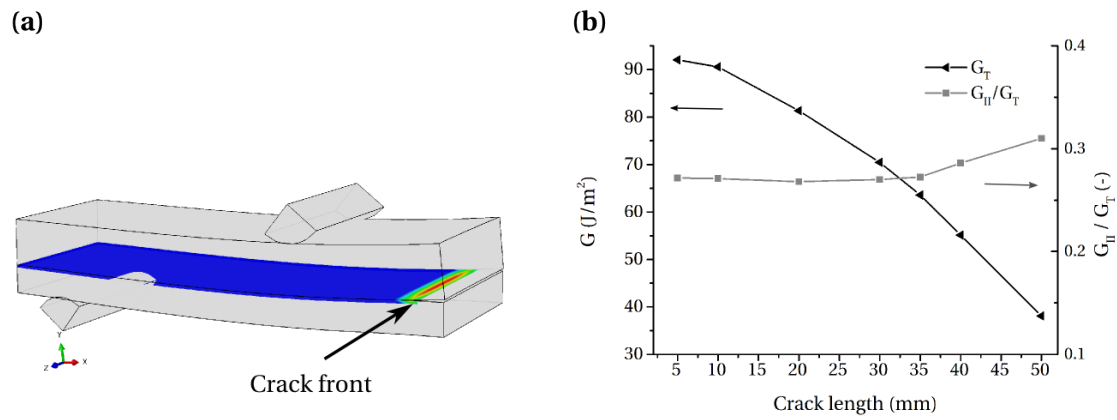


Figure 8.1: (a) FEM showing the values of G_T on the joined surfaces. Here the half specimen with a crack of 5 mm. (b) Evolution of G_T and the mixed mode ratio with increasing crack length.

8.2 4-SENB test

The load-displacement curves of the 4-SENB test are presented in figure 8.2 for the 0-90 and 0-0 specimens. The readings are consistent and all present an initial elastic domain until crack initiation and propagation occur in the joint. The 0-0 specimens are stiffer because the longitudinal direction of the thin part is aligned with the length of the specimen, but this causes higher stresses and the first crack appears earlier. Visual observations show that the onset of crack propagation happens in the range 1.45 - 2.05 mm of displacement and 0.5 - 0.8 mm of displacement for the specimens 0-90 and 0-0, respectively. Subsequently, a stable propagation confined in the joint is observed, although some sudden crack advances are sometimes noticeable. The global effect of crack propagation is a small but noticeable decrease of stiffness.

The load and displacement data for the loading and unloading cycles presented on figure 8.3 show that quite a large hysteresis happens during the cycles. The hysteresis corresponds to the

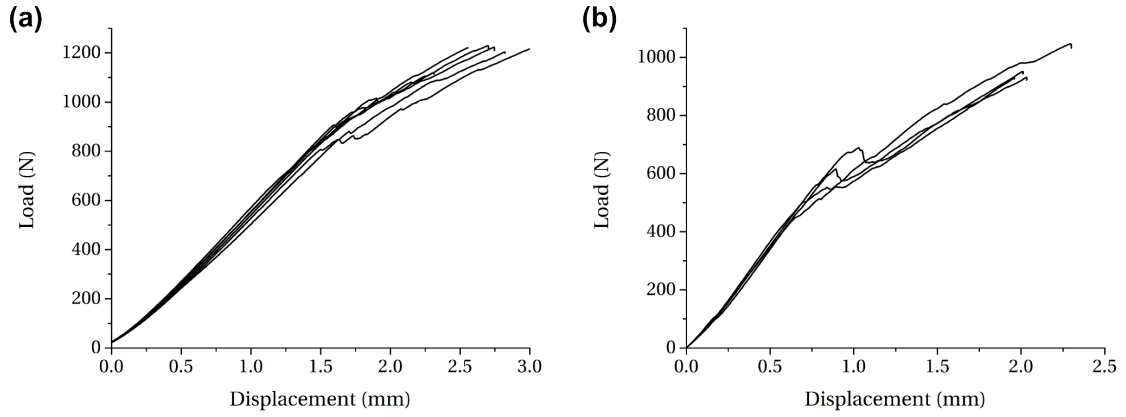


Figure 8.2: Load displacement data of the 4-SENB test for (a) 0-90 and (b) 0-0 specimens.

sum of the energies dissipated by the system, including crack propagation. The total energy dissipated during each cycle is calculated by computing the area of the hysteresis formed by the loading and unloading curves. For the 4-SENB, the onset of crack propagation occurs during the second cycle at a displacement of 0.8 mm and in the subsequent cycles, part of the energy dissipated is therefore due to crack propagation. During the MMB test, the crack propagates during all cycles.

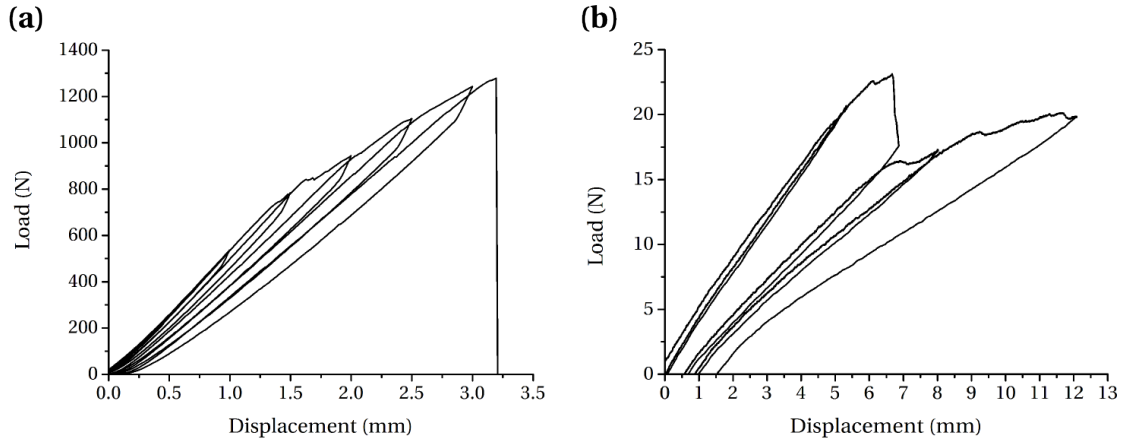


Figure 8.3: Experimental load and displacement data during loading and unloading cycles of (a) 4-SENB (0-90 specimen) and (b) MMB.

The total energy dissipation for each cycle is plotted in figure 8.4 where the results of the 4-SENB and the MMB experiments are presented. For both tests, the total crack propagation during the cycles is around 50 to 60 mm. One sees that the energy dissipated during each cycle (U^{dis}) increases markedly during the 4-SENB test, but stays more or less constant and at low levels during the MMB test. The bottom part of figure 8.4 shows the energy dissipated in each cycle divided by the corresponding increase of cracked surface (ΔS^{crack}). The relations

Chapter 8. Mixed mode crack propagation

for the mixed mode fracture criteria given in chapter 8 suggest that the total ERR (G_T) for a mode mixity of 0.3 is equal to 78.8 J m^{-2} for cross grain welding (case of the 4-SENB test) and 54.1 J m^{-2} for parallel grain welding (case of the MMB test). The measured values of energy dissipation per units of cracked surface are equal to 332 J m^{-2} for the 4-SENB (cycles 3 and 4) and to 55 J m^{-2} for the MMB (cycles 1 to 3). Therefore, the dissipated energy during the MMB test is completely due to crack propagation, whereas the high levels of dissipation during the 4-SENB test suggests that other dissipative effects occur. The real crack length of the fourth cycle of the MMB specimen cannot be visually measured, because it passes behind the loading support. An estimation is made based on the rate of crack growth but the value of $U^{dis} / \Delta S^{crack}$ for this fourth cycle must be handled with care. We can also show that the ratio of the hysteresis made by the loading curve of the $i + 1^{th}$ cycle with the unloading curve of the cycle i with U^{dis} at cycle i remains at a much more lower value in the case of MMB. This ratio also depends, of course, on the increase of crack length (Δa) during the cycle, because the higher that Δa is, the more energy dissipation that occurs during the cycle. The values concerning the cyclic tests are summarized in table 8.1 and 8.2.

Cycle Nbr i	4-SENB			
	Δa (mm)	U^{dis} (mJ)	$U^{dis} / \Delta S^{crack}$ (J/m ²)	Hyst. $i + 1, i / U^{dis}$ (-)
1	0	6.6	-	0.62
2	2	25.5	559	0.72
3	10	79.6	311	0.53
4	21	184.9	352	0.39
5	13	235.6	744	0.50
6	12	348.8	1140	-

Table 8.1: Data of the cyclic 4-SENB test.

Cycle Nbr i	MMB			
	Δa (mm)	U^{dis} (mJ)	$U^{dis} / \Delta S^{crack}$ (J/m ²)	Hyst. $i + 1, i / U^{dis}$ (-)
1	4	5.2	52	0.33
2	23	37.0	64	0.08
3	11	13.7	50	0.24
4	13	17.55	102	-

Table 8.2: Data of the cyclic MMB test.

The 4-SENB cyclic test with a holding time of 1 hour at constant displacement, suggests that the energy is dissipated mainly by time dependent effects such as visco-elasticity. Indeed, figure 8.5(a) shows that as long as no crack is present in the joint (cycle 1 to 3), the deformation of the system is recovered at zero loading and the slopes of the reloading curves are similar.

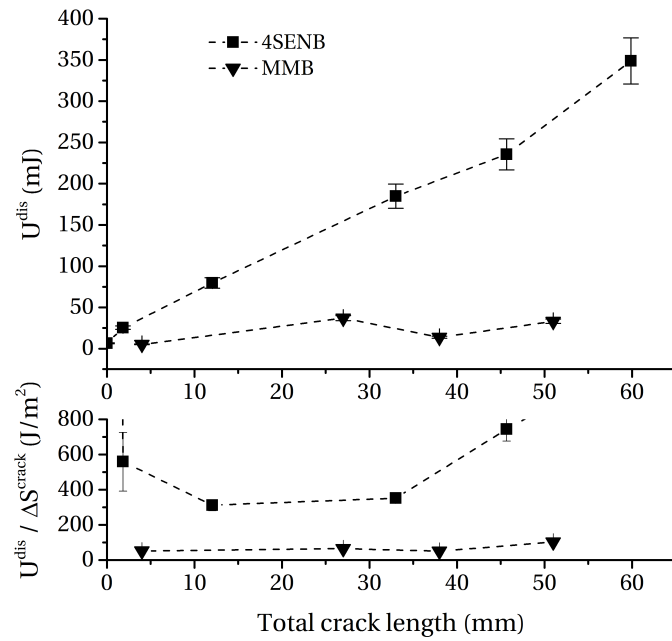


Figure 8.4: Measured dissipated energy (U^{dis}) for each cycle as a function of the observed crack length (top) and ratio of the energy dissipated to the cracked surface per cycle for the 4-SENB (squares) and MMB (triangles) experiments.

Moreover, the evolution of the load during the holding steps (figure 8.5(b)) confirms that stress relaxation occurs.

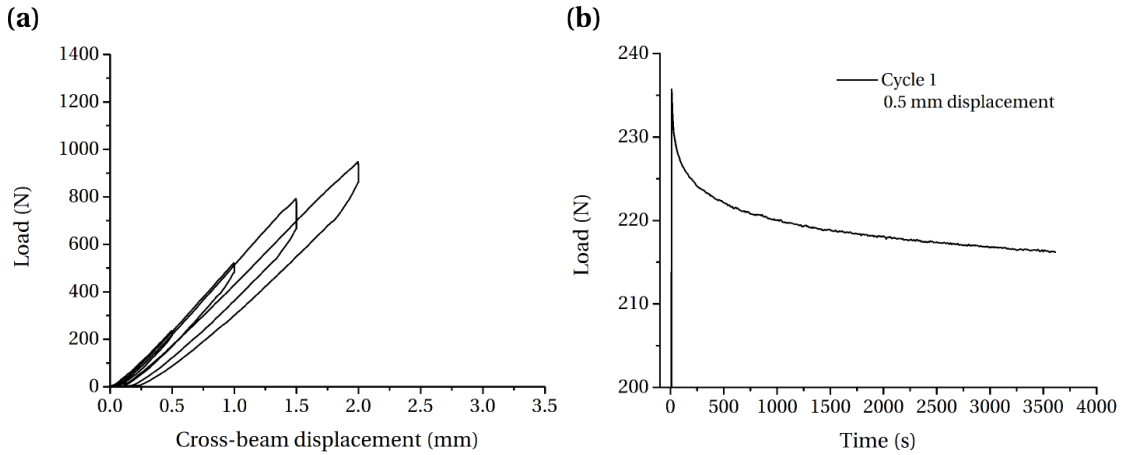


Figure 8.5: (a) Load-displacement data during cyclic loading with a holding step of 1 hour at constant displacement. (b) Evolution of the load during the holding step at 0.5 mm of displacement.

8.3 MMB test

The experimental curves of the MMB test are presented in figure 8.6(a) and show a stable crack propagation. As suggested by the ASTM standard [121], a 5% change in the compliance is taken as criteria for the crack propagation onset. This corresponds generally quite well with the visual observations made on the pictures of the lateral surface.

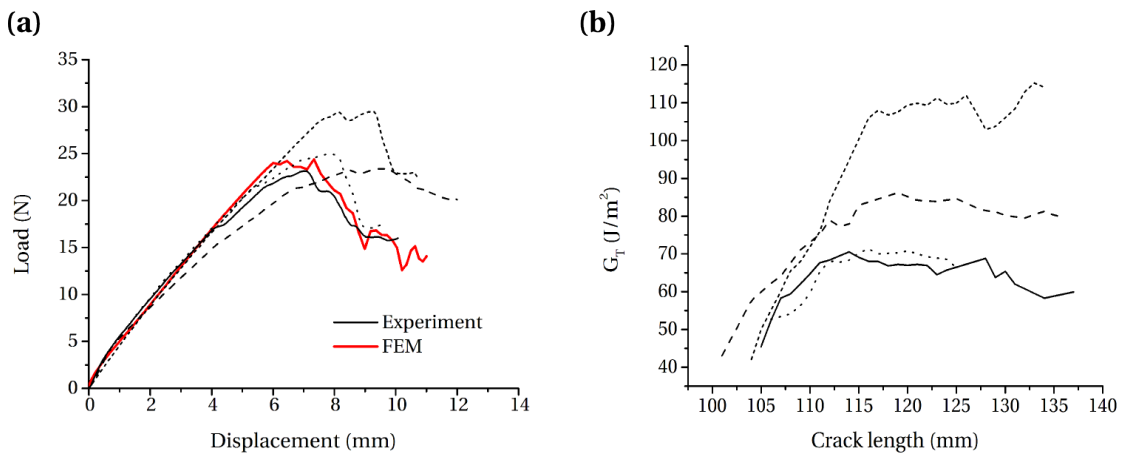


Figure 8.6: (a) Load and displacement data of the MMB test for 5 different specimens and the FE model curve. Experimental data are in black and FE results in red. (b) Corresponding curves of the evolution of G_T with the crack length.

The data reduction is an experimental compliance calibration method; i.e. the measured load P and the applied displacement enables computing the compliance C , which is plotted as a function of the crack length a and fitted with a 2nd order polynomial expression. This

expression can be derived with regards to a and G_T is calculated with the expression 2.21.

Since the mixed mode ratio is fixed to 0.3 by the settings of the experimental device, G_I and G_{II} can be easily computed from G_T . The curves showing the evolution of G_T with the crack length are presented in figure 8.6(b) for the tested specimens. The shape of the curves suggest that a toughening mechanism takes place after the initiation until the G value reaches a plateau value. Fibre bridging cannot be observed during the tests and the exact nature of the toughening is for the moment unknown. It is believed that crack branching or micro-cracking may appear in the joining material, but further investigations are needed to validate these hypotheses. If only the initiation point is considered, one can calculate an average initiation G_T equal to $48 \pm 7 \text{ J m}^{-2}$. Curiously and although the curves on figure 8.6 show different behaviors, the scatter of the initiation value is comparatively low. The mixed mode fracture criterion determined in chapter 7 (equation 7.1 with the parameters of table 7.2) gives a value for G_T equal to 54.1 J m^{-2} for the same mixed mode ratio and parallel grain welding.

Therefore, the MMB results tend to confirm the fracture criteria determined by the Arcan test in chapter 7. The behavior occurring after the maximal load (post-peak behavior) needs further work to be fully characterized and understood.

8.4 Finite elements modeling

4-SENB model

In order to model the crack propagation during loading, a 2D model is constructed with plain strain quadratic elements (CPE8R) for the wood parts and cohesive elements for the joint. The model is half of a symmetrical specimen and displacement is imposed on the upper supports (B) by a rigid body MPC. The sketch of the model is shown in figure 8.7.

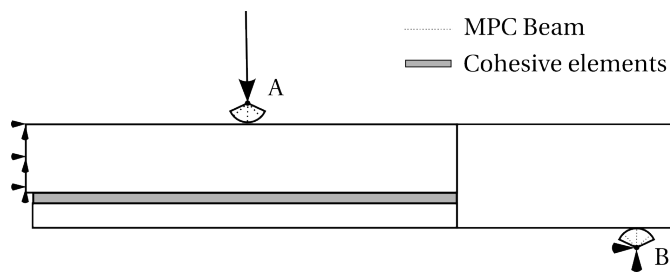


Figure 8.7: Sketch of the 4-SENB propagation model

As shown on figure 8.8(a), the load-displacement curve obtained by the crack propagation FE analysis with cohesive elements also features an elastic region before crack initiation and a subsequent propagation phase with a noticeable compliance change.

When compared with the experimental curves (figure 8.8(b)), one sees that the slope of the

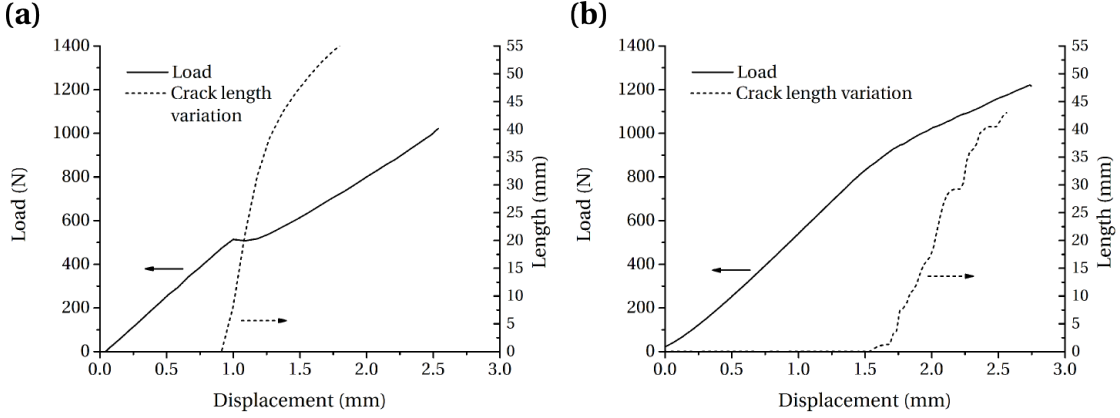


Figure 8.8: (a) Numerical load and displacement curve (plain) compared with the associated crack length (dashed). (b) Similar to (a) but for one of the experimental test.

curve in the elastic region is the same, but the change in slope of the numerical curve occurs at significantly smaller displacements. This is due to an early initiation of the crack in the cohesive elements and fast propagation. Afterwards, the propagation behavior is similar to the experiments, however the numerical crack length is longer than the experimental one at a given displacement. Static FE analyses with fixed crack length show that for the same crack length and displacement, the output load of the model is the same as the experimental one.

It is believed that the model cannot capture the viscous energy dissipation highlighted by the cyclic experiments because the wood material properties are linear elastic, which means that for the same external work, all the energy in the model is available for the propagation of the crack. An analytical solution for this particular testing configuration is proposed in Charalambides et al. [138], where the energies are expressed in terms of applied moment on the uncracked and cracked sections of the beam. The expression for the total ERR is given by:

$$G_T = \frac{M^2(1 - \nu_{lt}^2)}{2E_l} \left(\frac{1}{I_l} - \frac{\lambda}{I_c} \right) \quad (8.1)$$

where

$$\lambda = \frac{E_l(1 - \nu_{rt}^2)}{E_r(1 - \nu_{lt}^2)} \quad (8.2)$$

and M is the moment per unit width at a certain load P and for d being the distance between

the inner and outer support (in our case, $d=45$ mm).

$$M = \frac{Pd}{2b} \quad (8.3)$$

The I 's are the area moments of inertia for the complete 2-layered beam (subscript c) and for the thick layer of the beam (subscript l). the subscript r is used for the thin layer.

$$I_c = \frac{h_r^3}{12} + \frac{\lambda h_l^3}{12} + \frac{\lambda h_r h_l (h_r + h_l)^2}{4(h_r + \lambda h_l)} \quad (8.4)$$

$$I_l = \frac{h_l^3}{12} \quad (8.5)$$

Where h denotes the thickness of the layers. If equation 8.1 is used to compute the value of ERR at the onset of the propagation of the model (i.e. $P=500$ N), then the calculated value of G_T (64.5 J m^{-2}) is close to the value inputed by the mixed mode criterion in the cohesive elements (78.8 J m^{-2}). On the other hand, the experimental load at the onset of propagation (860 N) leads to a value of 190 J m^{-2} for the ERR.

Figure 8.9 illustrates what happens if all the dissipated energy were to occur at the crack front, i.e. the cohesive fracture energy is set equal to the energy calculated with the analytical model (i.e 190 J m^{-2}). The crack initiation happens at exactly the same displacement than the experimental ones (i.e. 1.6 mm). Although this shows an encouraging trend, this is not yet the solution because, as previously shown, the energy dissipation does not only occur at the crack front, but also in the bulk of the wood. Therefore, the cohesive elements alone are insufficient to describe complex structures and a global approach must be used.

For a more precise modeling of the mechanical behavior, the linear elasticity of the wood material should be reconsidered and viscoelastic properties for the wood parts may improve the precision of the predictions. This considers that a percentage of the energy available in the system is spent in the wood parts and does not contribute towards the crack propagation. This is beyond the scope of this study, but the results show that when energy dissipation is allowed only at the front of the crack, the model gives at least a conservative prediction, because propagation tends to occurs earlier than what is experimentally observed.

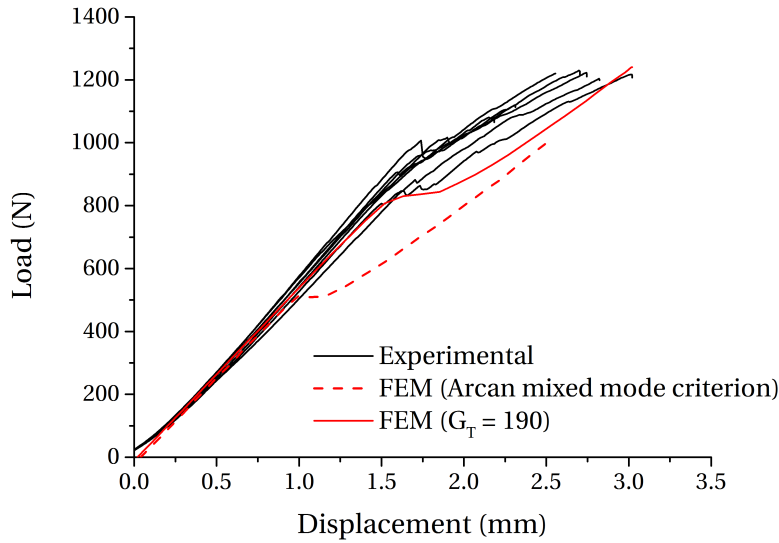


Figure 8.9: Numerical load and displacement curves (red) compared with the experimental results.

MMB model

The MMB model consists of the lever of the experimental setup that is schematically modeled with steel elastic properties and the specimen composed of quadrilateral plain strain elements (CPE8R) and is presented in figure 8.10. The cohesive element's layer has a length of 195 mm and is tied to the wood parts by a tie constraint. The interactions between the setup lever and the specimen are set up as follows: The part of the lever that indents the specimen (round part) forms a contact pair with the specimen with normal hard contact and tangential frictionless behavior. The part of the lever that pulls the specimen (tip) is linked to a 10 mm partition of the specimen with a MPC beam. An explicit calculation is used for better convergence. Reference point A is constrained to the X and Y directions and the displacement is applied on B.

Contrary to the 4-SENB test, the MMB test is correctly described with the use of cohesive elements and linear elastic wood properties and the maximal load is well predicted (figure 8.6(a)). During the MMB test there are no dissipative effects other than fracture and all the applied external work is used to propagate the crack. Indeed, the MMB specimen is based on a standard and is specially designed (as the DCB and ENF specimens are) for a correct characterization of the fracture properties, therefore it is expected that no parasitic effects take place. In contrast, the 4-SENB test is a tentative to investigate crack propagation in a near structural application.

The fact that the numerical MMB curve is coherent with the experimental ones tends to validate the cohesive mixed mode law implemented in the FE model in this work. However, for real applications and correct predictions, the material properties of the wood must be carefully selected. Furthermore, since no toughening mechanisms are taken into account in

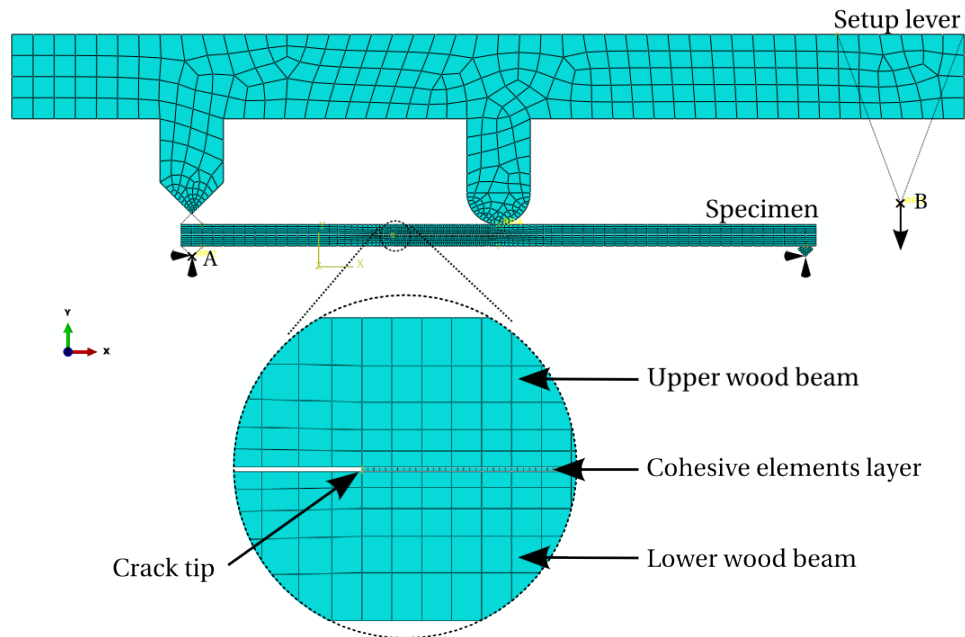


Figure 8.10: Presentation of the FE model for MMB test with a magnification of the crack tip region.

the cohesive properties, it is questionable to say that the post peak behavior is valid in mixed mode. A bilinear softening behavior for example, could improve the prediction of the model in the post peak region, but is yet to be validated by further research.

8.5 Summary

Mixed mode crack propagation in welded wood joints was investigated with experimental 4-SENB and MMB tests. FE analyses were carried out in parallel to study the levels of ERR and mode mixity (models with VCCT) or the crack propagation at the interface (model with cohesive elements). The experimental results indicate that stable crack propagation occurs, but also that the 4-SENB show a tendency to dissipate energy in the bulk of the wood due to visco-elastic effects. This situation leads to an inaccurate numerical prediction, because crack propagation was observed to initiate earlier in the model than in the experiment. However, the comparison of the MMB experimental and numerical curves seems to indicate that when no viscous dissipation occurs, the cohesive mixed mode properties used in this work give correct predictions. Improvement should be possible with the use of an appropriate material model incorporating visco-elasticity for the wood and a cohesive softening behavior, while also taking into account the observed R-curve behavior. However, it seems that in the actual

Chapter 8. Mixed mode crack propagation

state, the previously determined mixed mode cohesive properties give correct predictions and, if dissipative effects are present, a conservative prevision is achieved. The work presented here was submitted for publication [139].

9 Conclusions and future work

9.1 Conclusion

9.1.1 Effect of moisture

Firstly, moisture related properties of the materials were determined by standard testing methods to characterize the sorption isotherm and hygroexpansion coefficients of the wood. The results were found to be consistent with the values given in the literature. Additionally, diffusion tests were performed to determine the effect of the welded joints on the moisture transport through a welded part. For this purpose, the MC at different points of 3-layered welded parts were experimentally measured after a given diffusion time. The diffusion coefficient of the welded joint and wood in the tangential direction were determined by an inverse method and shows that the joint acts as a barrier for moisture transport. For better accuracy, an attempt to locate and determine the MC in welded pieces by means of neutron radiography, as was performed by Mannes et al. [29] and Sonderegger et al. [28], was carried out at the Paul Scherrer Institute, but unfortunately, experimental artifacts prevented an evaluation of the results. However, the results of this work still enables modeling the moisture transport at a macroscopic level and therefore the MC field at any time in a welded part. Subsequently, by knowing the hygro-expansion coefficients, it is now possible to determine the stress state of the joint due to swelling or shrinkage.

A second analysis of the effect of moisture was carried out with standard DCB and 4-ENF testing methods to evaluate the evolution of the fracture characteristics with MC. Specimens with various EMC between 6% and 22% were tested and their ERR in the pure modes I and II were computed. Additional tests measured the maximal tensile and shear strength at the same various EMCs. The experimental strength and fracture results showed that the properties of the welded joint strongly decreased at MC above 16%. The crack was always constrained at the joined interface and, unlike crack propagation in solid wood, no fiber bridging occurred. The loss of fracture toughness was mainly due to the poor performance of the joining material, leading to, at a macro level, a linear crack propagation in the joint without any kinking in the adherent. The experimental data were used to develop cohesive laws for the pure mode

fracture, which demonstrated a good capability to accurately predict the behavior of the welded specimens during the tests at different MC.

9.1.2 Mixed mode fracture and mechanical behavior modeling

The Arcan experimental device was used to investigate the effect of mixed loading on the mechanical behavior of the welded joint. Non-cracked specimens were tested and enabled determining that the tensile and shear strength were not dependent on the fibers orientation (parallel or cross grain welding) or on the in-plane loading direction. It was therefore concluded that the welding process produces a joining material that could be considered isotropic. Parallel and cross grain specimens with a pre-crack were tested at various loading angles, which enabled characterizing the mixed mode behavior of the joint to draw a fracture envelop. Experimental maximal loads and a virtual crack closure technique were used to separate the ERRs. The parameters for a power expression describing the mixed mode fracture of the joint were determined by fitting the experimental data. Here again, the fracture envelop of the parallel or cross grain specimens are similar in a relatively small scatter interval. The ERRs in the pure modes are more similar than those determined by the DCB and 4-ENF tests and it was shown that the stresses involved with mode mixity have proven to be very damaging for welded wood joints, i.e. the ERR in mixed modes is considerably lower than in pure modes.

It was then attempted to use the previously determined mixed mode characteristics to model the behavior of a 2-layered welded wood beam in bending (4-SENB). Specimens with a notch were tested and showed stable crack propagation in the joint, resulting in a small compliance increase of the system. VCCT was used in a static model to confirm that mode mixity occurred at the crack front, furthermore, a propagation model with cohesive elements exhibited an early crack initiation when compared with the experimental results. It was demonstrated that time dependent effects were causing energy dissipation in the system that could not be captured by the simple linear elastic properties implemented in the wood parts. This resulted in a greater amount of available energy for crack propagation, and consequently earlier crack initiation. The comparison with the MMB test at the same mixed mode ratio, where energy is consumed entirely by crack propagation, showed that the mixed mode law used with cohesive elements was suitable to model mixed mode crack propagation in welded wood joints. Furthermore, the experimental ERR computed with the MMB test enabled validating the result of the Arcan test. It is believed that a careful determination of the wood properties together with the cohesive laws determined in this work, could lead to a correct prediction of the behavior of welded wood pieces.

9.2 Future work

9.2.1 Micro mechanics

During this work, the welded joint was assumed to be a homogeneous layer of material between the two wood parts bonded together and, consequently, it was modeled as a layer of cohesive elements. At a macro-scale, it seemed sufficient to model the behavior of the welded joint at various MCs and mixed mode ratio. However, microscopic images highlighted that, at the micro-scale, the crack propagation is a much more complex phenomenon because the crack path runs either along the interface (joining material - wood) or in the joining material. Furthermore, and as shown in figure 9.1, what was called the joint is in fact a mix of joining material voids and wood fibers. The first observations made during this work with confocal microscopy showed that no penetration of the joining material in the wood parts occurred during the welding and that the adhesion was mostly due to the mechanical interlocking effect, further amplified by wood fibers still attached to the wood part and embedded in the joint. All these micro-structural features should be more intensely studied in order to better understand the fracture characteristics of the welded wood joint, particularly in mixed mode, where still open questions remain. To address these, auto fluorescence confocal microscopy seems to be an interesting tool, since the contrast it offers is impressively good. Furthermore, chemical analysis can be coupled with anatomical observation because the color reflects the chemical composition and could give good indications about chemical changes due to the welding process.

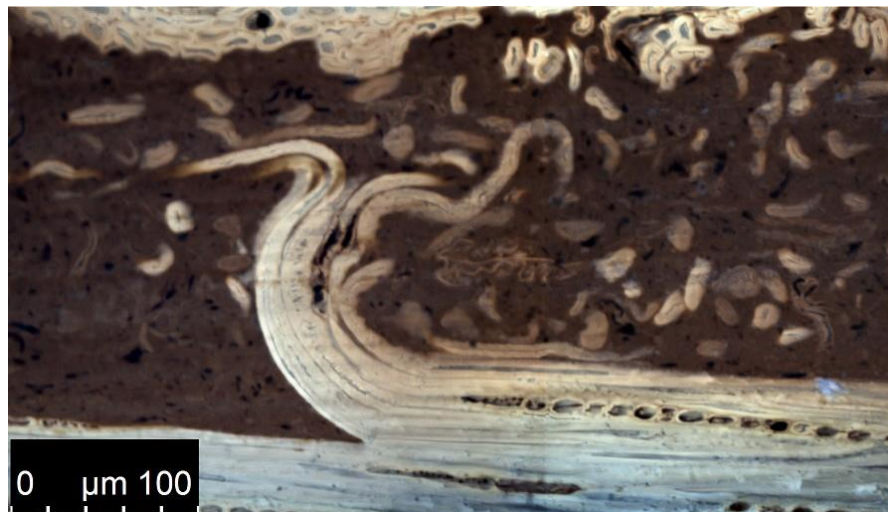


Figure 9.1: Side view of a welded joint taken with autofluorescence confocal microscopy.

9.2.2 Modeling of crack propagation with MC variation

The cohesive zone models developed in this work have showed to be suitable to predict crack propagation in welded pieces at various, but constant, MCs and temperatures. In addition to the fact that the joining material strength and fracture toughness strongly decreased at high MCs, transient moisture diffusion could also contribute to the weakening of the joint because of stresses induced by hygroexpansion. Indeed, during this work, cracking of moist specimens during uncontrolled drying was occasionally observed. Chapter 8 highlighted that the use of a correct material model is crucial for an accurate prediction of the behavior. The works of Moutou Pitti [140] in the field of wood fracture and Froidevaux [141] for the hygromechanical behavior of painted wood panels, both considered wood as a anisotropic viscoelastic media. Both also concluded that their model should be improved to take into account the effect of mechano-sorption. It is believed that a complete characterization of the wood properties could lead not only to conservative (as it is now), but also accurate predictions of the fracture behavior. Such a model would be useful for risk analysis and design of welded pieces and would help, for example, to minimize failure probability by sound choices of wood orientations and geometries or restrictions of climate.

Parallel to alternative models of wood properties, it could also be interesting to model the joint itself at a microscopic level. For example, lattice model [142] or material point models [143] have successfully modeled crack propagation in wood by considering the heterogeneous nature of wood. Such approaches to replace the cohesive elements might be useful to take into account the peculiar microstructure of the welded joint and model the rough crack path observed at microscopic levels.

9.2.3 Structure assessment

Fiber Bragg grating (FBG) sensors to measure strains are often used in the field of polymers and composite materials and a few examples are addressed in the paper of Botsis et al. [144]. A similar test to that performed by Stutz et al. [145] on fiber reinforced composite was carried out with one welded DCB specimen, but instead of embedding the FBG during the composite processing, this latter was glued on the external surface of the specimen. A good correlation between the experimental data and FE modeling was achieved (figure 9.2), but due to the relatively large distance between the crack plane and the localization of the FBG (thickness of the wood beam), no exact crack tip position could be determined and therefore further improvement of the installation process of the FBG is needed. Of course, positioning the FBG close to the welded interface is a challenging issue but it could bring valuable information about the deformations occurring not only during the test, but also during the welding process due to the local drying of the wood cells. Not much work with FBG was found in the field of wood, but Falciai et al. [146] demonstrated that it was an interesting tool to monitor hygromechanical behavior of wooden artworks. Despite their relative elevated costs, FBGs could be useful for research purposes or for the on-site monitoring of wooden structures.

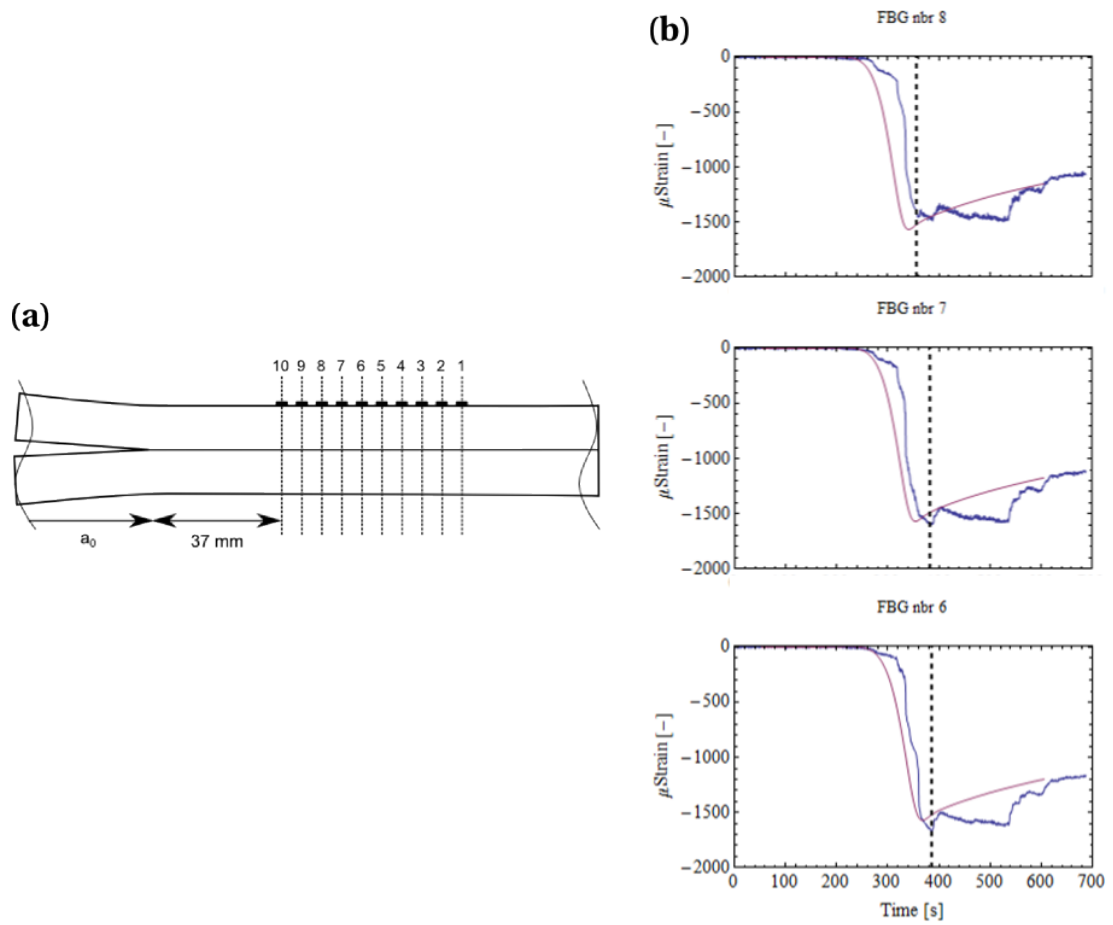


Figure 9.2: (a) Schematic representation of the position of the gratings on the DCB specimen. (b) Comparison of the experimental (blue) and numerical (purple) values of strain as function of time for three of the ten gratings. The associated observed crack tip position is indicated with the dashed line.

Bibliography

- [1] Fröhmann. *Fracture of wood on different hierarchical levels*. PhD thesis, Technischen Universität Wien, 2002.
- [2] P. Navi and D. Sandberg. *Thermo-hydro-mechanical processing of wood*. EPFL Press - Distributed by CRC Press, 2012.
- [3] B. Gfeller, M. Zanetti, M. Properzi, A. Pizzi, F. Pichelin, M. Lehmann, and L. Delmotte. Wood bonding by vibrational welding. *J. Adhes. Sci. Technol.*, 17:1573–1589, 2003.
- [4] B. Stamm, J. Natterer, and P. Navi. Joining wood by friction welding. *Holz als Roh- und Werkstoff*, 63:313–320, 2005.
- [5] L. Vorreiter. *Holztechnologisches Handbuch*, volume I. Verlag Georg Fromme & Co, Wien, 1949.
- [6] S. Ormarsson, O. Dahlblom, and H. Petersson. A numerical study of the shape stability of sawn timber subjected to moisture variation. part 1: Theory. *Wood Sci. Technol.*, 32: 325–334, 1998.
- [7] S. Ormarsson, O. Dahlblom, and H. Petersson. A numerical study of the shape stability of sawn timber subjected to moisture variation. part 2: Simulation of drying board. *Wood Sci. Technol.*, 33:407–423, 1999.
- [8] S. Ormarsson, O. Dahlblom, and H. Petersson. A numerical study of the shape stability of sawn timber subjected to moisture variation. part 3: Influence of annual ring orientation. *Wood Sci. Technol.*, 34:207–219, 2000.
- [9] P. Perré. Multiscale modeling of drying as a powerful extension of the macroscopic approach- application to solid wood and biomass processing. *Drying Technology*, 28: 944–959, 2010.
- [10] S. Wieland, B. Shi, A. Pizzi, M. Properzi, M. Stampanoni, R. Abela, X. Lu, and F. Pichelin. Vibration welding of wood: X-ray tomography, additives, radical concentration. *Forest Prod. J.*, 55:84–87, 2005.
- [11] B. Stamm. *Development of friction welding of wood - Physical, mechanical and chemical studies*. PhD thesis, Ecole Polytechnique fédérale de lausanne, 2005.

Bibliography

- [12] C. Ganne-Chedeville. *Soudage linéaire du bois: étude et compréhension des modifications physico-chimiques et développement d'une technologie d'assemblage innovante*. PhD thesis, Université Henri Poincaré, 2008.
- [13] DIN52-183. DIN 52 183 Prüfung von Holz - Bestimmung des Feuchtigkeitsgehaltes. Deutsche Normen, 1977.
- [14] C. Skaar. *Wood-Water Relation*. Springer series in Wood Science, 1988.
- [15] S. Brunauer, P.H. Emmet, and E. Teller. Adsorption of gases in multimolecular layers. *J. Am. Chem. Soc.*, 60:309–319, 1938.
- [16] R. W. Dent. A multilayer theory for gas sorption. *Text. Res. J.*, pages 145–152, 1977.
- [17] W. T. Simpson. Predicting equilibrium moisture content of wood by mathematical models. *Wood and Fibre*, 5:41–49, 1973.
- [18] R.M. Nelson. Diffusion of bound water in wood. *Wood Sci. Technol.*, 20:125–135, 1986.
- [19] J.F. Siau. Chemical potential as a driving force for nonisothermal moisture movement in wood. *Wood Sci. Technol.*, 17:101–105, 1983.
- [20] C. Skaar and J.F. Siau. Thermal diffusion of bound water in wood. *Wood Sci. Technol.*, 15:105–112, 1981.
- [21] C. Skaar and M. Babiak. A model for bound-water transport in wood. *Wood Sci. Technol.*, 16:123–138, 1982.
- [22] C. Skaar. Analysis of methods for determining the coefficient of moisture diffusion in wood. *Forest Prod. J.*, 4:403–410, 1954.
- [23] J. Weres, W. Olek, and R. Guzenda. Identification of mathematical model coefficients in the analysis of the heat and mass transport in wood. *Drying Technology*, 18:1697–1708, 2000.
- [24] J. Weres and W. Olek. Inverse finite element analysis of technological processes of heat and mass transport in agricultural and forest products. *Drying Technology*, 23: 1737–1750, 2005.
- [25] W. Olek, P. Perré, and J. Weres. Inverse analysis of the transient bound water diffusion in wood. *Holzforschung*, 59:38–45, 2005.
- [26] E. Agoua, S. Zohoun, and P. Perré. A double climatic chamber used to measure the diffusion coefficient of water in wood in unsteady-state conditions - determination of the best fitting method by numerical simulation. *International Journal of Heat and Mass Transfer*, 44:3731–3744, 2001.

-
- [27] W. Olek and J. Weres. Effects of the method of identification of the diffusion coefficient of modeling bound water transfer in wood. *Transport in Porous Media*, 66:135–144, 2007.
- [28] W. Sonderegger, S. Hering, D. Mannes, P. Vontobel, E. Lehmann, and P. Niemz. Quantitative determination of bound water diffusion in multilayer boards by means of neutron imaging. *European Journal of Wood Product*, 68:341–350, 2010.
- [29] D. Mannes, W. Sonderegger, S. Hering, E. Lehmann, and P. Niemz. Non-destructive determination and quantification of diffusion processes in wood by means of neutron imaging. *Holzforschung*, 63:589–596, 2009.
- [30] Thomas Gereke. *Moisture-induced stresses in cross-laminated wood panels*. PhD thesis, Swiss Federal Institute of Technology Zurich, 2009.
- [31] J. Bodig and B. A. Jayne. *Mechanics of wood and wood composites*. Krieger Publishing Company, 1982.
- [32] P. Niemz. *Physik des Holzes und der Holzwerkstoff*. DRW-Verlag, 1993.
- [33] J.M. Dinwoodie. *WOOD, Nature's Cellular, Polymeric Fibre-composite*. The Institute of Metals, London, 1989.
- [34] S. Hering, D. Keunecke, and P. Niemz. Moisture-dependent orthotropic elasticity of beech wood. *Wood Sci. Technol.*, 46:927–936, 2012.
- [35] D. Broek. *Elementary engineering fracture mechanics*. Maritnus Nijhoff Publisher, Dordrecht, 1987.
- [36] A. A. Griffith. The phenomena of rupture and flow in solids. *Philosophical Transactions of the Royal Society of London*, 221:163–197, 1921.
- [37] I. Smith, E. Landis, and M. Gong. *Fracture and Fatigue in Wood*. Wiley, 2003.
- [38] A. Hillerborg. Application of the fictitious crack model to different types of materials. *Int. J. Fracture*, 51:95–102, 1991.
- [39] S. E. Stanzl-Tschegg and P. Navi. Fracture behavior of wood and its composites. a review. *Holzforschung*, 63:139–149, 2009.
- [40] P. Navi and S.E. Stanzl-Tschegg. Micromechanics of creep and relaxation of wood. a review cost action e35 2004-2008:wood machining-micromechanics and fracture. *Holzforschung*, 63:186–195, 2009.
- [41] G. Pluvillage. *La Rupture du Bois et de ses Composites*. Cépaduès-Editions, 1992.
- [42] S. Vasic and S. Stanzl-Tschegg. Experimental and numerical investigation of wood fracture mechanisms at different humidity levels. *Holzforschung*, 61:367–374, 2007.

Bibliography

- [43] A. Majano-Majano, M. Hughes, and J. L. Fernandez-Cabo. The fracture toughness and properties of thermally modified beech and ash at different moisture contents. *Wood Sci. Technol.*, 46:5–21, 2012.
- [44] W. Liyu, L. Zhenyou, and Z. Guangjie. Wood fracture pattern during the water adsorption process. *Holzforschung*, 57:639–643, 2003.
- [45] D. E. Kretschmann and D. W. Green. Modeling moisture content-mechanical properties relationship for clear souther pine. *Wood Fiber Sci.*, 28:320–337, 1996.
- [46] G. Prokopski. Influence of moisture content on fracture toughness of wood. *Int. J. Fracture*, 79:R73–R77, 1996.
- [47] H. Yoshihara and T. Kawamura. Mode I fracture toughness estimation of wood by DCB test. *Composites Part A: Applied Science and Manufacturing*, 37:2105 – 2113, 2006. ISSN 1359-835X.
- [48] H. Yoshihara. Simple estimation of critical stress intensity factors of wood by tests with double cantilever beam and three-point end-notched flexure. *Holzforschung*, 61: 182–189, 2007.
- [49] M.F.S.F de Moura, J.J.L. Morais, and N. Dourado. A new data reduction scheme for mode I wood fracture characterization using the double cantilever beam test. *Eng. Fract. Mech.*, 75:3852–3865, 2008.
- [50] S. E. Stanzl-Tschegg, D. M. Tan, and E. K. Tschegg. New splitting method for wood fracture characterization. *Wood Sci. Technol.*, 29:31–50, 1995.
- [51] A. Reiterer, G. Sinn, and S. E. Stanzl-Tschegg. Fracture characteristics of different wood species under mode I loading perpendicular to the grain. *Materials Science and Engineering*, A 332:29–36, 2002.
- [52] A. Reiterer and S. Tschegg. The influence of moisture content on the mode I fracture behaviour of sprucewood. *Journal of Material Science*, 37:4487–4491, 2002.
- [53] L. Daudeville. Fracture in spruce: experiment and numerical analysis by linear and non linear fracture mechanics. *Holz al Roh- und Werkstoff*, 57:425–432, 1999.
- [54] S. Morel, N. Dourado, G. Valentin, and Morais J. Wood: a quasibrittle material r-curve behavior and peak load evaluation. *International Journal of Fracture*, 131:385–400, 2005.
- [55] N. Dourado, S. Morel, M.F.S.F de Moura, G. Valentin, and Morais J. Comparison of fracture properties of two wood species through cohesive crack simulation. *Composites Part A: Applied Science and Manufacturing*, 39:415–427, 2008.
- [56] M.F.S.F de Moura, N. Dourado, and Morais J. Crack equivalent based method applied to wood fracture characterization usign the single edge notched -three point bending test. *Engineering Fracture Mechanics*, 77:510–520, 2010.

-
- [57] H. Yoshihara. Examination of the mode I critical stress intensity factor of wood obtained by single-edge-notched bending test. *Holzforschung*, 64:501–509, 2010.
- [58] G. Duchanois. *Mesure de la ténacité et étude du comportement mécanique des joints bois-colle*. PhD thesis, Institut national polytechnique de Lorraine, 1984.
- [59] H. Wernersson. Fracture characterization of wood adhesive bonds. In *International Timber Engineering Conference*, 1991.
- [60] J. M. Gagliano and C. E. Frazier. Improvement in the fracture cleavage testing of adhesively-bonded wood. *Wood Fiber Sci.*, 33:377–385, 2001.
- [61] M.P.C Conrad, G.D. Smith, and G. Fernlund. Fracture of discontinuous wood-adhesive bonds. *Int. J. Adhes. Adhes.*, 23:39–47, 2003.
- [62] K. Frühmann, I. Burgert, S. E. Stanzl-Tschegg, and E. K. Tschegg. Mode I fracture behaviour on the growth ring scale and cellular level of spruce (*Picea abies* [L.] Karst.) and beech (*Fagus sylvatica* L.) loaded in the transverse crack propagation system. *Holzforschung*, 57:653–660, 2003.
- [63] M.F.S.F. de Moura, R.D.S.G. Campilho, and J.P.M. Gonçalves. Crack equivalent concept applied to the fracture characterization of bonded joints under pure mode I loading. *Composites Science and Technology*, 68:2224–2230, 2008.
- [64] C.T. Scott, B.H. River, and J.A. Koutsky. Fracture testing wood adhesive with composite cantilever beam. *J. Test. Eval.*, 21:259–264, 1992.
- [65] F. Simon. *Endommagement et rupture des joints collés sollicités en traction ou cisaillement. Application au collage du bois*. PhD thesis, Université Bordeaux I, 2001.
- [66] S. Morel, E. Bouchaud, J. Schmittbuhl, and G. Valentin. R-curve behavior and roughness development of fracture surfaces. *International Journal of Fracture*, 114:307–325, 2002.
- [67] P. Qiao, J. Wang, and J.W. Davalos. Analysis of tapered ENF specimen and characterization of bonded interface fracture under mode II loading. *Int. J. Solids. Struct.*, 40: 1865–1884, 2003.
- [68] S. Morel, C. Lespine, J.-L. Coureau, J. Planas, and N. Dourado. Bilinear softening parameters and equivalent LEFM R-curve in quasibrittle failure. *Int. J. Solids. Struct.*, 47: 837–850, 2010.
- [69] N. Dourado, M.F.S.F. de Moura, and J. Morais. A numerical study on the SEN-TPB test applied to mode I wood fracture characterization. *International Journal of Solids and Structures*, 48:234–242, 2011.
- [70] S. Aicher, L. Boström, M. Gierl, D. Kretschmann, and G. Valentin. Determination of fracture energy of wood in mode II. Technical report, RILEM TC 133, 1997.

Bibliography

- [71] H. Yoshihara. Mode II R-curve of wood measured by 4-ENF test. *Eng. Fract. Mech.*, 71: 2065–2077, 2004.
- [72] H. Yoshihara. Mode II initiation fracture toughness analysis for wood obtained by 3-enf test. *Composites Science and Technology*, 65:2198–2207, 2005.
- [73] C. Schuecker and B. D. Davidson. Evaluation of the accuracy of the four-point bend end-notched flexure test for mode II delamination toughness determination. *Compos. Sci. Technol.*, 60:2137–2146, 2000.
- [74] A. Kutnar, F.A. Kamke, J.A. Nairn, and M. Sernek. Mode II fracture behavior of bonde viscoelastic thermal compressed wood. *Wood Fiber Sci.*, 40:362–373, 2008.
- [75] A. Arrese, N. Carbajal, G. Vargas, and F. Mujika. A new methode for determining mode II R-curve by the end-notched flexure test. *Eng. Fract. Mech.*, 77:51–70, 2010.
- [76] H. Yoshihara. Initiation and propagation fracture toughness of solid wood under the mixed mode i-ii conditin examined by mixed-mode bending test. *Eng. Fract. Mech.*, 104: 1–15, 2013.
- [77] M.E.S.F de Moura, J.M.Q. Oliveira, J.J.L. Morais, and J. Xavier. Mixed-mode I-II wood fracture characterization using the mixed-mode bending test. *Eng. Fract. Mech.*, 77: 144–152, 2010.
- [78] L.O. Jernkvist. Fracture of wood under mixed mode loading II. experimental investigation of picea abies. *Eng. Fract. Mech.*, 68:565–576, 2001.
- [79] E.K. Tschegg, A. Reiterer, T. Pleschberger, and S.E. Stanzl-Tschegg. Mixed mode fracture energy of sprucewood. *J. Mater. Sci.*, 36:3531–3537, 2001.
- [80] H.K. Singh, Chakraborty A., Frazier C.E., and A. Dillard. Mixed mode fracture testing of adhesively bonded wood specimens using a dual actuator load frame. *Holzforschung*, 64:353–361, 2010.
- [81] M.E.S.F de Moura, J.M.Q. Oliveira, J.J.L. Morais, and N. Dourado. Mixed-mode (i+ii) fracture characterization of wood bonded joints. *Construction and Building Materials*, 25:1956–1962, 2011.
- [82] G. Valentin and P. Caumes. Crack propagation in mixed mode in wood : a new specimen. *Wood Sci. Technol.*, 23:43–53, 1989.
- [83] L. Banks-Sills, M. Arcan, and H.D. Bui. Toward a pure shear specimen for K_{IIc} determination. *Int. J. Fracture*, 22:R9–R14, 1983.
- [84] H.L.J. Pang and W. Seetoh. A compact mixed mode (cmm) fracture specimen for adhesive bonded joints. *Eng. Fract. Mech.*, 57:57–65, 1997.

-
- [85] R Rikards. Interlaminar fracture behaviour of laminated composites. *Computer & Structures*, 76:11–18, 2000.
- [86] N. Choupani. Interfacial mixed-mode fracture characterization of adhesively bonded joints. *Int. J. Adhes. Adhes.*, 20:267–282, 2008.
- [87] P. Davies, L. Sohier, J.-Y. Cognard, A. Bourmaud, D. Choqueuse, E. Rinnert, and R. Créac’hcadec. Influence of adhesive bond line thickness on joint strength. *International Journal of Adhesion & Adhesives*, 29:724–736, 2009.
- [88] B. Golaz, V. Michaud, S. Lavanchy, and J.-A.E. Manson. Design and durability of titanium adhesive joints for marine applications. *International Journal of Adhesion & Adhesives*, 45:150–157, 2013.
- [89] K.B. Dahl and K.A Malo. Nonlinear shear properties of spruce softwood: Numerical analyses of experimental results. *Compos. Sci. Technol.*, 69:2144–2151, 2009.
- [90] K.B. Dahl and K.A Malo. Linear shear properties of spruce softwood. *Wood Sci. Technol.*, 43:499–525, 2009.
- [91] M. Méité, F Dubois, O. Pop, and J. Absi. Mixed mode fracture properties characterization for wood by digital images correlation and finite element methode coupling. *Eng. Fract. Mech.*, 105:86–100, 2013.
- [92] B. Franke and P. Quenneville. Analysis of the fracture behavior of radiata pine timber and laminated veneer lumber. *Eng. Fract. Mech.*, 116:1–12, 2014.
- [93] R. Moutou Pitti, F Dubois, and O. Pop. Sur une éprouvette assurant la stabilité de la propagation de fissure en mode mixte dans le matériaux bois. *C.R. Mecanique*, 336: 744–749, 2008.
- [94] B. Ginest, J.-Y. Cognard, and A. A. Pizzi. Analysis of the mechanical behavior of wood and welded wood under tensile-shear loads using a modified arcan device. *J. Adhes. Sci. Technol.*, 26:1717–1731, 2012.
- [95] V. Rizov. Mixed-mode I/II fracture study of polymer composites using single edge notched bend specimens. *Computational Material Science*, 77:1–6, 2013.
- [96] H. Petersson. Analysis of fracture propagation. In *COST 508 Workshop on Fracture mechanics in wooden materials*, pages 147–168, 1992.
- [97] B. Suthoff, A. Schaaf, H. Hentschel, and U. Franz. Verfahren zum reibschweissartigen verbinden von holz. Offenlegungsschrift DE 196 20 273 A1, 1997.
- [98] C. Ganne-Chedeville, M. Properzi, A. Pizzi, J.M Leban, and F. Pichelin. Parameters of wood welding: A study with infrared thermography. *Holzforschung*, 60:434–438, 2006.

Bibliography

- [99] J.M. Leban, A. Pizzi, S. Wieland, M. Zanetti, M. Properzi, and F. Pichelin. X-ray micro-densitometry analysis of vibration-welded wood. *J. Adhes. Sci. Technol.*, 18:673–685, 2004.
- [100] H.R. Mansouri, P. Omrani, and A. Pizzi. Improving the water resistance of linear vibration-welded wood joints. *J. Adhes. Sci. Technol.*, 23:63–70, 2009.
- [101] P. Omrani, H.R. Mansouri, G. Duchanois, and A. Pizzi. Fracture mechanics of linearly welded wood joints: effect of wood species and grain orientation. *J. Adhes. Sci. Technol.*, 23:2057–2072, 2009.
- [102] A. Pizzi, J.M. Leban, F. Kanazawa, M. Properzi, and F. Pichelin. Wood dowel bonding by high-speed rotation welding. *J. Adhes. Sci. Technol.*, 18:1263–1278, 2004.
- [103] F. Kanazawa, A. Pizzi, M. Properzi, L. Delmotte, and F. Pichelin. Parameters influencing wood-dowel welding by high-speed rotation. *J. Adhes. Sci. Technol.*, 19(19):1025–1038, 2005.
- [104] J.-F. Bocquet, A. Pizzi, and L. Resch. Full-scale industrial wood floor assembly and structures by welded-through dowels. *Holz als Roh- und Werkstoff*, 65:149–155, 2007.
- [105] J.-F. Bocquet, A. Pizzi, A. Despres, H. R. Mansouri, L. Resch, D. Michel, and F. Letort. Wood joints and laminated wood beams assembled by mechanically-welded wood dowels. *J. Adhes. Sci. Technol.*, 21:301–317, 2007.
- [106] P. Omrani, J.-F. Bocquet, A. Pizzi, J.-M. Leban, and H. Mansouri. Zig-zag rotational dowel welding for exterior wood joints. *J. Adhes. Sci. Technol.*, 21:923–933, 2007.
- [107] P. Omrani, H. R. Mansouri, and A. Pizzi. Weather exposure durability of dowel welded joint. *Holz als Roh- und Werkstoff*, 66:161–162, 2008.
- [108] M. Properzi, J.M. Leban, A. Pizzi, S. Wieland, F. Pichelin, and M. Lehmann. Influence of grain direction in vibrational wood welding. *Holzforschung*, 59:23–27, 2005.
- [109] B. Gfeller, A. Pizzi, M. Zanetti, M. Properzi, F. Pichelin, M. Lehmann, and L. Delmotte. Solid wood joints by in situ welding of structural wood constituents. *Holzforschung*, 58: 45–52, 2004.
- [110] M. Vaziri, O. Lindgren, and A. Pizzi. Influence of weldline density on moisture behaviour of scots pine joint produced by linear frictional welding. *J. Adhes. Sci. Technol.*, In Press, 2010.
- [111] M. Vaziri, O. Lindgren, and A. Pizzi. Influence of machine setting and wood parameters on crack formation in scots pine joints produced by linear welding. *Forest Prod. J.*, In Press, 2010.
- [112] DIN-EN205. DIN-EN 205, adhesives - wood adhesives for non-structural applications. Determination of the tensile-shear strength of lap joints. European Standard, 2003.

-
- [113] C. Ganne-Chedeville, A. Pizzi, A. Thomas, J.M. Leban, J.F. Bocquet, A. Despres, and H. Mansouri. Parameter interaction in two-block welding and the wood nail concept in wood dowel welding. *J. Adhes. Sci. Technol.*, 19:1157–1174, 2005.
- [114] P. Omrani, H.R. Mansouri, A. Pizzi, and E. Masson. Influence of grain direction and pre-heating on linear wood welding. *European Journal of Wood Products*, 68:113–114, 2010.
- [115] J. Delmotte, H. R. Mansouri, P. Omrani, and A. Pizzi. Influence of wood welding frequency on wood constituents chemical modifications. *Journal of Adhesion Science and Technology* 23, 23:1271–1279, 2009.
- [116] C. Ganne-Chedeville, G. Duchanois, A. Pizzi, F. Pichelin, M. Properzi, and J.M. Leban. Wood welded connection: energy release rate measurement. *J. Adhes. Sci. Technol.*, 22: 169–179, 2008.
- [117] T. Vallée, T. Tannert, S. Hehl, and C. Ganne-Chédeville. Capacity prediction of welded timber joints. *Wood Sci. Technol.*, 46:333–347, 2012.
- [118] B. Hahn, Y. Weinand, B. Stamm, and T. Vallée. Experimental investigation on welded double lap joints composed of timber. *Procedia Engineering*, 10:2526–2531, 2011.
- [119] M. Oudjene, M. Khelifa, C. Segovia, and A. Pizzi. Application of numerical modelling to dowel-welded wood joints. *J. Adhes. Sci. Technol.*, 24:359–370, 2010.
- [120] D5528-01. Standard test method for mode I interlaminar fracture toughness of unidirectional fiber-reinforced polymer matrix composites. American Society for Testing Material, 2007.
- [121] ASTM. Mixed mode I-mode II interlaminar fracture toughness of unidirectional fiber reinforced polymer matrix composites. American Society for Testing and Materials, 2006.
- [122] *Abaqus 6.12 User's Manual*. Dassault Simulia, 2012.
- [123] R. Krueger. Virtual crack closure technique: History, approach and applications. *Applied Mechanics Review*, 57:109–142, 2004.
- [124] J.F. Siau. *Wood: Influence of Moisture on Physical Properties*. Departement of Wood Science and Forest Product, 1995.
- [125] E. Charkaluk, M. Figerelle, and A. Iost. Fractals and fracture. *Eng. Fract. Mech.*, 61: 119–139, 1998.
- [126] M. I. Placencia Peña, A. L. Deutschle, B. Saake, A. Pizzi, and F. Pichelin. Study of the solubility and composition of welded wood material at progressive welding times. *Holzforschung*, Submitted.

Bibliography

- [127] J.L. Coureau, S. Morel, P.J. Gustafsson, and C. Lespine. Influence of the fracture softening behavior of wood on load-COD curve and R-curve. *Mater. Struct.*, 40:97–106, 2006.
- [128] M. Rheme, J. Botsis, J. Cugnoni, and P. Navi. Influence of the moisture content on the fracture characteristics of welded wood joint - part 1: Mode I fracture. *Holzforschung*, 67:747–754, 2013.
- [129] F. Kollmann. *Technologie des Holzes und der Holzwerkstoffe*. Springer Verlag, Berlin, 1982.
- [130] M. A. Dietenberger, D. W. Green, D. E. Kretschmann, and R. Hernandez. *Wood handbook - Wood as an engineering material*. 1999.
- [131] M. Rheme, J. Botsis, J. Cugnoni, and P. Navi. Influence of the moisture content on the fracture characteristics of welded wood joint - part 2 : Mode II fracture. *Holzforschung*, 67:755–761, 2013.
- [132] T. Ozyhar, S. Hering, and P. Niemz. Moisture dependent elastic and strength anisotropy of european beech wood in tension. *J. Mater. Sci.*, 47:6141–6150, 2012.
- [133] C. Ganne-Chedeville, M. Properzi, J.-M. Leban, A. Pizzi, and F. Pichelin. Wood welding: Chemical and physical changes according to the welding time. *J. Adhes. Sci. Technol.*, 22:761–773, 2008.
- [134] G. H. Valentin, L. Boström, P. J. Gustafsson, A. Ranta-Maunus, and S. Gowda. Application of fracture mechanics to timber structure rilem state-of-the-art report. Technical Report 1262, Technical Research Center of Finland, 1991.
- [135] J. R. Reeder. 3d mixed-mode delamination fracture criteria - an experimentalist's perspective. In *American Society for Composites 21st Annual Technical Conference*, 2006.
- [136] M. Rheme, J. Botsis, J. Cugnoni, and P. Navi. Mixed mode fracture behavior of welded wood joint investigated with the Arcan test. *Wood Sci. Technol.*, Submitted, 2014.
- [137] S. Mindess. The fracture of wood in tension parallel to the grain. *Can. J. Civ. Eng.*, 4: 412–416, 1977.
- [138] M. Charalambides, A.J. Kinloch, Y. Wang, and Williams J.G. On the analysis of mixed-mode failure. *Int. J. Fracture*, 54:269–291, 1992.
- [139] M. Rheme, J. Botsis, J. Cugnoni, and N. Parviz. Mixed mode crack propagation in welded wood joint. *Eng. Fract. Mech.*, Submitted, 2014.
- [140] R. Moutou Pitti. *Découplage des modes mixtes de rupture dans les matériaux viscoélastiques orthotropes - modélisation et expérimentation*. PhD thesis, Université de Limonge, 2008.
- [141] J. Froidevaux. *Wood and paint layers aging and risk analysis of ancient panel painting*. PhD thesis, Université de Montpellier 2, 2012.

- [142] M. Sedighi-Gilani and P. Navi. Micromechanical approach to wood fracture by three-dimensional mixed lattice-continuum model at fibre level. *Wood Sci. Technol.*, 47: 619–634, 2007.
- [143] J. A. Nairn. Material point method simulations of transverse fracture in wood with realistic morphologies. *Holzforschung*, 61:375–381, 2007.
- [144] J. Botsis, L. Humber, F. Colpo, and P. Giaccari. Embedded fiber bragg grating sensor for internal strain measurements in polymeric materials. *Optics and Lasers in Engineering*, 43:497–510, 2005.
- [145] S. Stutz, J. Cugnoni, and J. Botsis. Studies of mode I delamination in monotonic and fatigue loading using FBG wavelength multiplexing and numerical analysis. *Compos. Sci. Technol.*, 71:443–449, 2011.
- [146] R. Falciai, C. Trono, G. Lanterna, and C. Castelli. Continuous monitoring of wooden works of art using fiber bragg grating sensors. *Journal of Cultural Heritage*, 4:285–290, 2003.

Martin RHÊME
Route du Coteau 17
1752 Villars sur Glâne
076/205 11 14

34 years old (28.12.1979)
Married
Swiss
martin.rheme@gmail.com



Skills and Interests

- Fracture mechanics
- Material characterization
- FEM / FEA
- R&D activities in industrial environment
- Solve multi-materials issues

Education

- **PhD, Material Science and Engineering** 2010 – 2014
 - EPFL – Material Science Doctoral school
- **Master of Science, Material Science and Engineering** 2005 – March 2007
 - EPFL – Material Science Section
- **Bachelor, Material Science and Engineering** 2001 – 2005
 - EPFL – Material Science Section
- **Semester Abroad** Jan. 2001– June 2001
 - Santa Barbara City College, USA (CA)
- **Maturité fédérale, Type C** 1996– 2000
 - Collège St –Michel, Fribourg

Working experience

- **Bern University of Applied Science** Currently
 - R&D Assistant in Institute of Material and wood technology
 - Involvement and lead of research project and services for the industry
 - Project acquisition and proposal writing (CTI, SNF, EU)
- **EPFL – Computational Materials Laboratory** April – July 2007
 - Assistant
 - Bi-metal laser soldering – Determination of a range of parameters
- **EPFL – Laboratory of Mechanical Metallurgy** Summer 2006
 - Assistant
 - Development of a platform for thermal properties measurements using the software LabVIEW
- **Contrinex SA / Proximity Switches** Summer 2005
 - Trainee
 - Development of PU and silicon foam for the encapsulation of electronic components

Teaching Experience

- **Passerelle “Baustoffkunde” Modul**
 - Introduction course to material science 2011 – present

Selected Projects

- **Ultra-light particleboard**
 - A continuous process to produce ultra-light particleboard with a foam core layer
- **Sinergia Welding for Wood**
 - Fracture characteristics of welded wood joints
- **Clear Coat**
 - Development of a transparent powder coating for MDF finishing
- **Various services in the field of wood based panel production and characterization**

Languages and Computer skills

- | | |
|----------------|--|
| ➤ French | First language |
| ➤ English | Very good knowledge (Council of Europe Level C1) |
| ➤ German | Good knowledge (Council of Europe Level B1) |
| ➤ Spanish | Basic knowledge (Council of Europe Level A1) |
| ➤ Office suite | Microsoft Office, Open Office |
| ➤ Mathematics | Mathematica, Matlab |
| ➤ Programming | Lab VIEW, Visual C, LaTeX |
| ➤ FEA/CAD | Abaqus, Ansys, CATIA |

Peer-reviewed Publications

- M. Rhême, J. Botsis, J. Cugnoni, and P. Navi. Mixed mode crack propagation in welded wood joint. *Eng. Fract. Mech.* Submitted.
- M. Rhême, J. Botsis, J. Cugnoni, and P. Navi. Mixed mode fracture behavior of welded wood joint investigated with the Arcan test. *Wood Sci. Technol.*, Submitted.
- M. Rhême, J. Botsis, J. Cugnoni, and P. Navi. Influence of the moisture content on the fracture characteristics of welded wood joint – part 1: Mode I fracture. *Holzforschung*, 67:747–754, 2013.
- M. Rhême, J. Botsis, J. Cugnoni, and P. Navi. Influence of the moisture content on the fracture characteristics of welded wood joint – part 2 : Mode II fracture. *Holzforschung*, 67:755–761, 2013.
- M. Rhême, F. Gonzales, and M. Rappaz. Growth directions in directionally solidified al–zn and zn–al alloys near eutectic composition. *Scr. Mater.*, 59(4):440 – 443, 2008.
- J.–M. Molina, M. Rhême, J. Carron , L. Weber. Thermal conductivity of aluminum matrix composites reinforced with mixtures of diamond and SiC particles. *Scripta Mat.*, 58 , 393–396, 2008.

Other Activities

- Mountaineering and backcountry skiing
- Member of the Swiss Alpine Club, section Moléson
- Member of the Athletic Club of Belfaux, J+S instructor of Track and Field